



**HAL**  
open science

# Graphene oxide sheets confined within anisotropic fluid matrices

Rafael Leite Rubim

► **To cite this version:**

Rafael Leite Rubim. Graphene oxide sheets confined within anisotropic fluid matrices. Other [cond-mat.other]. Université de Bordeaux, 2018. English. NNT : 2018BORD0209 . tel-01997785

**HAL Id: tel-01997785**

**<https://theses.hal.science/tel-01997785>**

Submitted on 29 Jan 2019

**HAL** is a multi-disciplinary open access archive for the deposit and dissemination of scientific research documents, whether they are published or not. The documents may come from teaching and research institutions in France or abroad, or from public or private research centers.

L'archive ouverte pluridisciplinaire **HAL**, est destinée au dépôt et à la diffusion de documents scientifiques de niveau recherche, publiés ou non, émanant des établissements d'enseignement et de recherche français ou étrangers, des laboratoires publics ou privés.



THESIS PRESENTED  
TO OBTAIN THE GRADE OF  
**DOCTOR FROM THE**  
**UNIVERSITY OF BORDEAUX**

DOCTORAL SCHOOL OF PHYSICS AND ENGINEERING  
FIELD: LASERS, MATTER AND NANOSCIENCE

Rafael Leite Rubim

**Graphene oxide sheets confined within  
anisotropic fluid matrices**

Advisors:

Ms. Laurence Navailles    Centre National de la Recherche Scientifique  
Mr. Frédéric Nallet        Université de Bordeaux

Thesis publicly defended on 12 November 2018.

Members of the committee:

Ms. Cécile Zakri	Université de Bordeaux	President
Ms. Brigitte Pansu	Université Paris-Sud	Rapporteur
Mr. Eric Anglaret	Université de Montpellier	Rapporteur
Ms. Elisabeth Andreoli de Oliveira	Universidade de Brasília	Examiner
Mr. Cristiano L. Pinto de Oliveira	Universidade de São Paulo	Examiner



*"Happy the one who transfers what he knows  
and learns what he teaches."*

"Feliz aquele que transfere o que sabe  
e aprende o que ensina."

Cora Coralina

Okê Arô...

# Resumé

## Confinement de feuillets de graphène oxydé dans une matrice fluide anisotrope

Dès sa découverte, le graphène oxydé (GO), le plus accessible des précurseurs du graphène, a été largement utilisé pour des applications en science et technologie. La motivation de ce travail est d'étudier, d'un point de vue fondamental, le couplage entre des bicouches amphiphiles auto-associées (lesquelles peuvent être vues comme une matrice anisotrope formée d'objets bidimensionnels) et un objet lui-même bidimensionnel, en l'occurrence le feuillet d'oxyde de graphène, quand ils sont dispersés dans un solvant commun.

La compétition entre les élasticités intrinsèques des bicouches et des feuillets de GO, ainsi que les interactions directes bicouche-bicouche, bicouche-GO et GO-GO, permet d'envisager un riche polymorphisme en fonction de la composition du système. Après avoir développé une procédure destinée à contrôler, dans une gamme étendue de teneur en GO, le système binaire GO-eau, le domaine confiné des dispersions aqueuses de GO a été exploré et, par la suite, le diagramme de phases ternaire a été construit.

Les systèmes obtenus ont été caractérisés par des techniques comme la microscopie optique et la diffusion du rayonnement (diffusion dynamique de la lumière et diffusion des rayons-X aux petits angles). Les propriétés élastiques et thermodynamiques ont été décrites par l'application de modèles initialement conçus pour les phases lamellaires à deux constituants et adaptés dans le cadre de cette étude.

**Mots clés :** graphène oxydé, tensioactif, cristaux liquides, SAXS, empilements de bicouches



# Resumo

## Confinamento de folhas de grafeno oxidado em uma matriz fluida anisotrópica

Desde sua descoberta, o grafeno oxidado (GO), o mais acessível dos precursores do grafeno, tem sido amplamente utilizado para aplicações na ciência e tecnologia. A motivação deste trabalho é de estudar, de um ponto de vista fundamental, o acoplamento entre bicamadas anfífilas auto-organizadas (que podem ser vistas como uma matriz anisotrópica formada por objetos bidimensionais) e um objeto ele mesmo bidimensional, neste caso a folha de óxido de grafeno, quando estão dispersados em um solvente comum.

A competição entre as elasticidades intrínsecas das bicamas e das folhas de GO, assim como as interações diretas bicamada-bicamada, bicamada-GO e GO-GO, permitem esperar um rico polimorfismo em função da composição do sistema. Seguindo o desenvolvimento de um procedimento destinado ao controle, em um intervalo estendido da quantidade de GO, o sistema binário GO-água, o domínio confinado de dispersões aquosas de GO foi explorado e, em seguida, o diagrama de fases ternário contruído.

Os sistemas obtidos foram caracterizados por técnicas como microscopia ótica, espalhamento dinâmico de luz e espalhamento de raios-x à baixos ângulos. As propriedades elásticas e termodinâmicas foram descritas pela aplicação de modelos inicialmente concebidos para fases lamelares à dois constituintes e adaptados ao escopo deste estudo.

**Palavras-chave:** grafeno oxidado, surfactante, cristais líquidos, SAXS, empilhamento de bicamadas



# Abstract

## Graphene oxide sheets confined within anisotropic fluid matrices

Since the discovery of graphene oxide (GO), the most accessible of the precursors of graphene, this material has been widely studied for applications in science and technology. The motivation of this work is to study with a fundamental perspective the coupling between amphiphilic bilayers, which can be seen as an anisotropic matrix formed of two-dimensional objects, and another two-dimensional object, namely the graphene oxide sheet when they are dispersed in a common solvent.

The competition between the intrinsic elasticities of the bilayers and GO sheets, as well as between direct bilayer-bilayer, bilayer-GO and GO-GO interactions allows us to envisage a rich polymorphism, depending on the composition of the system. Following the development of a dedicated procedure for controlling in an extended range of GO content the binary GO-water system, the confined domain of aqueous GO dispersions was first investigated, and the ternary phase diagram then constructed.

The obtained systems have been characterised, using techniques such as optical microscopy, light and x-ray scattering. Elastic and thermodynamic properties have been described by applying, and adapting to the scope of this study, models for two-component lamellar stacks.

**Keywords:** graphene oxide, surfactant, liquid crystal, SAXS, stacked layers



# Acknowledgments

The accomplishment of this work would not have been possible without all the help I have received during these last years. I would like to thank everyone who somehow contributed for this thesis to be concluded in the best conditions, either directly or indirectly. It would be very difficult to list the names of each of them, but there are some special ones that I could not forget.

First I would like to thank those who looked after me, guiding my steps. Thanks to my wife, who was always by my side and gave me the strength needed to keep going, I was able to finish one more step. I also thank my mother, who provided me all the necessary to be who I am.

Not less importantly, I would like to thank Laurence and Frédéric for giving me the opportunity to take part in this work. Thank you for inspiring me and for everything you gave me during these years, I have learnt a lot from you. In addition, the idea of this project would not have been possible without initial discussions with George Nounesis, so I am grateful to him for that.

I also thank Beth for being part of my learning and encouraging me to face this challenge. Without your help I would not be where I am today and it was a pleasure for me that you could be influential in this new step in my career. My special thanks also to Cristiano, who was also there since the beginning of my scientific career. Thank you for all the discussions and for the contributions in this work.

The contributions of Brigitte Pansu and Eric Anglaret were also very helpful to improve this text. Thank you to both of you for reading this thesis and for the discussions during the defence.

I also would like to thank Cécile Zakri, not only for evaluating my work during the defence, but also for everything you have done as director of the laboratory, providing a good scientific environment and always listening to the needs of the students.

I could not thank enough my duo, Kévin. You were always there to support and help me when needed. I would also like to thank all your family, which became an extension of our family here in France, and our new friends.

I also thank Margarida, Thomas and Clément. Without your help, the accomplishment of this work would not have been possible. Special thanks to Annie, Ahmed and all the services of the laboratory that helped me. Without you, the development of this work would have been much more difficult.

Thank you to all my friends from the CRPP: Vincent, Éric, Antoine, Valentine, Bosi, Mayada, Hélène, Artem, Maxime, Michaël, Mayte, Hervé, Julien, Maeva, Pierre-Etienne, Aurélie, Élodie, Marie, Sandra, Rémi, Alliny, Flávia, Deysi, Gabi, Thamires, Marli, Simon, Cécile, Amarande, Alexis, Mélodie, Margot and possibly someone I forgot to mention here. Even if I was far from home, you made my days much easier.

And finally, I would like to thank all my friends and family, specially those who are geographically distant, but stayed very close during this phase. Thank you for the support you gave me.

# Contents

<b>1</b>	<b>Introduction</b>	<b>15</b>
1.1	Context of the study . . . . .	15
1.2	Motivation and objectives . . . . .	15
1.3	Scientific environment . . . . .	16
<b>2</b>	<b>State of art</b>	<b>17</b>
2.1	Graphene oxide . . . . .	17
2.2	Liquid crystals . . . . .	20
2.3	Surfactants . . . . .	24
2.4	Characterisation techniques . . . . .	26
2.4.1	Polarised Optical Microscopy . . . . .	27
2.4.2	Transmission Electron Microscopy . . . . .	27
2.4.3	Dynamic Light Scattering . . . . .	27
2.4.4	Small Angle X-Ray Scattering . . . . .	29
<b>3</b>	<b>Highly concentrated dispersions of graphene oxide</b>	<b>33</b>
3.1	Characterisation of the GO sheets . . . . .	33
3.2	Preparation of highly concentrated GO dispersions . . . . .	39
3.3	Structural characterisation of highly confined GO sheets in water . . . . .	42
3.4	Effect of salt on interactions between GO sheets . . . . .	48
<b>4</b>	<b>SAXS models for graphene oxide dispersions</b>	<b>53</b>
4.1	Absolute scale normalisation . . . . .	53
4.2	Principles of SAXS theory for disk-like objects . . . . .	55
4.3	Fittings of SAXS curves . . . . .	57
<b>5</b>	<b>Complexes of Graphene Oxide and Surfactant</b>	<b>65</b>
5.1	Self-assembly of surfactant in water . . . . .	65
5.2	Preparation of GO-surfactant complexes . . . . .	68
5.3	Binary (dehydrated) GO-surfactant complexes . . . . .	73
5.4	Ternary (hydrated) GO-surfactant complexes . . . . .	78

<b>6</b>	<b>Conclusions</b>	<b>91</b>
6.1	Results . . . . .	91
6.2	Perspectives . . . . .	93
	<b>Bibliography</b>	<b>95</b>
	<b>List of symbols and acronyms</b>	<b>109</b>
	<b>List of figures</b>	<b>113</b>
<b>A</b>	<b>Published Article</b>	<b>115</b>
<b>B</b>	<b>Résumé détaillé</b>	<b>127</b>
<b>C</b>	<b>Resumo detalhado</b>	<b>131</b>

# Chapter 1

## Introduction

### 1.1 Context of the study

After the study developed by Emerson Rodrigo da Silva (da Silva, 2011), followed by Kévin Bougis (Bougis, 2016), the formulation of complexes composed of lipid bilayers is in focus in our group. Using techniques like x-ray scattering, optical and electronic microscopy, the properties of systems formed by a host lamellar structure and DNA fragments were investigated.

The DNA fragments are short enough to be meaningfully seen as cylinders, or one-dimensional particles, and the insertion/organization of these macro molecules in between the bilayers, a two-dimensional matrix, gives rise to different self-organized structures. This work was then the inspiration for trying to insert in between the membranes a two-dimensional object itself, namely graphene oxide sheets.

### 1.2 Motivation and objectives

The motivation of this work is to study the coupling between the amphiphilic bilayers, which can be seen as an anisotropic matrix formed of two-dimensional objects, and another two-dimensional object, namely the graphene oxide sheet.

Since the discovery of graphene oxide, the most accessible of the precursors of graphene, this material has been widely studied for applications in science and technology. The objective of this study is, from a fundamental point of view, the investigation of the effects of confinement on self-assembled complex systems of soft matter and, in particular, the insertion of GO sheets into a fluid anisotropic matrix. The competition between the elasticity of the bilayer and that of GO allows to envisage a rich polymorphism depending on the composition of the system.

Initially, the fundamental aspects of the investigated system are introduced and the experimental techniques, such as optical and electron microscopy, light and x-ray scattering, employed to get the data for their characterization are described (chapter 2).

Afterwards, the concentrated regime of the binary system (graphene oxide-water) will be described (chapter 3), followed by the discussion of the analysed structure using theoretical models already proposed and others that will be developed in the scope of this work (chapter 4).

In a second step, properties of the host matrix composed of surfactant will be studied, as well as the binary complex (graphene oxide-surfactant). These results will contribute to the interpretation of the results obtained for the ternary system (graphene oxide-water-amphiphiles). This characterisation will provide relevant information about a new material that could be used in many future applications (chapter 5).

The phase diagram will be constructed, given as the final, conclusive part of chapter 5.

### **1.3 Scientific environment**

The work has been developed at the Structure and Dynamics of Soft Matter (M2SD) team of the *Centre de recherche Paul-Pascal*, a laboratory located in Pessac and attached to the University of Bordeaux and the National Center for Scientific Research (CNRS - France).

The financial support for the thesis was provided by the Science Without Borders program (Process: 250085/2013-5), an initiative of the Brazilian government through the National Council for Scientific and Technological Development (CNPq - Brazil).

# Chapter 2

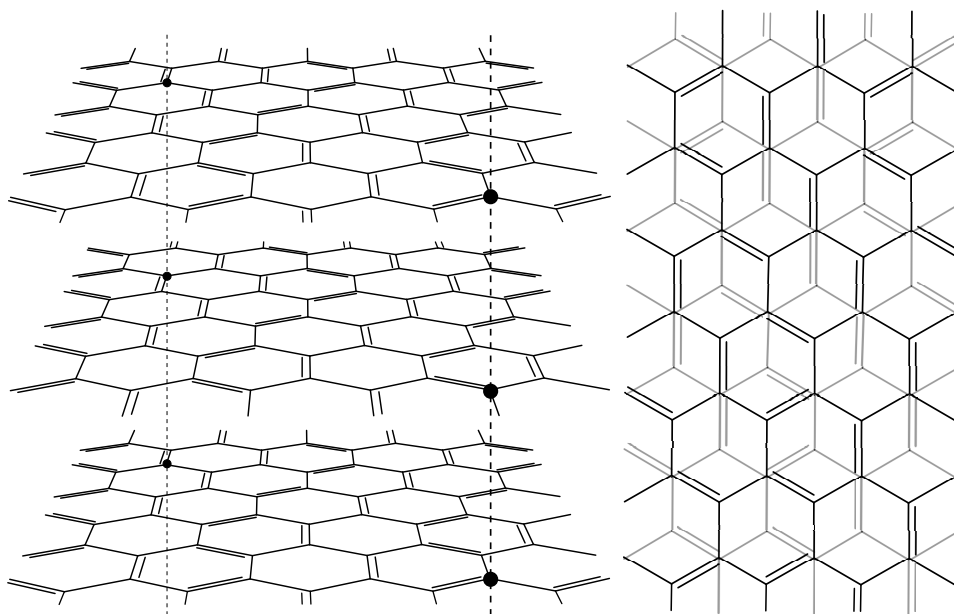
## State of art

### 2.1 Graphene oxide

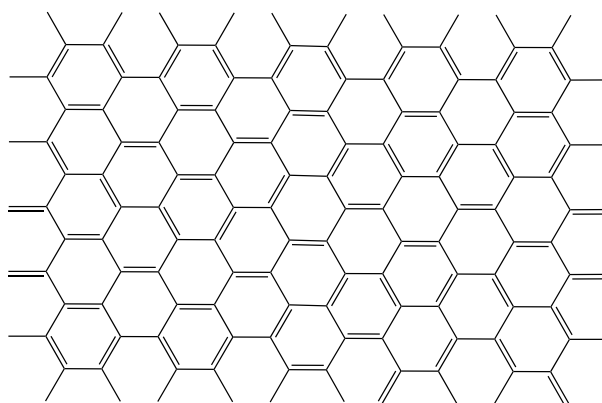
Graphite or, more precisely, hexagonal graphite (Nič et al., 2009), is a material that was discovered in the earliest times and has been used since, especially because of its use for writing. Nowadays, it is also widely used for engineering and industrial applications because of its excellent in-plane properties. This allotropic form of carbon is the most thermodynamically stable and has a unique structure, which gives it very interesting electrical, thermal and mechanical characteristics (Kelly, 1981). The structure of graphite was one of the first ones to be studied by X-ray diffraction (Hull, 1917) and, as shown in Figure 2.1a, it consists on hexagonal net planes of carbon atoms stacked periodically along the axis perpendicular to their plane. In the plane, the distance between the nearest neighbour carbon atoms is  $1.4 \times 10^{-10}$  m and adjacent layers are shifted, with a spacing of  $3.4 \times 10^{-10}$  m between them (Bernal, 1924).

The covalent bonds between the carbon atoms in the plane are much stronger than the metallic bonds between the planes, which facilitates the dissociation of graphite into individual layers. As shown in Figure 2.1b, these layers have the structure of a triangular lattice of carbon atoms with a single atom thickness, and they are called graphene (Nič et al., 2009; Boehm et al., 1994). The idea of graphene has been introduced by scientists many years ago (Wallace, 1947) and some experiments even evidenced its existence a few years later (Boehm et al., 1962), but from the theoretical point of view, it was considered impossible to obtain thermodynamically stable two-dimensional crystals (Landau, 1937; Mermin, 1968). It was only in 2004 that this material was isolated and characterised for the first time (Novoselov et al., 2004), this work being awarded with the 2010 Nobel prize in Physics (Prezhdo, 2011).

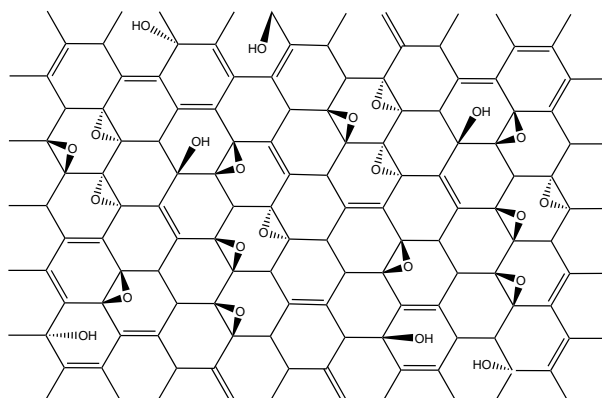
Graphene is a material that presents high electronic mobility and high mechanical strength, being at the same time very light, flexible and near transparent (Geim, 2009). Due to its extraordinary properties, graphene has gained space in the research and industry, finding many applications in the fields of materials, composites, sensors, energy,



(a) Graphite in perspective and top views.



(b) Graphene and reduced Graphene Oxide.



(c) Graphene Oxide.

Figure 2.1 – Structural representation of carbon materials.

electronics and many others (Qiu et al., 2012; Marcaccio and Paolucci, 2014; Mohan et al., 2018).

There are a lot of available procedures to produce graphene (Spyrou and Rudolf, 2014), and the one mentioned above consists on obtaining graphene layers from several steps of exfoliation, peeling the layers from graphite using an adhesive (Scotch®) tape (Novoselov et al., 2004). The graphene produced using this method has the lowest number of defects, presenting the highest quality concerning electron mobility and structure (Kusmartsev et al., 2014). However, another very common way of preparing this material consists on reducing exfoliated layers of chemically oxidised graphite, which provides lower quality graphene but in a much larger scale (Stankovich et al., 2007; Wang et al., 2008; Gao et al., 2009). The graphite oxide, also known as graphitic oxide, was first prepared by Brodie (1859), but one of the most frequent methods used nowadays is based on the procedure proposed by Hummers and Offeman (1958), which has been improved with the years to increase the ratio between oxygen and carbon atoms in the material (Marcano et al., 2010).

Studies were developed using graphite oxide and dispersions of the layers in acid medium (Behabtu et al., 2010), however, the advantage of the graphite oxide, compared to the graphite, is its affinity with water. The hydration of graphite oxide was experimentally investigated, showing that the distance between the layers can be increased when solvent is added (Scholz and Boehm, 1969). In Figure 2.2, data extracted from the literature show the evolution of the interlayer distance of the graphite oxide when the material is hydrated.

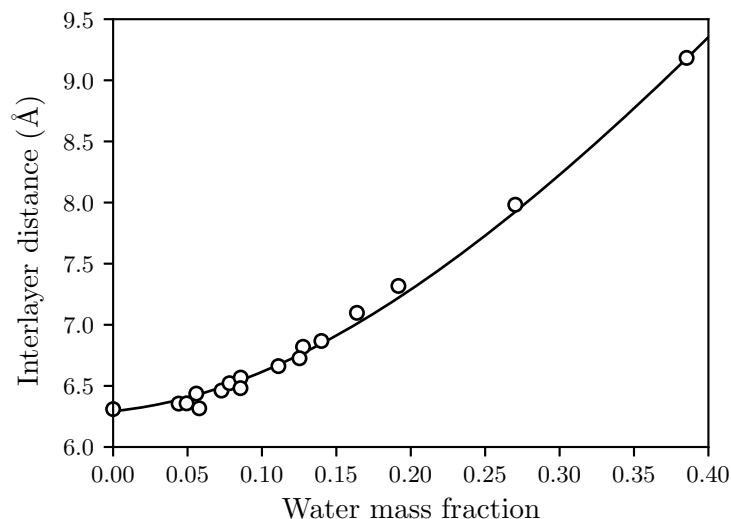


Figure 2.2 – Interlayer distance as a function of the water mass fraction for graphite oxide. Data extracted from Scholz and Boehm (1969).

These observations show that after obtaining the graphite oxide, it is possible to separate the layers and ultrasonication can be used to exfoliate the material, so then thin

layers will be suspended in the solvent. The obtained thin layers of graphite oxide are graphene containing oxygen atoms in the form of epoxy, hydroxyl, carbonyl and carboxylic groups, and this material is called graphene oxide (GO) (Stankovich et al., 2006b; Marcano et al., 2010). Its precise structure depends on the level of oxidation, but a representation is shown in Figure 2.1c.

Besides the structure, the properties of GO are very different from the ones of graphene, because of the presence of the oxygen groups, which makes this material a bad electrical and thermal conductor. However, these groups can be partially removed *via* chemical, photochemical, electrochemical or thermal reduction, and a new material called partially reduced graphene oxide (rGO) is obtained (Stankovich et al., 2006a; Schniepp et al., 2006; Cote et al., 2009; Zhou et al., 2009; An et al., 2010; Pei and Cheng, 2012). After this procedure, even if the material keeps a few defects, it recovers part of the properties of graphene (Gao et al., 2009).

Graphene oxide is attracting a lot of interest, especially due to its unique properties, which have already been mentioned, with the advantage of interacting with water, as well as other solvents. Many composites and new materials are prepared by the deposition of GO and solution processing, besides its applications in the biotechnological and biomedical field (Zhou et al., 2009; An et al., 2010; Bisoyi and Kumar, 2011; Xu and Gao, 2011b; Frost et al., 2012; Kim et al., 2012; Singh et al., 2018).

The structure of GO sheets, as well as their structural organisation in water have been experimentally investigated and these studies revealed, in an extended range of solvent content, a liquid-crystalline structure, liquid crystals being materials with special characteristics that will be treated in the next section. In addition, it has been recently evidenced that the GO sheets are very flexible, with a bending modulus in the order of  $k_B T$  (Poulin et al., 2016). Incidentally, most of these works assume for the GO sheets a density around  $1.8 \text{ g/cm}^3$  and a thickness smaller than 1 nm (Behabtu et al., 2010; Kim et al., 2011; Xu and Gao, 2011a; Aboutalebi et al., 2011; Zamora-Ledezma et al., 2012; Dan et al., 2011; Xu and Gao, 2011b).

## 2.2 Liquid crystals

We all have in mind that matter can be found in nature in one of the three different fundamental states. A brief definition of each one of the states is presented below.

1. Solid, also known as crystal, is a dense state where the components have strong interactions and are regularly distributed in a three-dimensional periodic lattice, presenting a defined form;
2. Liquid is also a dense state where the components have still quite strong interactions and no ordered structure, being able to flow;

3. Gas is a dilute state where the components have negligible interactions and no structure, occupying all the available space.

Moreover, some materials can be transformed from one of the three states to the others without changing their chemical composition. Water is the most common example of these materials, whose phase transitions are obtained changing the temperature and/or pressure. Despite the fact that many other materials present the same phase transitions, some other compounds have a much more complex phase diagram.

Certain organic materials present several transitions involving new phases with intermediate properties between the liquid and solid states. These intermediate states are called mesomorphic phases and a material that presents these properties is called liquid crystal (LC) (Liebert, 1978; Kelker and Hatz, 1980; de Gennes and Prost, 1995; Dierking and Al-Zangana, 2017). This is the term used to define these materials because of the liquid-like order, also called isotropic organisation, they have in at least one direction of space and an ordered structure in the other directions. There are three possible forms of liquid crystals:

1. Nematic, a mesophase in which the components have a defined preferred orientation but their centres of gravity do not present a positional order;
2. Smectic, a mesophase in which the components have a defined preferred orientation and are organised, forming stacked layers. In the perpendicular direction to the layers, there is a positional order of the centres of gravity, while there is no positional order in the parallel direction;
3. Columnar is a mesophase in which the components have a defined preferred orientation and are organised forming cylinders. In the perpendicular direction to the axis of symmetry of the cylinders there is a positional order of the centres of gravity, while there is no positional order in the parallel direction.

Elongated objects tend to form nematic and smectic phases, while columnar and also nematic phases are often obtained with disk-like particles. The LCs are grouped in two different classes, called thermotropic liquid crystals or lyotropic liquid crystals, depending on whether the phase transitions are obtained by varying a variable of state, such as the temperature or pressure, or varying the concentration, respectively.

It has been shown in the literature that aqueous dispersions of GO present the same behaviour observed for lyotropic liquid crystals. When the dispersion is diluted, no preferred orientation of the layers is observed, which means that they present an isotropic organisation. However, an increasing in the concentration makes the GO sheets start to orientate themselves in a given direction, and birefringence can be observed under polarised optical microscopy (see subsection 2.4.1) (Kim et al., 2011; Xu and Gao, 2011a; Aboutaleb et al., 2011; Dan et al., 2011; Xu and Gao, 2011b; Zamora-Ledezma et al.,

2012; Zakri et al., 2013; Jalili et al., 2013; Xu and Gao, 2014; Tong et al., 2014; Tkacz et al., 2014).

This organisation is equivalent to the one observed for nematic mesophases in LCs and the concentration at which the transition occurs is dependent on the aspect ratio  $\varsigma$  of the GO sheets that is calculated using Equation 2.1, where  $\delta$  is the layer thickness and  $l$  its maximum lateral extension.

$$\varsigma = \frac{l}{\delta} \quad (2.1)$$

From Onsager's theory (1949), it is possible to predict the isotropic-nematic phase transition for suspensions of hard cylinder-like particles with a given aspect ratio. This model also gives a good qualitative estimate of the phase transition for flat particles. In the case of GO dispersions, the mass fraction of GO  $f_m$  at which we observe the phase transition can be obtained using Equation 2.2.

$$f_m \approx \frac{4.8}{\varsigma} \quad (2.2)$$

If the distribution of sizes of the GO sheets is very large, which means that the GO sheets present a high polydispersity in size, the concentration at which the phase transition occurs is not well defined. Instead, there is an interval of mass fractions where the phase transition takes place. For a given concentration, the biggest sheets start to orientate and birefringence is observed. This phenomenon corresponds to the appearance of nematic domains, coexisting with isotropic organisation.

When the concentration is further increased, the smaller sheets will also orientate themselves, increasing the presence of nematic domains until it reaches a certain concentration in which the isotropic organisation is no longer observed and the whole sample presents a nematic structure. In Figure 2.3, experimental results obtained from the literature are presented. For a few given average aspect ratios, the concentrations of GO in water when the nematic structure is first observed and when the whole sample presents this organisation are showed.

These experiments showed that the theoretical prediction given by Equation 2.2 is in good accordance with the values of concentrations that define the interval of coexistence of isotropic and nematic orientations for polydisperse samples. It has also been observed that for even higher concentrations, the GO sheets start to stack in layers with a periodic distance of repetition, an organisation that is equivalent to the one observed for smectic mesophases.

The stacked structures were further analysed and it is possible to investigate the evolution of the distance of repetition of the lamellar structure as a function of the mass fraction for different aspect ratio of GO sheets in the aqueous dispersion (Xu and Gao, 2011a,b; Zamora-Ledezma et al., 2012). As illustrated in Figure 2.6, lamellar periodicity  $d$  is the distance of repetition of the unit cell and, from the data available in the literature,

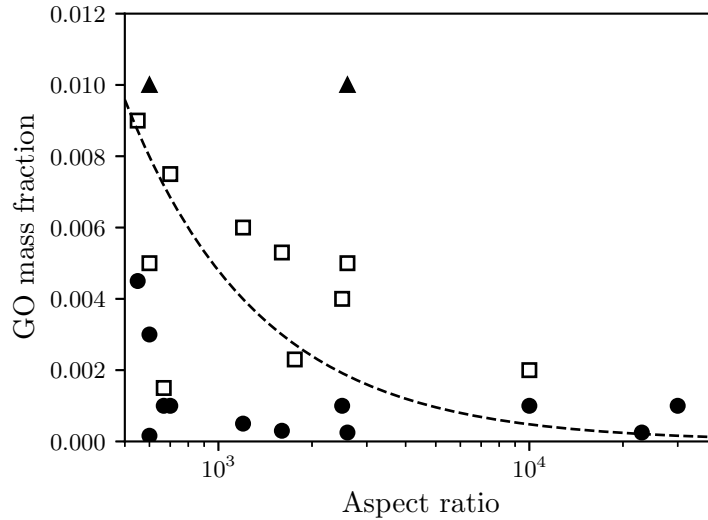


Figure 2.3 – Mass fraction of GO in water when the phase transitions are observed as a function of the aspect ratio. Lower (●) and upper (□) limits of the coexistence of isotropic-nematic mesophases and lamellar (▲) mesophases. Dashed line corresponds to the phase transition given by Equation 2.2. Data extracted from Kim et al. (2011), Xu and Gao (2011a), Aboutalebi et al. (2011), Dan et al. (2011), Xu and Gao (2011b), Zamora-Ledezma et al. (2012), Zakri et al. (2013), Jalili et al. (2013), Xu and Gao (2014), Tong et al. (2014) and Tkacz et al. (2014).

it is possible to obtain the curve of this variable as a function of the mass fraction of GO for different aspect ratios, as shown in Figure 2.4.

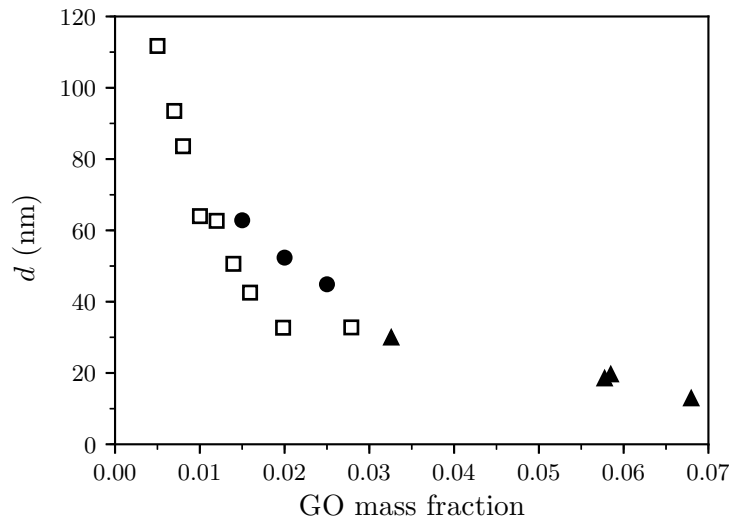


Figure 2.4 – Lamellar periodicity as a function of GO mass fraction in water for layers with an aspect ratios of: 2600 (●), 1000 (□) and 667 (▲). Data extracted from Xu and Gao (2011a), Xu and Gao (2011b) and Zamora-Ledezma et al. (2012).

One can observe from the data that increasing the mass fraction of GO makes the distance of repetition of the lamellar structure to decrease, which is in accordance with what is observed for smectic lyotropic liquid crystals. In addition, the continuous curve indicates that this behaviour is not dependent on the aspect ratio of the GO layers.

From these observations, it is now clear that graphene oxide layers can behave as a lyotropic liquid crystal when in solution. A classic example of this class of liquid crystal is the surfactants, which will be discussed in next section.

## 2.3 Surfactants

Surface active agent, commonly known as surfactant, is a molecule that has the ability to lower the surface tension between a liquid and another medium, which can be a gas, a liquid or a solid. This effect occurs due to the tendency of these molecules to concentrate at the interface between the two non-miscible media. Some examples of surfactants are, among many others, detergents and emulsifiers (Shaw, 1992; Myers, 1999).

These molecules interact with the surrounding medium in a very particular way: a part of the molecule is strongly attracted to the solvent, receiving the name of lyophilic group, while the other part has little attraction to the solvent, which is called lyophobic group. Most of the information found on literature concerns systems composed of water as solvent so, for this reason, the terms lyophilic and lyophobic are commonly replaced by, respectively, hydrophilic part of the molecule, also called “head”, and hydrophobic part of the molecule, also called “tail”. A representation of this structure is shown in Figure 2.5.

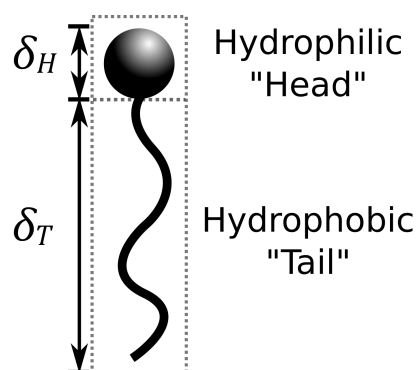


Figure 2.5 – Representation of an amphiphilic molecule.

Molecules that present the same behaviour of surfactants in solution, like the lipids, receive the name of amphiphiles. In general, the hydrophobic part of these molecules is composed of carbonic chains, or another nonpolar structure, and the hydrophilic part is composed of an ionic or a highly polar group. Depending on the characteristics of the hydrophilic “head” of the amphiphile, the molecule can be classified in one of the following categories, where subgroups are defined depending on the nature of the hydrophobic “tail”.

1. Anionic: the “head” has a negative charge;
2. Cationic: the “head” has a positive charge;
3. Nonionic: the “head” has no charge, but it presents a polarisation of charges;
4. Zwitterionic (or Amphoteric): the “head” has a negative and a positive charge.

Because of the so-called hydrophobic effect, when the amphiphiles are dispersed in aqueous solutions the water molecules will solvate the “head” and arrange themselves

around the “tail” in an “ice-like” structure. This organisation has the intention of lowering the contact between the water molecules and the hydrophobic part of the amphiphile, which also makes the global entropy of the system to decrease. This phenomenon is not thermodynamically favourable, and that is the reason why the surfactants are transported to the surface, so the “tail” will no longer be in contact with the solvent and the associated water molecules are released, which makes the free-energy of the system to decrease (Jones, 2002; Israelachvili, 2015).

However, when the concentration of amphiphiles in solution increases, the surface starts to saturate and there is no available space for all the particles and, for this reason, the dispersed amphiphiles tend to aggregate forming many different structures like spherical micelles, cylindrical micelles, inverted micelles, vesicles or bilayers. In all of the self-assembled structures the hydrophilic groups are kept in contact with the water while the hydrophobic chains stay “protected” from it, and the preferred structure for a given amphiphile is dependent on the solvent in which it will be dispersed, the geometry of the molecule, its concentration in the solution and the temperature (Luzzati and Husson, 1962; Fontell et al., 1968; Ekwall, 1975; Ruckenstein and Manciu, 2001).

The only structure of self-assembled amphiphiles studied in this thesis is the bilayer, so the other structures will not be discussed. When dispersed in water, the molecules will form the bilayers that has a thickness  $\delta_L$  approximately equivalent to two times the sum of the lengths of the “head”  $\delta_H$  and the “tail”  $\delta_T$ . These bilayers will stack forming a lamellar phase, separated by a layer of solvent, as represented in Figure 2.6, with a constant distance of repetition  $d$  of the unit cell, also known as lamellar periodicity.

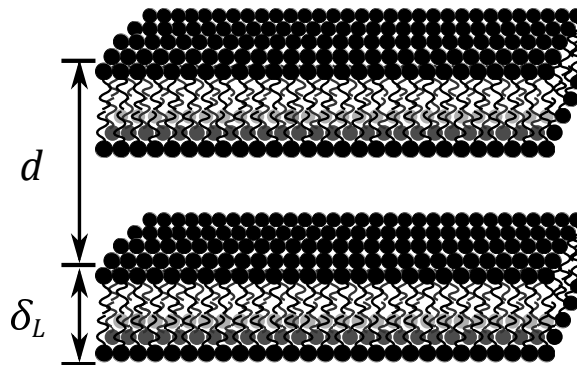


Figure 2.6 – Representation of a smectic A mesophase, formed by the self-assembly of amphiphilic molecules.

This structure is a typical example of a smectic liquid crystal and, as the phase transitions occur with the variation of the concentration, it is classified as a lyotropic liquid crystal. We observe a positional order of the centres of gravity of the amphiphilic molecules in the perpendicular direction to the plane of the layers. If the bilayers are in the fluid phase, also known as  $L_\alpha$  structure, the aliphatic chains are free to move and there is no positional order in the plane of the bilayer. This liquid-like organisation in the plane of the layer is the characteristic that defines the group of smectic A mesophases.

Considering the surfactant bilayers as rigid planes with a constant thickness, also known as geometrical model of the lamellar phase, the thickness of the solvent layers will vary when the concentration of amphiphile in the sample is changed. An increase in the amount of solvent will lead to an increase in the distance of separation of the bilayers and, as the thickness of the bilayers is constant, this is the same as saying that the distance of repetition of the unit cell increases.

This swelling is linearly proportional to the expansion in the volume of the solvent (Fontell et al., 1968; Ekwall, 1975). This phenomenon is called ideal dilution law, which can be expressed by Equation 2.3, where  $d$  is the lamellar periodicity,  $\delta_L$  is the bilayer thickness and  $\varphi$  is the volume fraction of the bilayer. The swelling of lyotropic smectic liquid crystals is very characteristic of bilayers of amphiphiles.

$$d = \frac{\delta_L}{\varphi} \quad (2.3)$$

As mentioned in chapter 1, in this study we investigated the complexes formed with GO and surfactant. The amphiphilic molecule we worked with, whose structural formula is represented in Figure 2.7, is called simulsol.

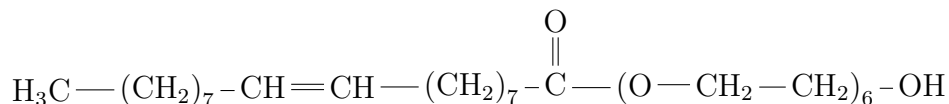


Figure 2.7 – Structural formula of simulsol (oleic acid with 6 monomers of PEG functionalized).

The molecules are composed by an oleic acid in the hydrophobic “tail” with a short polyethylene glycol (PEG) polymer functionalized to it, playing the role of the hydrophilic “head”, containing a fixed number of 6 monomers. The lengths of the hydrophobic and hydrophilic parts of the simulsol can be deduced from the fitting of x-ray scattering data. The estimated values are, respectively,  $0.8 \pm 0.2$  nm and  $2.0 \pm 0.5$  nm (Bougis, 2016). In the next section, the techniques employed to characterise the studied systems will be presented.

## 2.4 Characterisation techniques

In this study a few experimental techniques were employed to characterise the investigated systems, some of them more often than others. The aim of this section of the thesis is not to discuss in details the experiments and their theory, as plenty of high quality texts with this objective can be easily found nowadays in the literature and should be consulted by those who are interested. Basic aspects of these techniques will be briefly introduced to support the discussions of the results.

### 2.4.1 Polarised Optical Microscopy

Polarized Optical Microscopy (POM) is performed in an Olympus BX51 microscope with objectives that can magnify 20x, 40x or 100x. In this study, we use two configurations for the observation of the samples and the obtained images are recorded using a camera, that is not coloured in our case.

1. In order to identify the presence of big particles in the sample, direct observation of the image is implemented.
2. In order to observe if the sample is birefringent, an analyser, which has the same properties of the polarizer, is positioned between the sample and the observer, with the polarisation direction forming an angle between  $0^\circ$  and  $90^\circ$  with the one of the polarizer.

The presence of particles indicates that aggregates of GO sheets are formed and the presence of birefringence indicates an optical anisotropy in the sample, that can be related to a certain level of organisation on the microscopic level of the system. For a more detailed introduction to the optical microscopy, one of the several suggestions would be Bradbury (1989).

### 2.4.2 Transmission Electron Microscopy

The Transmission Electron Microscopy (TEM) images were obtained on a H-600 electron microscope from Hitachi. A tungsten filament emits electrons that are accelerated, forming a beam of electrons that is focused by electromagnetic lenses before being transmitted through the sample. After the interaction with the electrons on the sample, an “electronic image” is obtained and the resulting electron beam is refocused by electromagnetic lenses and magnified to be projected onto a fluorescent screen and this optical image can be recorded by a camera. For more details on the technique a suggestion would be Reimer and Kohl (2008).

### 2.4.3 Dynamic Light Scattering

The Dynamic Light Scattering (DLS) is widely used as a technique to characterise the distribution in size of dispersed particles, generally ranging from  $\sim 1$  nm to  $\sim 10$   $\mu$ m. We carried out the experiments with a research goniometer and a red laser light scattering system working, under controlled temperature, in a wavelength of 644 nm from Brookhaven Instruments Corporation. A basic experimental setup is composed of a laser beam that is aligned in the direction of the sample, passing through a polarizer to define the polarisation of the incident light before reaching it. After impinging the sample, the light can interact with the dispersed particles and, if so, those last ones will emit radiation at the

same wavelength in all the directions, phenomenon known as elastic scattering, or even called Rayleigh scattering for the visible light. This emitted radiation passes through an analyser and the photons with the selected polarisation reach the detector, that is placed in a determined position to quantify the radiation collected.

The detector can be placed in a goniometer, used to rotate this one around the sample, allowing the observation of the intensity in different positions, changing this way the angle between the propagation of the incident and the emitted light, also known as scattering angle  $2\theta$ . The scattering angle can be converted into the scattering vector  $q$ , that is defined as the modulus of the difference between the wave vectors of the scattered and the incident light, respectively. This physical quantity allows one to compare data from different scattering techniques, as it is “normalised” by the wavelength  $\lambda$ , and its magnitude can be calculated by Equation 2.4 where  $n$  is the refractive index of the medium surrounding the particles.

$$q = \frac{4\pi n \sin \theta}{\lambda} \quad (2.4)$$

The information collected is stored in a correlator, that will correlate the fluctuations on the intensity of the detected light at an instant  $t$  and an instant later  $t + \tau$ . These fluctuations are related to the movement of the particles between the respective instants. For systems with a high polydispersity in size, as the dispersions of GO flakes, one can describe the correlation function of the intensity as a function of  $\tau$  using an stretched exponential, given by Equation 2.5, where  $\Delta$  is the characteristic relaxation time, which corresponds to the time for the position of the particles to loose the correlation with the initial position, and the stretching exponent  $\beta$ , that is inserted to take into account the dispersity.

$$C(\tau) = \exp \left[ -2 \left( \frac{\tau}{\Delta} \right)^\beta \right] \quad (2.5)$$

If the dispersion is diluted enough, the suspended particles will not interact with each other, so their movement will be ruled by Brownian motion only. In this case, the diffusion coefficient  $D$  of the particles can be related to the characteristic relaxation time by Equation 2.6 for a given scattering vector.

$$\frac{1}{\Delta} = Dq^2 \quad (2.6)$$

If the scattering angle is varied for a given sample, the evolution of the characteristic relaxation frequency  $1/\Delta$  as a function of the scattering vector can be observed, whose fitting will give a more representative value of  $D$  for the whole domain of accessible  $q$ . From the Stokes-Einstein relation, the hydrodynamic radius  $R_H$  of the particles is obtained, that is given by Equation 2.7, where  $k_B$  is the Boltzmann,  $T$  the absolute temperature and  $\nu$  the viscosity of the medium.

$$R_H = \frac{k_B T}{6\pi\nu D} \quad (2.7)$$

In the case of flat particles, like the GO sheets, the hydrodynamic radius can be described as the hydrodynamic radius of a sphere that would have the same diffusion coefficient. The bigger the particles, the bigger is the equivalent sphere, and we used this property to the analysis that have been done during the study presented here. We did not intended to determine the real size of the GO flakes using DLS, but it is possible to follow the changes on the dimensions of this equivalent sphere when determined parameters are changed. For a detailed theory of DLS one could check Berne and Pecora (2000).

#### 2.4.4 Small Angle X-Ray Scattering

The Small Angle X-Ray Scattering (SAXS) is the main technique adopted to investigate the systems studied in this thesis. Every experimental setup contains a source, which produces x-rays that will be deviated in the direction of the sample, forming a beam of x-rays. During this procedure, the photons with a well defined wavelength will be selected, resulting on a monochromatic beam. As all the sources used in the experiments carried out during this thesis were built with copper, the wavelength of the x-ray beam is 1.5418 Å, which is the most intense wavelength produced by this material. The beam passes then through slits that will eliminate divergent photons, so a collimated beam will impinge on the sample, interacting with it.

Similar to what happens in light scattering experiments, the electrons on the sample can absorb the x-ray radiation and, as it consists on an elastic scattering, also known as Thompson scattering for the wavelength of x-rays, they will emit radiation with the same wavelength in all directions. The x-ray experiments give information about the structure of the sample in the atomic level, a scale that is smaller than what is obtained by light scattering experiments, as the wavelength of x-rays is much smaller than the one of light.

The emitted photons will interfere with each other when reaching the detector, that will collect this radiation. In all the different equipments used in this work, we used 2-dimension detectors, so other types of detectors will not be discussed. The detector will count the number of photons arriving on it and their positions, so we obtain a diffractogram image at the end of the acquisition. After that, this image is integrated, which means that the average number of photons detected for a constant distance to the centre of the direct beam, over the whole azimuthal range, is calculated. This procedure transforms the 2-D information in a 1-D curve, the intensity  $I$  as a function of the distance to the centre or, in other words, the scattering angle  $2\theta$ . Using Equation 2.4, where  $n = 1$  for x-ray experiments, we can convert the scattering angle into scattering vector, obtaining the curve of  $I$  as a function of  $q$ , which will be called spectrum.

The scattering curve contains information about the shape of the scattering units and the interactions between them, if any. In the case of periodic structures, like a lamellar

phase, the interference between the re-emitted radiation will provide peaks in the spectrum, that can be described by Bragg’s law. This law is based on Bragg’s condition, which considers that the radiation emitted by subsequent layers, separated by an interplanar distance  $d$ , will be summed up before reaching the detector, if the electromagnetic waves are in phase, or will be cancelled, if they are out of phase. The waves will be in phase if the path difference between the two of them is proportional to a multiple integer of the wavelength. This phenomenon depends on the incidence angle and, consequently, on the scattering angle. Bragg’s law allows one to determine the interplanar distance from the position of the peaks in the spectrum, using Equation 2.8, where  $q_i$  is the value of the scattering vector for the peak of order  $n_i$  ( $n_i = 1; 2; 3 \dots$ ). For typical spectra of lamellar phases, we can observe that  $q_2/q_1 = 2$ ,  $q_3/q_1 = 3$  and so on.

$$d = \frac{2\pi n_i}{q_i} \quad (2.8)$$

In the case of other structures, this relation is not true, but these structures will not be discussed in this text. For more information concerning scattering techniques one could see Lindner and Zemb (2002). However, a more detailed description of the theory of the scattering curves of GO sheets and the obtained structures will be discussed in chapter 4.

Three different equipments were used during the work here presented and they will be presented below.

1. Most of the diffractograms were recorded on a Bruker-SAXS Nanostar machine equipped with a Hi-Star detector, also from Bruker (Karlsruhe, Germany). After collimation, the incident beam size is 0.43 mm in both vertical and horizontal directions at the sample position. Two distances between the sample and the detector are used, depending on the range of  $q$  wanted. The configuration called “small-angle”, where the distance is 1.05 m, allows the access of scattering vectors from  $0.01 \text{ \AA}^{-1}$  to  $0.2 \text{ \AA}^{-1}$ , and for the “large-angle” one, where the distance is 0.25 m, the window is from  $0.04 \text{ \AA}^{-1}$  to  $0.8 \text{ \AA}^{-1}$ . The calibration is done using silver behenate as standard and from the Gaussian width of the first order Bragg peak we estimate a resolution width (FWHM) of  $\Delta q \approx 5 \times 10^{-2} \text{ \AA}^{-1}$  and  $\Delta q \approx 6.0 \times 10^{-3} \text{ \AA}^{-1}$  for the two configurations, respectively (Huang et al., 1993). The path between the source and the detector is evacuated and the sample temperature, kept at  $20 \text{ }^\circ\text{C}$  for our experiments, is controlled by a water circulation system. Acquisition times are in the order of 5 hours.
2. To have access to even higher scattering vector values, technique known as Wide Angle X-Ray Scattering (WAXS), a custom-made instrument with a rotating anode from Rigaku (Tokyo, Japan) and a mar345 image plate detector (marXperts, Norderstedt, Germany) is used. The distance between the sample and the detector is 0.15 m, also calibrated with silver behenate, giving access to  $q$  ranging from

0.5  $\text{\AA}^{-1}$  to 3.3  $\text{\AA}^{-1}$ . Only the path between the source and the sample is evacuated and the temperature is controlled by the air-conditioning in the room. Acquisition times are in the order of 1 hour.

3. For very specific measurements, that will be discussed in chapter 4, a Nanostar equipment located in the Institute of Physics of the University of São Paulo (Brazil) was used. The machine operates with a Vantec-2000 detector from Bruker, and a Genix3D source with a FOX3D focusing system, both from Xenocs (Sassenage, France). The sample to detector distance is 0.67 m, giving a  $q$  range from 0.01  $\text{\AA}^{-1}$  to 0.35  $\text{\AA}^{-1}$ . The path between the source and the detector is evacuated and the sample temperature, kept at 20 °C for our experiments, is controlled by a water circulation system. The final curve is obtained with the average of 10 frames of 30 minutes each.

Those techniques will help to characterise the aqueous graphene oxide dispersion. In the next chapter, the results of these experiments will be presented and, exploiting all the presented information, we can interpret them to better understand the investigated system.



# Chapter 3

## Highly concentrated dispersions of graphene oxide

### 3.1 Characterisation of the GO sheets

As briefly described in section 1.2, in order to reach the objectives proposed in this thesis, we started studying the binary system composed of GO sheets dispersed in water. Different sources of GO were tested, in particular, dried forms of GO layers, which were obtained as films or powder, this last one the result of the lyophilisation of a diluted solution. The advantage of using dried forms is a better—and easier—control of the concentration of the prepared dispersion when water is added to the sample.

Because of its porous form, we observed that it is easier to hydrate the GO powder than hydrating the film. However, it is possible to observe particles, which can be seen with the naked eye, suspended in the dispersions prepared with both sources. These grains are presumably formed by GO sheets that aggregated when the material was dried and cannot be separated by a simple hydration, so the heterogeneous dispersions were submitted to an ultrasonic treatment to “break” these aggregates.

After sonication, the aggregates are no longer visible with the naked eye, which suggests that the larger aggregates were separated into monolayers that are dispersed in the solvent. However, a secondary effect observed after the sonication of the dispersions (as monitored by DLS) is a decrease in the average lateral size of the “free” sheets. These samples were also observed under POM and, for these observations, the samples can be prepared in two different ways, depending on their concentrations.

1. For diluted GO dispersions (mass fraction around 10 mg/mL and below), microslides with a constant optical path varying from 0.2 mm to 0.8 mm are soaked into the dispersion. By capillary forces, the sample will fill the microslide and the ends of the microslides are flame sealed to avoid evaporation of water.
2. For more concentrated (significantly more viscous) dispersions, the samples are sandwiched between a microscope slide and a cover slip, both in glass, and then sealed

with UV-curing glue to prevent the evaporation of water. In this case, the optical path is not constant, but is estimated to be smaller than 0.01 mm.

The POM images obtained for two of the dispersions prepared with the lyophilised powder at different concentrations are shown in Figure 3.1. It is possible to observe the presence of GO aggregates even after the sonication procedure and, as one can expect, the higher the concentration, the higher the amount of these aggregates in the sample.

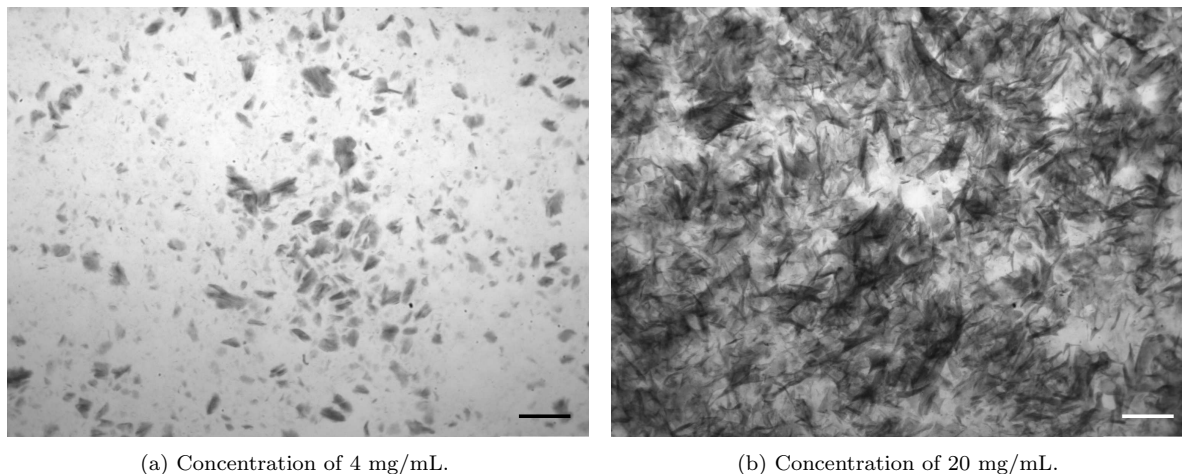


Figure 3.1 – POM images of aqueous dispersions prepared with lyophilised GO. The scale bars are equivalent to 100  $\mu\text{m}$ .

Considering these results, we concluded that, for the work to be developed in this thesis, the dispersions prepared from dried sources of GO are not convenient, because of the presence of aggregates. For this reason, we tested another source of GO sheets, which consists on a solution commercialised by Graphenea company (San Sebastian, Spain).

The commercial dispersion presents a nominal concentration of 4 mg/mL with more than 95% of carbon monolayers, containing an amount between 41 and 50% of oxygen atoms (Graphenea, 2014). The presence of these oxygen groups gives an acid character to the solution, with a  $p\text{H}$  in the order of 2.4. According to the provider, the dispersion is produced using Hummers and Offeman's method (1958), which provides a large amount of graphene layers with a high polydispersity in size. In order to compare this source of GO sheets with the dried ones, we have also observed the solution in POM and the obtained images are shown in Figure 3.2.

This time, no aggregates are observed in the sample, as one can see in the image obtained in direct observation (Figure 3.2a). From the image obtained with crossed polarizer and analyser (Figure 3.2b), we can observe the presence of birefringence, indicating a certain level of organisation in the system.

To better characterise the commercial dispersion, TEM images of the GO sheets were obtained and are shown in Figure 3.3. The samples are prepared by diluting the commercial GO dispersion and depositing a small quantity in a copper grid coated with Formvar® and carbon. The grid is then placed in a vacuum chamber for the water to evaporate at room temperature. This procedure allows to obtain a very thin sample, a condition that

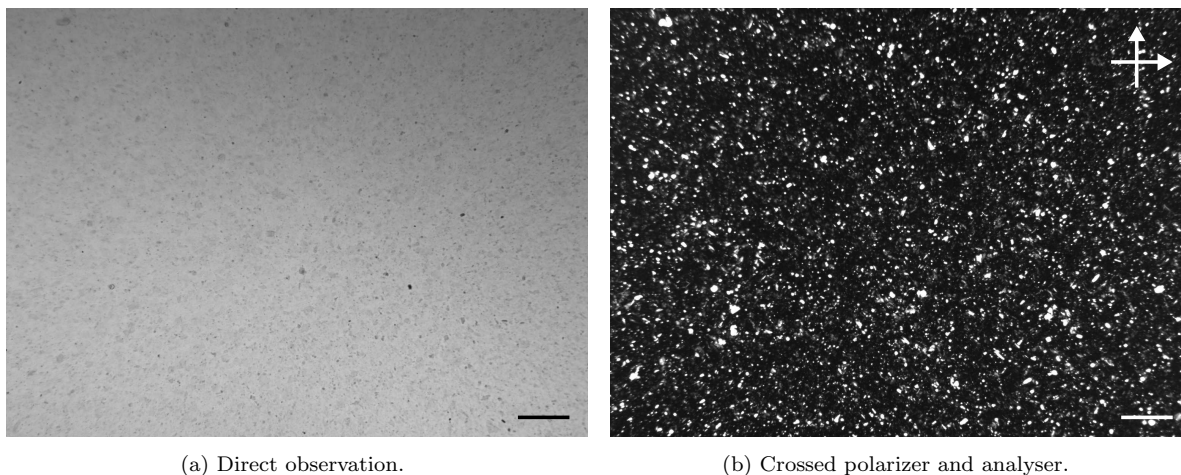


Figure 3.2 – POM images of commercial GO aqueous dispersions. The scale bars are equivalent to  $100\ \mu\text{m}$ .

is necessary for the experiment.

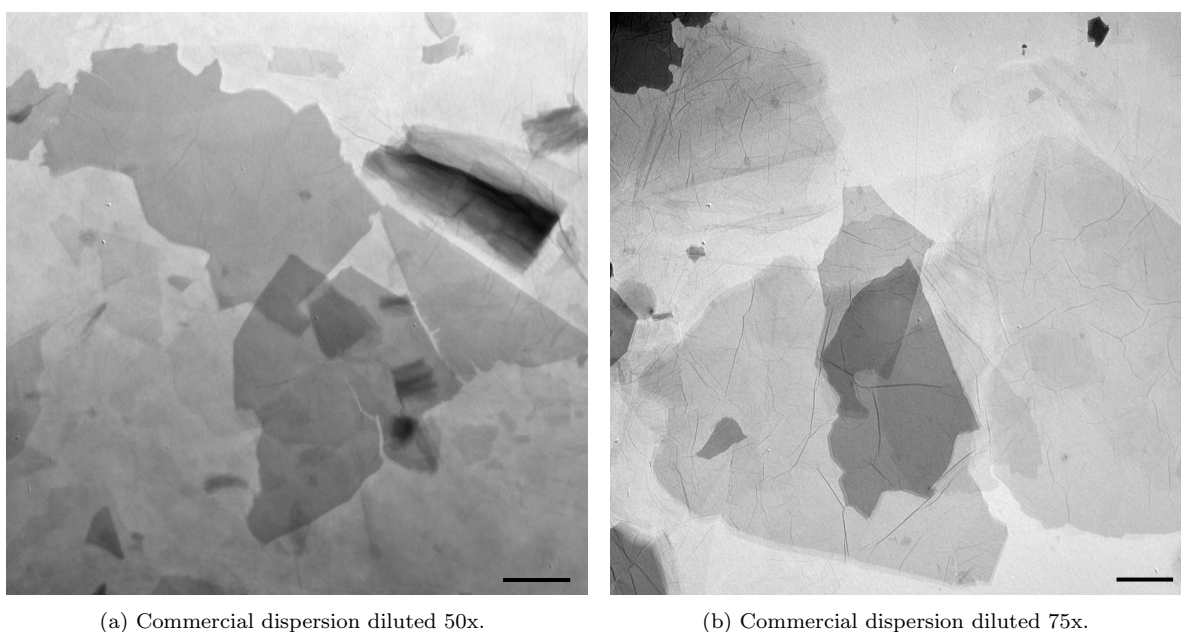


Figure 3.3 – TEM images of GO sheets. The scale bars are equivalent to  $2\ \mu\text{m}$ .

The TEM experiments show the presence of monolayers and, as already mentioned, these GO layers are very polydisperse. In the image obtained for the commercial dispersion diluted 50x (Figure 3.3a), it is possible to observe large sheets, with a maximum length of  $\approx 10\ \mu\text{m}$  and a few smaller ones, with a maximum length no larger than  $1\ \mu\text{m}$ .

As the shape of the layers is not regular, it is difficult to determine their sizes, however, we can consider the maximum length of a layer as its lateral size. A few grids from the same dispersion were observed in TEM and the images analysed, so the distribution of sizes over almost 200 GO sheets can be obtained, as showed in Figure 3.4.

To have a more quantitative analysis of the dimensions of the GO sheets, we can consider a log-normal distribution for the size of the GO layers. From the fitting, we obtain a mean size of  $2.3\ \mu\text{m}$ , with a standard deviation of  $2.2\ \mu\text{m}$ . The median value

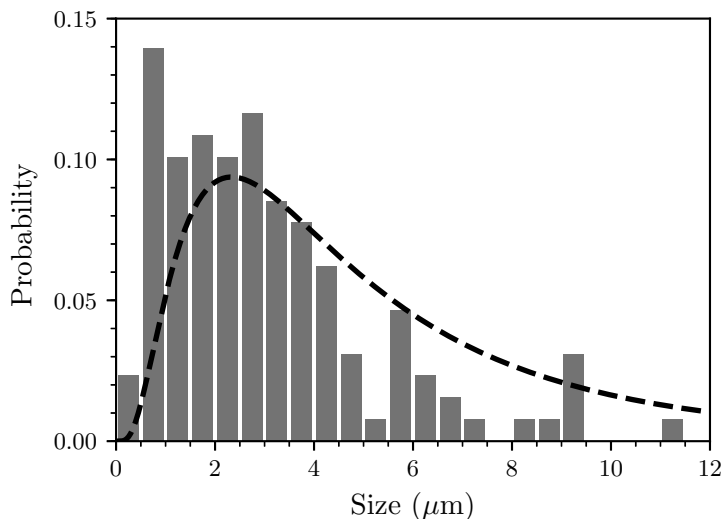


Figure 3.4 – Probability distribution and probability density function of the size of GO layers.

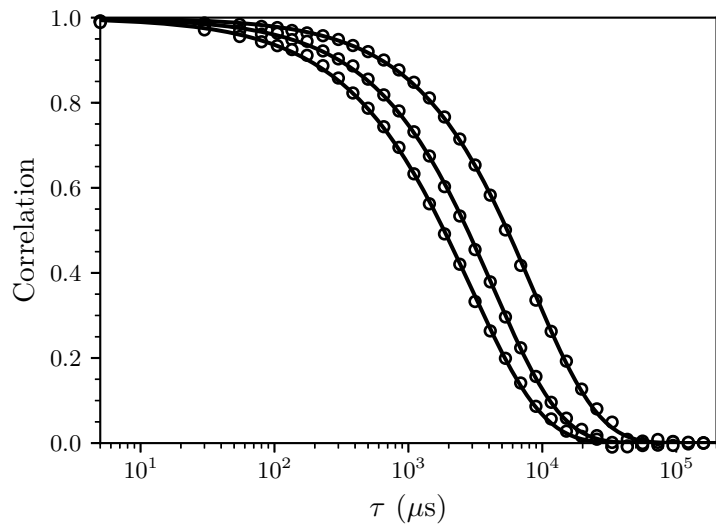
is  $2.7 \mu\text{m}$ . These results confirm the high polydispersity in size of the GO sheets. The average size found is compatible with the information provided by the company.

Another technique useful to characterise the dimensions of particles in suspension is DLS. In Figure 3.5, the obtained results for the characterisation of the commercial dispersion using this technique are shown. For this study, two batches of commercial dispersion were used. The dispersion is diluted 100 times, reaching a concentration around  $40 \mu\text{g}/\text{mL}$ , to have a condition where the interactions between the sheets are negligible.

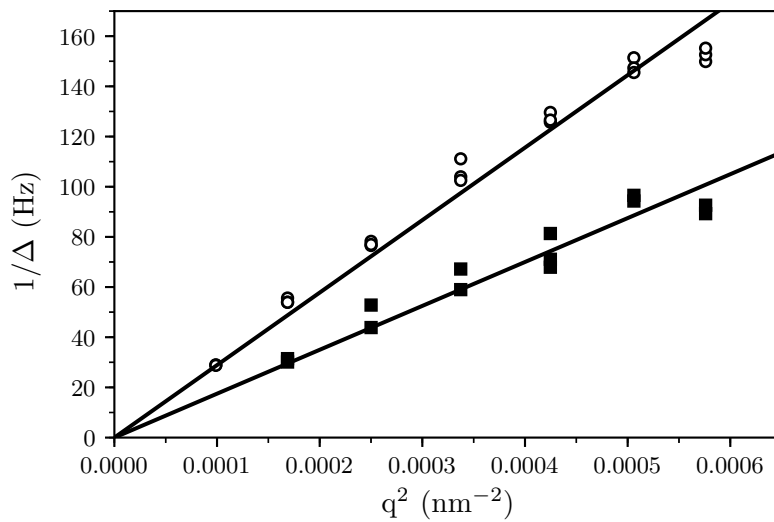
Figure 3.5a shows the correlation functions obtained in three different scattering angles for one of the analysed batches of GO dispersion. One can observe that the stretched exponential model that was presented in subsection 2.4.3, describes adequately the curves. From the fittings of each one of the correlation functions for the two batches, the extracted parameters are plotted in Figure 3.5b and Figure 3.5c.

One can observe from the curves fitted in Figure 3.5b that  $1/\Delta$  is proportional to  $q^2$ , which means that the conditions to have only Brownian motion are valid and an average hydrodynamic radius can be determined for the GO layers. From the diffusion coefficient and the Stokes-Einstein relation, considering the experimental conditions, the hydrodynamic radii are calculated and we obtain  $0.74 \mu\text{m}$  and  $1.22 \mu\text{m}$  for each one of the batches.

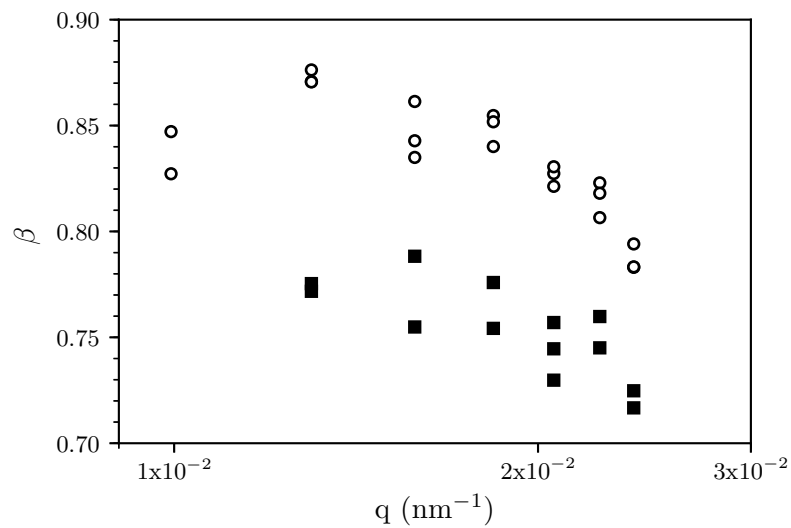
We do not intend to discuss in this work the quantitative relation between the hydrodynamic radius of a flat, not necessarily rigid particle of irregular shape and its effective lateral size. However, we can notice that the obtained values by the scattering technique are close to the one obtained by TEM distribution. Another important information that can be extracted from the experiment is the value of the exponent  $\beta$ , that indicates how much stretched is the fitted exponential. In Figure 3.5c one can observe that this parameter decreases as the scattering angle increases, with values varying from 0.71 to 0.88,



(a) Correlation functions of a GO dispersion fitted with the stretched exponential model for three different scattering angles.



(b) Characteristic relaxation frequency as a function of the scattering vector for two batches of commercial GO dispersions.



(c) Exponent of the stretched exponential as a function of the scattering vector for two batches of commercial GO dispersions.

Figure 3.5 – DLS results for GO dispersions.

which also indirectly demonstrates that the dispersions are polydisperse.

These findings show that the DLS technique can give a comparative information about the dimensions of the layers for different suspensions, with the advantage of increasing substantially the statistics of the analysis. This can also help to characterise the evolution (ageing) of a given dispersion.

We have observed that the GO layers tend to reduce when exposed to light or high temperatures. When this happens, the layers are no longer fully dispersible in water and two of the observable consequences of this phenomenon are: the increasing in the viscosity of the sample and the formation of aggregates. For this reason, three different ways of storing the samples were tested by DLS and they are described below.

1. The commercial dispersion is stored for ageing and a specimen is diluted to the appropriate concentration, just before the experiment to be carried out.
2. The commercial dispersion is diluted to the appropriate concentration for the experiment and stored for ageing.
3. The commercial dispersion is concentrated (see section 3.2) and stored for ageing. A specimen is diluted to the appropriate concentration just before the experiment to be carried out.

In order to control the ageing of the GO dispersions and evaluate the best way to store the samples, the DLS experiments were carried out to investigate their evolution in time and the results are presented in Figure 3.6.

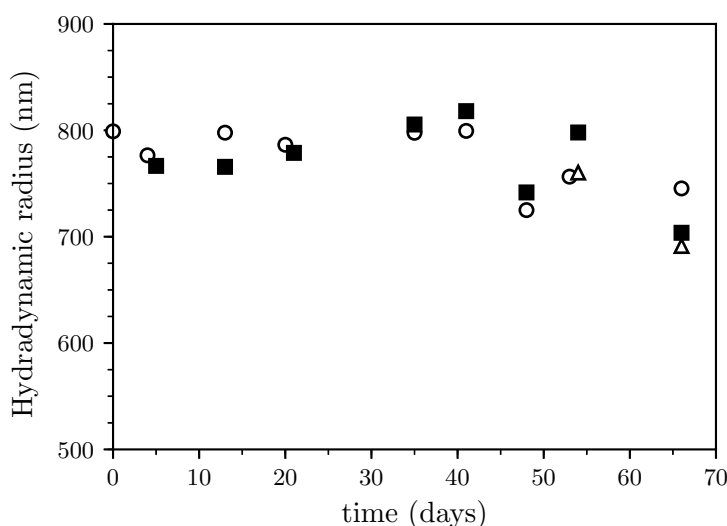


Figure 3.6 – Evolution of the GO layers hydrodynamic radii obtained from DLS for the commercial (o), diluted (■) and concentrated (△) dispersions stored for ageing.

It is possible to observe that changing the storage condition (always avoiding direct light, and at room temperature) does not interfere in the obtained results, which means

that the presented conditions are equivalent from the DLS characterisation. The DLS experiments also show no significant ageing after two months.

All these results show that the commercial dispersion is a convenient source of GO for our experiments. Nevertheless, it has a very low concentration for the work to be developed and, for this reason, a procedure to concentrate the dispersions, keeping the properties of the GO layers, had to be developed.

## 3.2 Preparation of highly concentrated GO dispersions

In order to obtain highly concentrated samples from the commercial dispersion, we had to develop a procedure that keeps the GO sheets hydrated throughout all the steps, as we already showed that dried sources are not appropriate for the objectives of this thesis. The first step of the procedure consists on centrifuging the sample at  $1400g$  for about 20 minutes, with the objective of diminishing the possibility of finding large aggregates in the samples, if any. After this procedure, the supernatant is recovered and the pellet material, where the large particles are deposited, is discarded.

The recovered dispersion is then ultracentrifuged at  $302000g$  for typically 5 hours. This time, the bottom phase, consisting on an almost black viscous paste, is recovered and the supernatant, consisting on almost only water, is discarded. We have verified that for longer centrifugation durations, no increase in the final concentration is observed and, as the maximum speed of the ultracentrifuge was reached, it is not possible to concentrate even more the dispersions using this method. The concentrated dispersions are stored in closed tubes at  $4^{\circ}\text{C}$  for one week, in order to homogenise the samples. In Figure 3.7 we show POM images obtained for a concentrated GO dispersion.

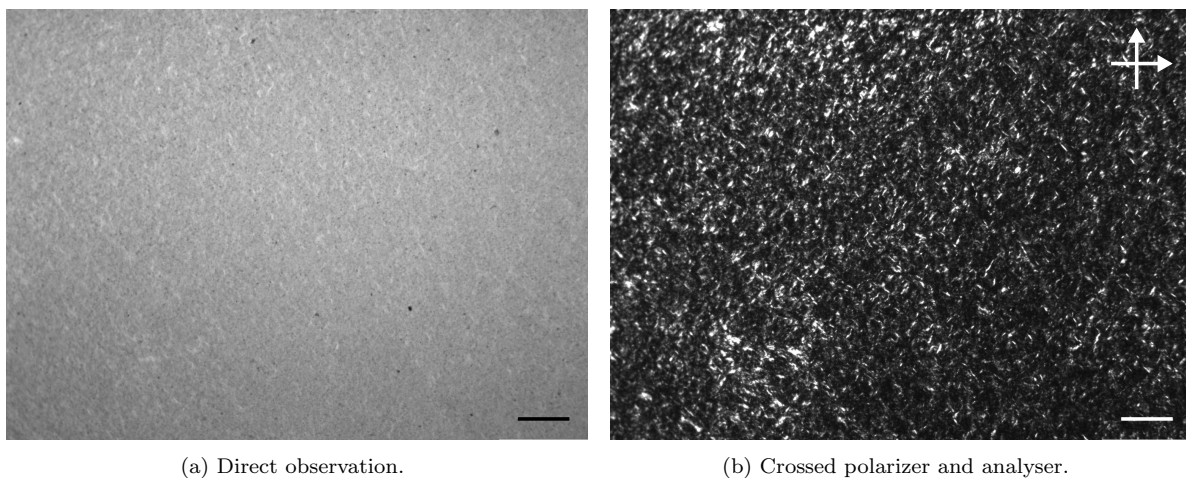


Figure 3.7 – POM images of a concentrated GO aqueous dispersion. The scale bars are equivalent to  $100\ \mu\text{m}$ .

It is possible to observe that the obtained images, though with a much smaller optical path, are very similar to the ones obtained for the commercial dispersion before the

concentration procedure. This means that even after an ultracentrifugation, no large aggregates are formed and the sample is still birefringent.

After homogenisation, a new step to obtain even more concentrated dispersions starts. A device consisting on a diaphragm pump connected to a pressure controller and a desiccator, designed in the laboratory and showed in Figure 3.8, is used to concentrate the dispersion.



Figure 3.8 – Device developed in the laboratory to dehydrate aqueous GO dispersions. From the left to the right: vacuum pump, pressure controller and vacuum chamber.

Small tubes containing the concentrated dispersion are opened and placed into the vacuum chamber, where the pressure is kept constant at 300 mbar and at room temperature, controlled by an air conditioning system regulated to 22°C, to avoid the aggregation of the sheets due to thermally-induced reduction of the GO layers. Note that exposure to direct light is also avoided in our device. In these conditions, the water will slowly evaporate and, as a consequence, the concentration of the dispersion will increase.

The mass loss is controlled by stopping the evaporation, closing the tubes and weighing the samples. A few cycles of (mild) centrifugation can be applied, if necessary, to homogenise the sample during this step. The procedure of dehydration is considered to be completed when there is no more variations in the mass of the sample.

The remaining water molecules are strongly bounded to the GO layers: a few “dry” samples have been submitted to even lower pressures, but no mass changes were observed, which means that the dispersion reached its driest state accessible with our setup.

From SAXS experiments (see subsection 2.4.4 and section 3.3) it is possible to obtain the lamellar periodicity of the GO dispersion for variable amounts of water. With this information and using Scholz and Boehm (1969) calibration curve (Figure 2.2), one can determine the water amount in the sample and calculate, retrospectively, the initial GO mass fraction. The evolution of the GO mass fraction as a function of the dehydration time for three of the dispersions is shown in Figure 3.9.

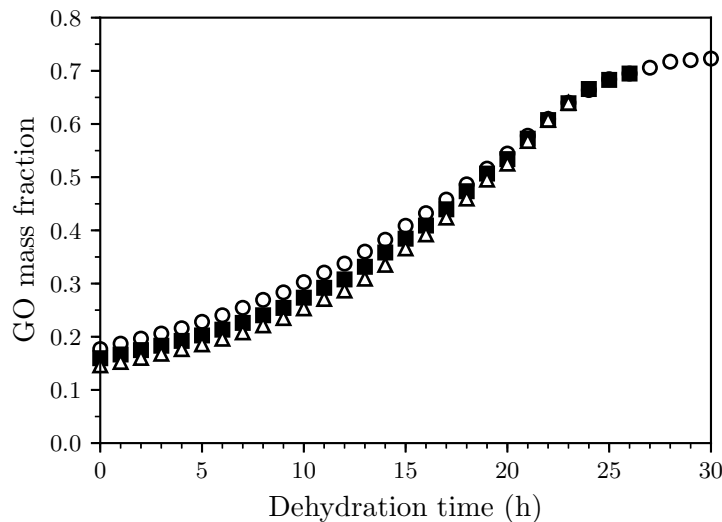


Figure 3.9 – GO mass fraction as a function of the dehydration time in the vacuum chamber for three samples.

We observe that the amount of GO in the driest accessible sample is a little higher than 70% in mass. A small variation in the initial concentration of the three analysed dispersions is observed and we can estimate the mass fraction of a ultracentrifuged GO dispersion to be  $f_m = 0.160 \pm 0.015$ .

In addition, a fully dehydrated sample was rehydrated, until it reached the initial mass fraction after ultracentrifugation, with the objective of comparing the properties of the ultracentrifuged dispersion before and after the dehydration procedure. After waiting one week for homogenisation, the redispersed sample was observed under POM and the obtained images are equivalent to the ones showed in Figure 3.7, for the ultracentrifuged dispersion, revealing the absence of aggregates and an optically anisotropic sample. Both samples were also investigated by SAXS and the obtained spectra are shown in Figure 3.10.

One can see that the maximum values of intensity from each curve differ, which is probably due to the correction procedure and experimental artefacts (see section 3.3). However, the shapes of both curves are very similar, with a peak at practically the same position, which means that the systems have the same lamellar periodicity, given by Equation 2.8, *i.e.*  $d \approx 6.5$  nm.

All the observations reported in this section show that the procedure to obtain highly concentrated aqueous GO dispersions, developed during this thesis, is very efficient and chemical modifications, if any, on the GO layers are not significant during the drying process. The obtained dispersions are free of aggregates, which is not the case for dried samples, and the concentration procedure is completely reversible presumably because the sample does not reach the driest state. The production of these samples allows the access to an unexplored confined regime of this system, which can now be investigated.

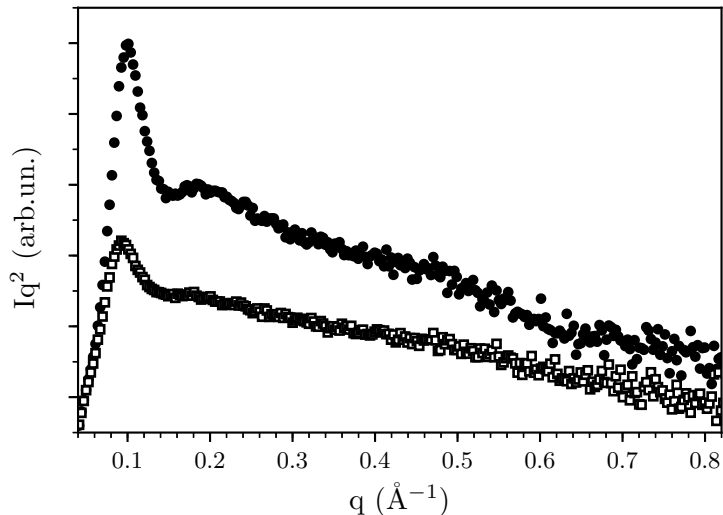


Figure 3.10 – SAXS spectra of an ultracentrifuged (●) and a rehydrated (□) GO dispersion at the same final concentration. Data shifted vertically for a better visualisation.

### 3.3 Structural characterisation of highly confined GO sheets in water

For the characterisation of the phases obtained with highly concentrated aqueous GO dispersions, ultracentrifuged samples were separated in different tubes that were placed in the vacuum chamber, following the procedure already discussed in the previous section. Each one of the tubes was removed from the desiccator after different durations, providing samples with concentrations varying along the dehydration curve. In addition, a few samples were prepared by diluting the ultracentrifuged dispersion, in order to obtain less concentrated samples, but with a higher GO mass fraction than the commercial dispersion.

After homogenisation of the prepared samples, they were observed in POM. For highly dehydrated samples, it was not possible to obtain thin enough samples that remained too opaque for the observations. However, samples containing up to 50% of GO in mass were always birefringent, indicating a certain level of organisation in the system, and clear images indicated the absence of aggregates.

All the prepared samples were also analysed by SAXS, which is the main technique used in this thesis to characterise the organisation of the GO layers in the system. In addition to the different equipments used for the measurements (see subsection 2.4.4), the experiments were also carried out in two different conditions, which are described below.

1. For dispersion less concentrated than  $f_m = 0.15$ , the sample is inserted directly into a quartz capillary with nominal diameter of 1.5 mm. The capillary can be softly centrifuged for the sample to reach the bottom and it is flame sealed to avoid evaporation.

2. For more concentrated dispersions, the sample is inserted in a support of stainless-steel that is introduced into a quartz capillary with a nominal diameter of 2.5 mm. The support has a cylindrical shape, measuring  $2.0 \times 20.0$  mm, with a circular hole, in the perpendicular direction to the long axis of the cylinder, for the sample to be spread, measuring 1.3 mm of diameter. The capillary is flame sealed to avoid evaporation.

Besides the conditions of preparation of the capillaries, there is no difference between the experiments carried out with a diluted or a concentrated sample. The SAXS measurements are then performed for each one of the samples and selected, but representative results are shown in Figure 3.11.

In Figure 3.11a and Figure 3.11b, the typical 2D diffractograms of dehydrated dispersions are presented. It is possible to observe a slight orientation in the images, probably due to the shear applied to the sample when the capillary or the cylinder support are filled. The images are azimuthally averaged and the curves of intensity as a function of the scattering vector are obtained.

Nevertheless, the scattered radiation contains information not only from the GO sheets, but also from the solvent and the capillary. In order to remove these undesired informations from the curves, a correction procedure is implemented. A spectrum of the capillary filled with the solvent (or an empty capillary for the highly dehydrated samples) is obtained and its intensity subtracted from the intensity of the ensemble.

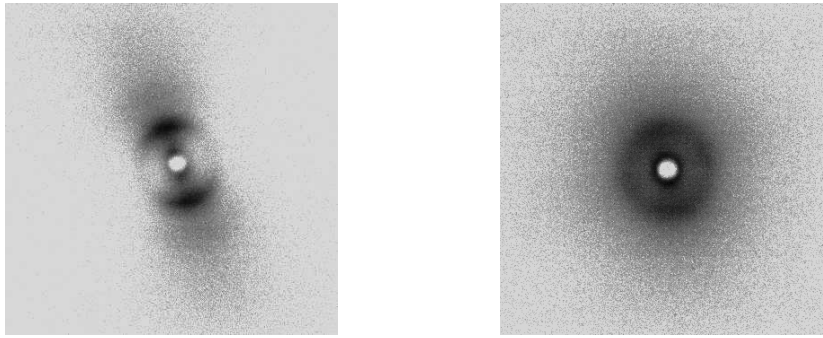
The final intensity  $I_f$  as a function of  $q$  is obtained using Equation 3.1, where  $I_s$  and  $I_b$  are, respectively, the intensities of the sample and background and  $f_c$  is the correction factor, which is defined as the maximum value for the intensity curve to be strictly positive.

$$I_f(q) = I_s(q) - f_c I_b(q) \quad (3.1)$$

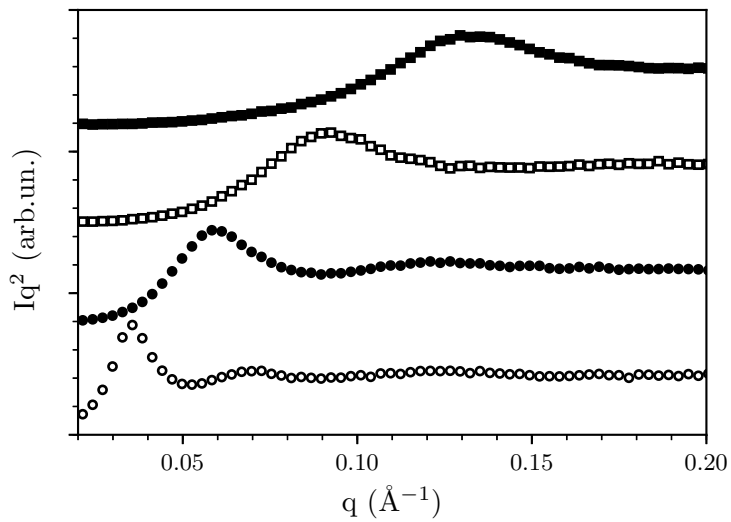
In Figure 3.11c and Figure 3.11d, the plots of corrected spectra obtained for some of the dehydrated samples are presented, those being vertically shifted to facilitate the visualisation. Between both groups of curves, the setup was changed to allow the access of different ranges of  $q$ , depending on the concentration of the samples.

One of the first things that can be observed is the plot of the curves in the Kratky representation, which is obtained by drawing  $Iq^2$  as a function of  $q$ . This particular way of exhibiting the data highlights the decrease of the intensity proportional to  $1/q^2$ , characteristic of flat particles with random orientation, which is the case of GO sheets in suspension.

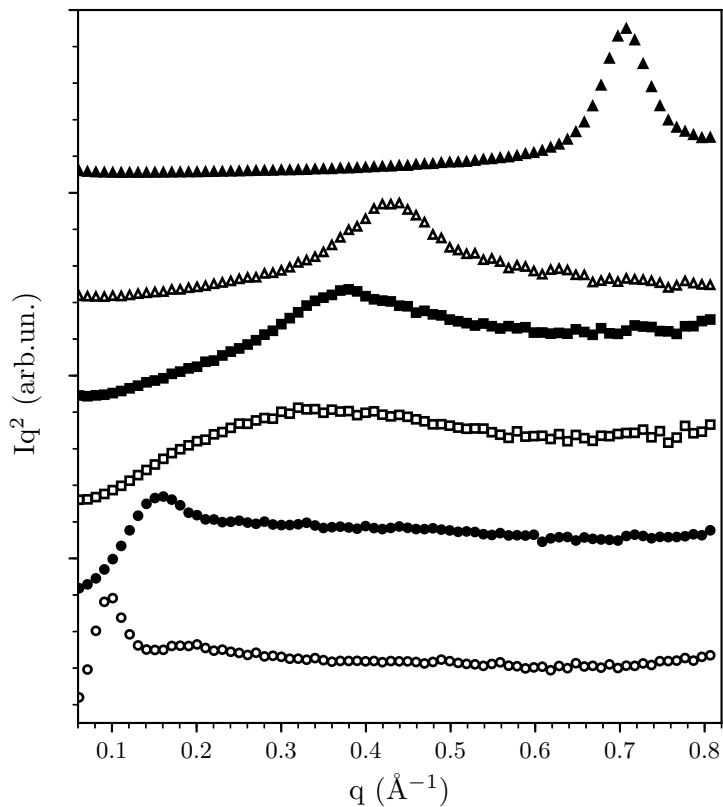
It is also possible to observe the presence of at least one peak of intensity in each curve and, the higher the concentration of GO in the dispersion, the higher is the position of the peak in scattering vector. Besides, a behaviour that is evidenced in Figure 3.11d is the broadening of the peaks with the dehydration, specially for intermediate samples, while this behaviour is reversed when the maximum concentration limit is approached.



(a) Diffractogram of a dispersion with  $f_m = 0.04$ . (b) Diffractogram of a dispersion with  $f_m = 0.16$ . Intensity is in log scale.



(c) Spectra in a smaller range of  $q$  for dispersions with  $f_m$ : 0.04 ( $\circ$ ), 0.07 ( $\bullet$ ), 0.10 ( $\square$ ) and 0.14 ( $\blacksquare$ ).



(d) Spectra in a larger range of  $q$  for dispersions with  $f_m$ : 0.12 ( $\circ$ ), 0.16 ( $\bullet$ ), 0.21 ( $\square$ ), 0.26 ( $\blacksquare$ ), 0.38 ( $\triangle$ ) and 0.62 ( $\blacktriangle$ ).

Figure 3.11 – SAXS results of dehydrated GO dispersions. Data shifted vertically for a better visualisation.

The spectra of the less concentrated dispersions, for both configurations, show the presence of two peaks, whose positions follow Bragg's condition given by Equation 2.8, indicating that the GO sheets are organised in periodically stacked layers, which characterises a lamellar phase. The second order peak, that is barely seen in more dehydrated samples, disappears when the first order peak gets broader, even if its eventual position is still visible in the  $q$  range investigated.

However, the upper limit in  $q$  with the NanoStar set-up is smaller than the expected position of the second order peak for the very dehydrated samples. For this reason, the most concentrated sample, with  $f_m = 0.79$ , was analysed in a much larger window of observation and its spectrum is shown in Figure 3.12.

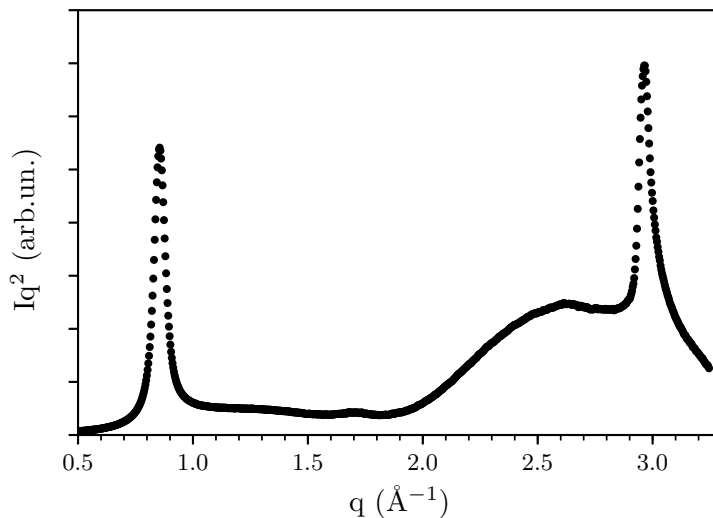


Figure 3.12 – X-ray scattering spectrum of the driest GO dispersion with  $f_m = 0.79$ .

We can observe the presence of the first order peak at  $q = 0.85 \text{ \AA}^{-1}$ , which gives a lamellar periodicity of  $7.4 \text{ \AA}$ . The second order peak is also visible, although weak in intensity, at  $q = 1.71 \text{ \AA}^{-1}$ , corresponding to what is expected from Bragg's condition for a lamellar phase.

A hump is observed at  $q \approx 2.6 \text{ \AA}^{-1}$ , whose origin is presumably due to the correction procedure and experimental artefacts. In addition, another strong peak is observed at  $q = 2.96 \text{ \AA}^{-1}$ , which is related to the distance between the nearest neighbour carbon atom  $d_{CC}$  in the graphene layer. From the relation given by Equation 3.2, we obtain a distance of  $1.4 \text{ \AA}$ , which is compatible to the value obtained from the literature for  $d_{CC}$  (see section 2.1).

$$\sqrt{3}d_{CC} = \frac{4\pi}{\sqrt{3}q} \quad (3.2)$$

These observations show that, even after a high dehydration, the GO sheets are still organised in periodically stacked layers and the structure of the graphene in the plane of the layers is conserved. The curve obtained for the driest samples can be compared to

the one obtained for the natural graphite (Graflake 99550 - Nacional de Grafite LTDA, Brazil), which is shown in Figure 3.13.

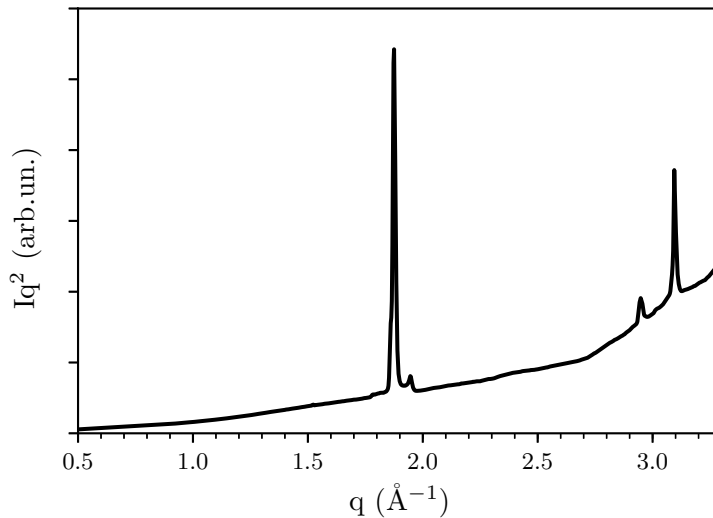


Figure 3.13 – X-ray spectrum of natural graphite.

It is possible to observe the characteristic peak of the nearest neighbour carbon atoms  $d_{CC}$  in the graphene layer plane and a sharp peak at  $q = 1.87 \text{ \AA}^{-1}$ , corresponding to a lamellar periodicity of  $3.36 \text{ \AA}$ , which is very close to the spacing between the graphene layers in the graphite. Two other small peaks are observed, probably due to impurities in the sample.

The results shown above confirm that the organisation of the driest GO sample is very similar to the one of graphite. The layers have the structure of graphene with an interlayer spacing two times higher than the spacing in graphite, which is probably due to the oxygen groups in the surface of the graphene oxide and the remaining water molecules, corroborating the observations for the dehydration curve.

Considering that the GO aqueous dispersion is organised in a lamellar phase throughout all the dehydration curve, it is possible to determine the periodic spacing of the lamellar phase as a function of the concentration. Moreover, we can compare the behaviour of the lamellar structure with the ideal swelling law of lyotropic smectic liquid crystals, converting the GO mass fraction into GO volume fraction.

The conversion can be done using the mathematical relation given by Equation 3.3, where  $\varphi$  is the GO volume fraction,  $f_m$  the GO mass fraction and  $\rho_g$  and  $\rho_w$  the GO and water densities, respectively.

$$\varphi = \frac{1}{1 + \left(\frac{1}{f_m} - 1\right) \frac{\rho_g}{\rho_w}} \quad (3.3)$$

From the SAXS spectra obtained for all the dehydrated samples, it is possible to determine the position of the Bragg's peaks and, using the relation given by Equation 2.8,

calculate the lamellar periodicity  $d$  for each one of the curves. Additionally, with the conversion of the concentration in volume fraction  $\varphi$ , we can plot the curves of  $d$  as a function of  $1/\varphi$ , as presented in Figure 3.14.

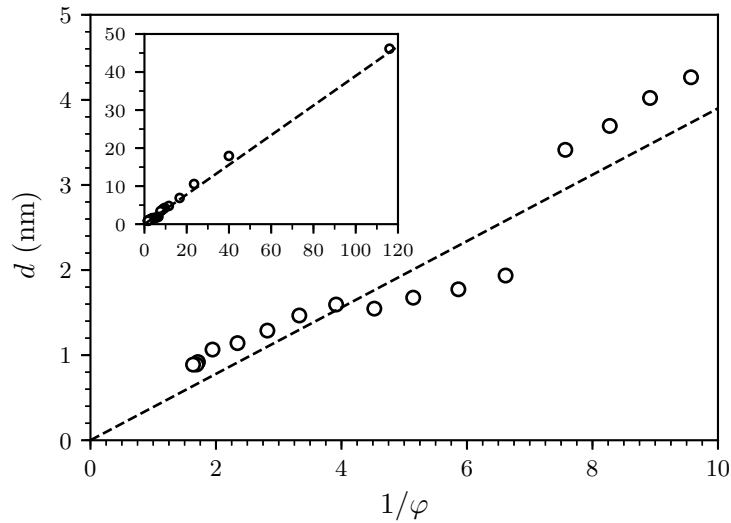


Figure 3.14 – Lamellar periodicity as a function of the inverse volume fraction for GO dispersions. Inset: *idem* for the whole investigated dilution range. The dashed line corresponds to the swelling law expressed by Equation 2.3, with  $\delta = 0.39$  nm.

One can observe that the ideal swelling law, given by Equation 2.3, convincingly describes the global behaviour of the GO dispersion. This observation shows that, in the conditions here presented and in the range of concentration investigated, this system can be considered as a lyotropic liquid crystal, with the formation of smectic mesophases (see section 2.3). This phenomenon is schematically represented in Figure 3.15.

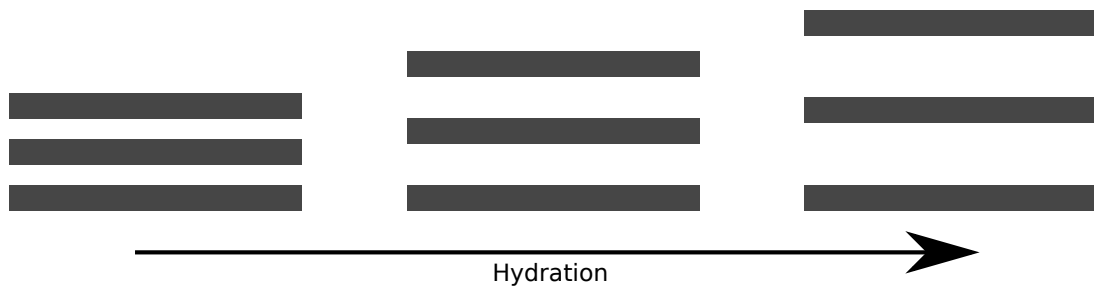


Figure 3.15 – Schematic representation of the swelling of GO sheets lamellar structure. The amount of solvent increases from the left to the right.

The fitting, using the dilution law in the whole range of available volume fractions, gives a slope of 0.39 nm, which corresponds to the geometrical thickness of the GO layers. This value is very close to the one obtained for the thickness of a graphene layer, which shows that this method is consistent with previous observations.

Nevertheless, making a zoom in the concentrated domain of the GO aqueous dispersions, we observe marked irregularities, and even a disparity in the dilution curve when  $\varphi$  is close to approximately 0.14. The gap on the swelling curve corresponds to the domain

at which the broadening of the first order peak in the SAXS spectra is observed, indicating a possible structural phase transition. This transition remains to be characterised in details.

The results obtained with the SAXS experiments showed that, for a small domain of concentrated aqueous GO dispersions where the peaks get broader and the ratio between the intensities of the first and second order peaks decreases, a structural transition probably takes place. Still, this system forms a periodically stacked structure throughout the whole studied dilution range, globally following the characteristic swelling law of lyotropic liquid crystals. After investigating the structure of the system, we can study the interactions that stabilise the lamellar organisation.

### 3.4 Effect of salt on interactions between GO sheets

As already mentioned, the swelling observed for lamellar phases of GO is a common phenomenon for layered systems like self-assembled bilayers of surfactants. This behaviour is controlled by the balance of the direct interactions between the layers and within the layers with the entropic penalty of layers being ordered. When water is added to the system, the layers get apart from each other, due to the direct, if any, or effective (entropy-driven) repulsive interactions. An equilibrium along the dilution line, with excess water coexisting with the lamellar stack may be reached if the attractive (van der Waals) and repulsive forces become balanced.

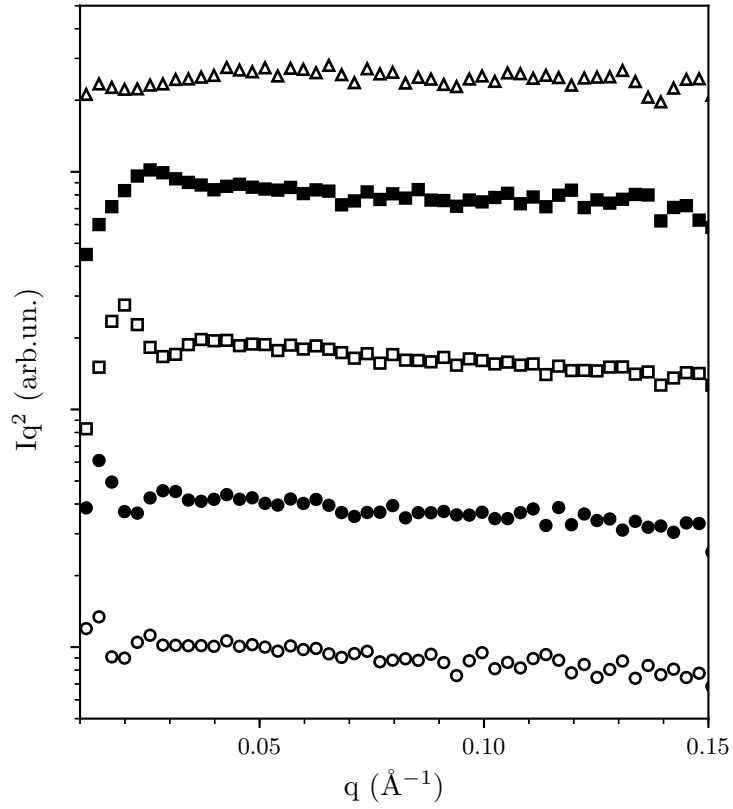
Steric repulsive interactions, from the configurational entropy associated to undulations of the GO sheets, and electrostatic repulsion have already been evidenced in the literature. In particular, in order to evaluate the importance of electrostatic interactions and monitor their relative weight in the balance, an easy and common method is adding salt to the samples, changing the ionic strength in the system.

The salt used for our experiments is NaCl and the samples are prepared diluting the ultracentrifuged dispersion in a saline solution with different concentrations, at the same final GO mass fraction. The nominal salt concentrations  $c_s$  range from  $10^{-5}$  M to  $\approx 10^{-1}$  M, covering a wide range of ionic strength.

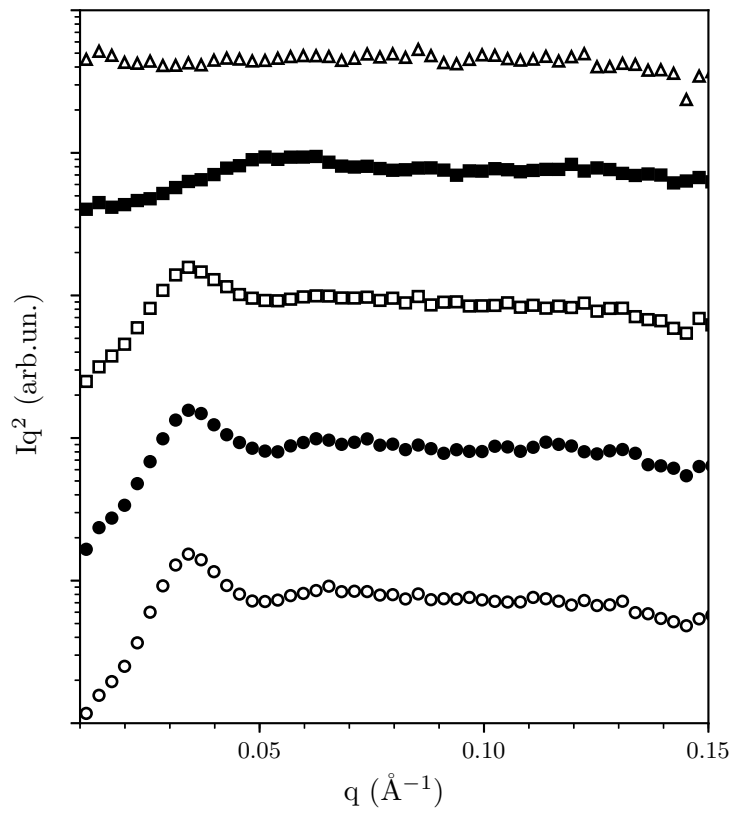
Two series of samples, with final mass fractions of  $f_m = 0.014$  and  $f_m = 0.043$  each, were prepared with different NaCl solutions in the whole domain of available concentrations and, after homogenisation, were analysed by SAXS. The results of the experiments for a few samples are presented in Figure 3.16.

One can observe that, for both series of samples, the curves for systems less charged in salt have two peaks, which are related to the lamellar order in the sample. These results could be expected, as the system is not very different from the one investigated in the dilution curve observed with no salt. However, different observations are made for each one of the series when the ionic strength is increased.

For the less concentrated dispersions (Figure 3.16a), it is possible to observe that the



(a) GO mass fraction fixed to  $f_m = 0.014$ . Salt concentrations  $c_s = 1 \times 10^{-5}$  M ( $\circ$ ),  $1 \times 10^{-4}$  M ( $\bullet$ ),  $1 \times 10^{-3}$  M ( $\square$ ),  $1 \times 10^{-2}$  M ( $\blacksquare$ ),  $1 \times 10^{-1}$  M ( $\triangle$ ). Data shifted vertically by amounts allowing a better visualisation.



(b) GO mass fraction fixed to  $f_m = 0.043$ . Salt concentrations  $c_s = 1 \times 10^{-5}$  M ( $\circ$ ),  $5 \times 10^{-4}$  M ( $\bullet$ ),  $1 \times 10^{-2}$  M ( $\square$ ),  $4 \times 10^{-2}$  M ( $\blacksquare$ ),  $1 \times 10^{-1}$  M ( $\triangle$ ). Data shifted vertically by amounts allowing a better visualisation.

Figure 3.16 – SAXS spectra in the Kratky representation for GO aqueous dispersions with two constant mass fractions  $f_m$  differing in salt content  $c_s$ .

first order peak significantly moves towards higher values of  $q$  when salt is added to the system, indicating a decrease in the distance between the GO layers. In addition, we can notice a broadening in this peak, until it practically disappears for high salt concentrations.

Broadly equivalent results are obtained for the more concentrated series, as shown in Figure 3.16b, however, the first order peak does not change its position for low amounts of NaCl, indicating a constant lamellar periodicity. When the number of ions is increased, though, a characteristic concentration  $c_s^*$  is reached where the periodicity starts to decrease and, for even higher salt concentrations, the peak is not visible anymore.

The same effect is observed in Xu and Gao (2011b), a decreasing in the stacking period with the increasing in the amount of salt. Closely related systems had already been studied, giving similar results (Gabriel et al., 2001; Michot et al., 2006).

The GO dispersions in saline solution were observed in POM and the images of two of the samples are shown in Figure 3.17. The chosen salt concentrations for these samples delimit the transition before and after the disappearance of the first order peak of the lamellar phase.

It is possible to observe in the sample with more ions (Figure 3.17c) the presence of large aggregates that are not observed in the less charged sample (Figure 3.17a). This result shows that the formation of GO aggregates is directly related to the disappearance of the peak characteristic of the lamellar phase.

Therefore, we can determine the periodic distance of each one of the systems before the lost of the lamellar organisation as a function of the salt concentration. The obtained results are presented in Figure 3.18.

The obtained curves show that before reaching a critical salt concentration  $c_s^*$ , the lamellar organisation is stable and, for more charged samples,  $d$  starts to decrease until it reaches a minimum value where the layers start to aggregate, losing the lamellar structure.

These results put in evidence the importance of the repulsive electrostatic interactions for the stabilisation of the lamellar structure of GO sheets. The presence of salt screens these interactions and the ratio between the intensity of all the repulsive contributions and the attractive ones starts to decrease, making the GO layers to attract each other. The effect of this changing in the balance of the interactions is the decreasing in the distance between the GO sheets, up to the point where the aggregates are formed.

It is important to highlight that, when the lamellar period starts to decrease, part of the solvent present in between the GO sheets is expelled from the lamellar structure, forming a new phase composed of solvent in excess. In these conditions, a biphasic domain is obtained, with a lamellar stacking of GO sheets coexisting with solvent in excess.

One can also notice that  $c_s^*$  is directly dependent on the GO mass fraction, which means that the higher the GO mass fraction  $f_m$ , the higher the number of ions needed to reach the balance point in screening the electrostatic interactions.

The results presented in this chapter have been published in Rubim et al. (2018), where a deeper discussion concerning the stability of this system is presented. The full

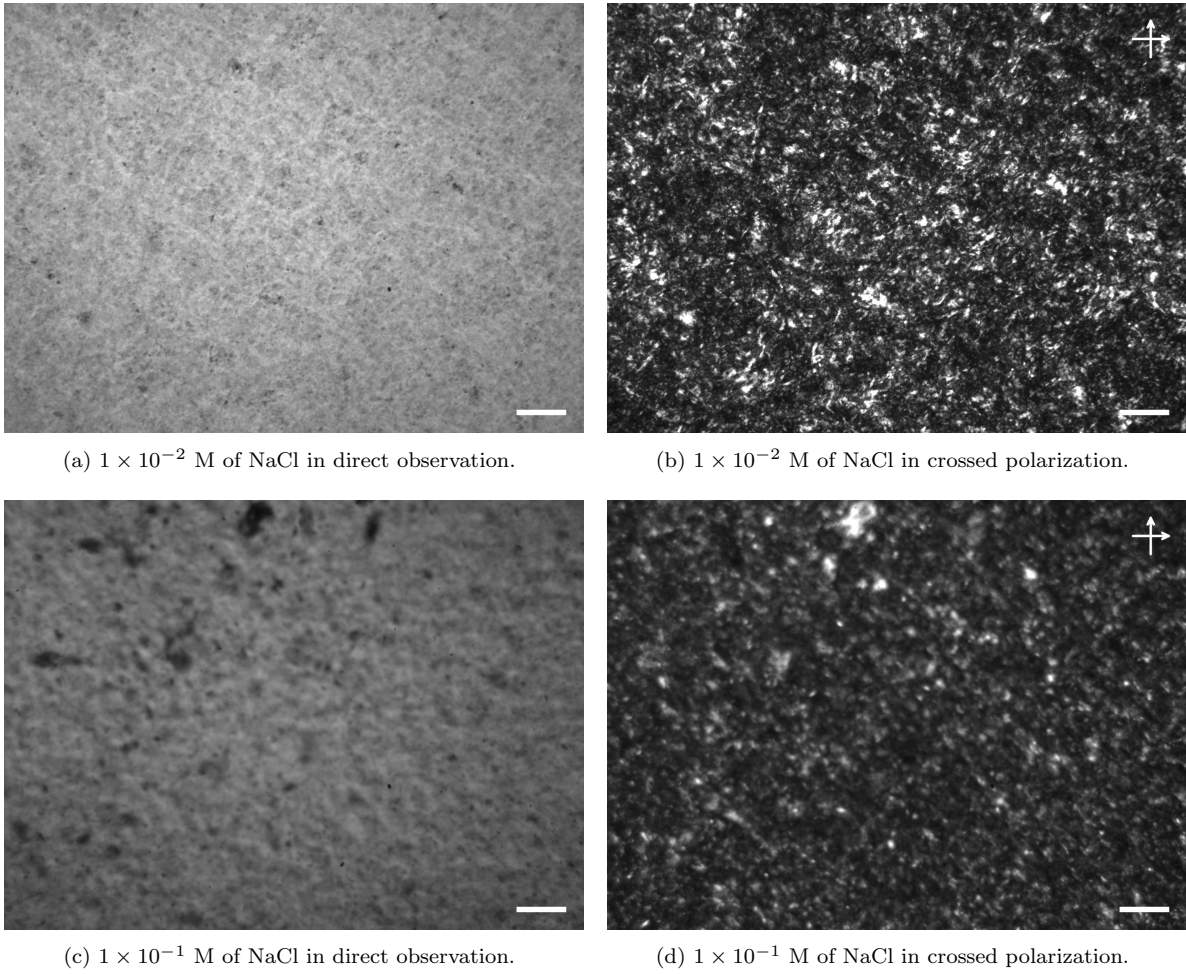


Figure 3.17 – POM images of the GO dispersions prepared at  $f_m = 0.043$  with different NaCl concentrations. The scale bars are equivalent to  $100 \mu\text{m}$ .

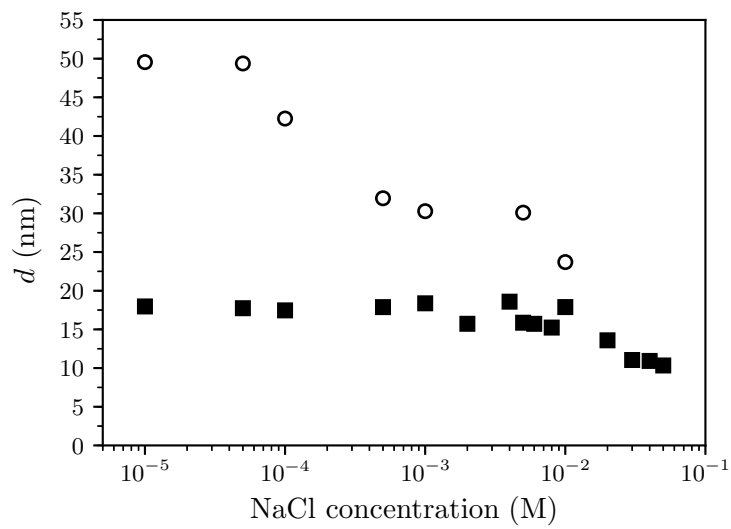


Figure 3.18 – Lamellar periodicity as a function of the NaCl concentration for GO mass fraction of:  $f_m = 0.014$  ( $\circ$ ),  $f_m = 0.043$  ( $\blacksquare$ ).

article is available in Appendix A.

After a qualitative characterisation of the structure of GO dispersion and the stability of the system, we can try to extract more quantitative information from the SAXS experiments, using adapted models to describe the experimental data.

# Chapter 4

## SAXS models for graphene oxide dispersions

### 4.1 Absolute scale normalisation

The curves obtained from scattering experiments, like SAXS, contain valuable information about the investigated system. Using adapted models to describe how the radiation will interact with the sample, it is possible to fit the experimental data and obtain quantitative parameters to describe the scattering units and their organisation.

However, to have access to specific information, molar mass for instance, about the particles, it is necessary to normalise the scattered curves to obtain the intensity in absolute scale. This normalisation is completely dependent on the equipment used and on the conditions at which the experiments are carried out. As mentioned in subsection 2.4.4, the experiments presented in this chapter were performed at the Institute of Physics of the University of São Paulo (Brazil).

Absolute calibration is very useful for interpreting the data, because it relates the intensity of the scattered radiation with the scattering cross section of the system, providing a curve that is independent on the experimental setup and conditions of the experiment. This normalisation of the scattered curves allows the comparison with the curves obtained in different ranges of  $q$  or even with curves obtained by other scattering techniques. Besides, as mentioned above it is possible to determine the molar mass of the scattering particles and to detect interactions between particles in diluted dispersions (Lindner and Zemb, 2002).

This normalisation can be performed using a standard sample with known differential scattering cross section. Therefore, two experiments are necessary for the calibration: the measurement of the scattering of the standard sample and the measurement of the scattering of the same empty sample holder in the same conditions. The information from both are necessary because the intensity of the sample holder has to be subtracted from the one obtained for the standard sample. In our case, we use as standard sample the water

at 20°C, whose theoretical scattering cross section per unit volume equals 0.01632 cm<sup>-1</sup> (Orthaber et al., 2000), and a capillary in quartz.

In addition, the intensities of the noise in the experimental setup, mostly due to the electronics in the machine, and the shadow in the detector, generated by the beam stopper, are also measured. The exactly same capillary is used for the calibration and for the experiments, assuring constant conditions of acquisition, like the sample path and thickness of the capillary walls.

With all the obtained information and the results of the analysed samples, the normalised experimental data can be obtained using the expression given by Equation 4.1, where  $I$ ,  $\Phi$ ,  $T$ ,  $t$  and  $d\Sigma/d\Omega$  are, respectively, the measured scattered intensity after integration, the intensity of the incident beam, the transmission of the sample, exposition time and the theoretical scattering cross section. The indexes  $t$ ,  $s$ ,  $b$ ,  $n$ ,  $sh$  and  $w$  indicate, respectively, the treated result, the sample, the background, the noise, the beam stopper shadow and the water.

$$I_t(q) = \left\{ \left[ \frac{I_s(q)}{\Phi_s T_s t_s} - \frac{I_b(q)}{\Phi_b T_b t_b} - \frac{I_n(q)}{t_n (\Phi_s T_s - \Phi_b T_b)} \right] \frac{1}{I_{sh}(q)} \right\} \frac{d\Sigma/d\Omega_w}{I(0)_w} \quad (4.1)$$

As an example of the correction procedure, one can observe in Figure 4.1 the curves of the intensity as a function of the scattering vector for a GO dispersion and water, which correspond to the scattering of the sample and the background, respectively, and the obtained final corrected curve. The intensity of the corrected curve is normalised in absolute scale, contrary to the other curves. The representation in arbitrary units is convenient for comparing the spectra. It is possible to notice that the treatment brings out the wanted information, as the peaks are clearer after the correction procedure.

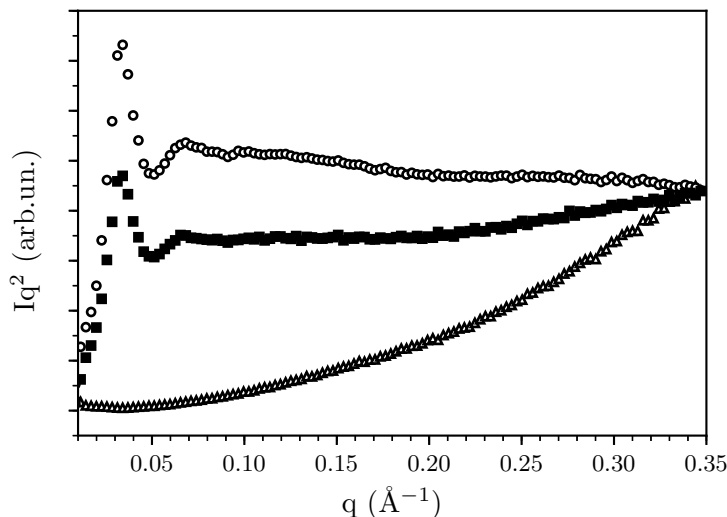


Figure 4.1 – Spectra obtained for the background ( $\Delta$ ), for the sample before the correction ( $\blacksquare$ ) and the result after the treatment ( $\circ$ ).

The data normalisation is performed using the SUPERSAXS package (Oliveira and

Pedersen, Unpublished). After this procedure, the data can be interpreted and, from the fittings using models that describe the analysed system, the parameters that characterise the spatial configuration of the units and their shape can be obtained. This theoretical description of the SAXS experiments will be discussed in the next section.

## 4.2 Principles of SAXS theory for disk-like objects

In many situations, the intensity of the scattered radiation by unoriented samples made of thin, but elongated plate-like objects (“flat disks”) can be considered as proportional to the product of two terms describing the investigated system: the form and structure factors. For this reason, the intensity  $I$  as a function of the scattering vector  $q$  can be expressed by Equation 4.2, where  $A$  is a normalising constant and  $c$  a background constant.  $P(q)$  and  $S(q)$  represent, respectively, the form and structure factors, which will be detailed below (Kratky and Porod, 1949).

$$I(q) = A \frac{2\pi}{q^2} P(q) S(q) + c \quad (4.2)$$

As mentioned in subsection 2.4.4, the interaction between the X-ray radiation and the matter depends on the contrast electron density of the investigated system. The scattering patterns that will be detected are related to the inhomogeneities of the electron density in the particles, if any, and also the difference between the particle itself and the surrounding medium. The sum of the amplitude of all the scattered waves that reach the detector in a given position is dependent on the shape of the system that has been irradiated. The square of this sum is called from factor  $P(q)$  of the particle.

For this reason, as the name may indicate, the form factor contains information about the form of the scattered system. The factor sense comes from the fact that, as already mentioned, it has to be scaled with a constant in order to match the experimental intensity units. Using the inverse of a Fourier transform, and disregarding ambiguities related to the so-called “phase problem” it is possible to obtain the electron contrast density profile of a particle from its form factor.

The ideal situation to obtain the form factor of a sample is when the particles are identical in shape and size and they do not interact, which is the case for diluted dispersions. In these conditions, the obtained scattering pattern is proportional to the form factor of a single particle multiplied by the number of illuminated units. However, if the investigated sample presents any kind of polydispersity, the obtained form factor will be proportional to the average form factor of all the illuminated particles.

Therefore, it is possible to obtain the form factor of a GO layer in order to have access to the parameters that will describe their shape and electron distribution. The simplest model that can be adopted to the GO sheets, which can be seen as flat particles, ideally a mono-atomic sheet of carbon atoms, is to consider the layers as infinite planes with zero

thickness, resulting in a form factor that is not dependent in  $q$  and equals to 1.

Although this approximation is reasonable for our system in the investigated range of scattering vector, it does not provide information about the shape of the GO layers. For this reason, another model can be proposed, which consists on considering the GO sheets as layers with a constant thickness and homogeneous electron density. The form factor of this kind of particles can be expressed by Equation 4.3, where  $\Delta\rho$  is the constant electron density of the layers relative to the background electron density and  $\delta$  is its thickness (Kratky and Porod, 1949).

$$P(q) = \frac{4}{q^2} \Delta\rho^2 \sin^2 \left( q \frac{\delta}{2} \right) \quad (4.3)$$

Nevertheless, a more complex model for the distribution of the electron density of the GO layer can be proposed, trying to better represent the observed results. Considering that the electron density is not constant along the perpendicular axis to the plane of the sheets, due to the presence of oxygen groups in the surface of the GO layer, the electron density profile can be described by the presence of steps, which will result in the form factor given by Equation 4.4, where the indexes  $i$  and  $o$  represent the inner and outer parts of the layer, respectively, and  $\Delta\rho$  and  $\delta$  are, respectively, the electron density of the layer relative to the background electron density and half of its length (Nallet et al., 1993).

$$P(q) = \frac{4}{q^2} \{ \Delta\rho_o [\sin(q(\delta_o + \delta_i)) - \sin(q\delta_i)] + \Delta\rho_i \sin(q\delta_i) \}^2 \quad (4.4)$$

A schematic representation of the electron density profile of the GO layers obtained from the form factors of both models is shown in Figure 4.2.

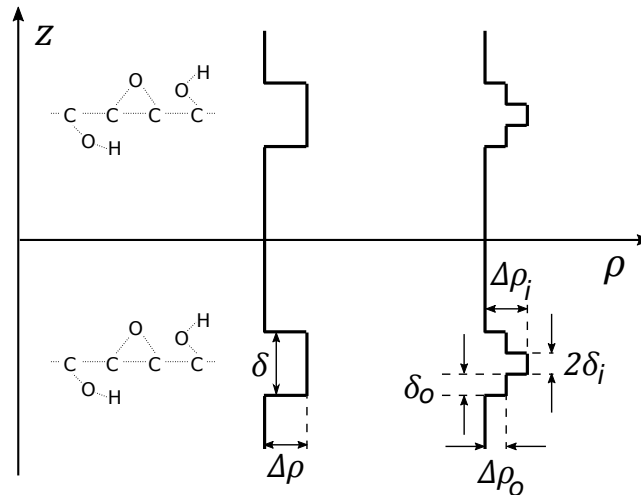


Figure 4.2 – Schematic electron density profile  $\rho$  along the perpendicular direction to the GO layer  $z$  for: the constant model (Equation 4.3) in the left and the model in steps (Equation 4.4) in the right.

Even though the form factor is obtained for diluted samples, when the concentration of units in the dispersion starts to increase, the distances between neighbour particles become

comparable to the particle size: The overlap concentration is reached. In the case of very anisometric particles—as suggested by Onsager’s analysis of the isotropic-to-nematic transition for elongated rods, for instance—the overlap concentration remains low. Though not yet “dense”, but “semi-dilute” as commonly expressed, the system shares features with truly dense systems: The interference pattern obtained will contain information not only about the shape of the particles, but will also comprehend information concerning the organisation of the neighbouring units. This additional information expressing the structure of the particles in the ensemble represents, as the name may indicate, the structure factor  $S(q)$  of the system.

The structure factor contains the information of the positions of the particles with respect to each other. In the case of diluted samples, the structure factor can be considered to be equal to 1, however, for a smectic organisation (see section 2.2), which is the structure obtained for the dispersions of GO in a large part of its extended semi-dilute regime, it can be expressed by model Equation 4.5 and Equation 4.6, where  $N$  is the number of correlated layers,  $d$  is the distance of repetition of the structure,  $\gamma$  is the value of Euler’s number and  $\eta$  is known as Caillé parameter (Nallet et al., 1993).

$$S(q) = 1 + 2 \sum_{n=1}^{N-1} \frac{\left(1 - \frac{n}{N}\right) \cos \left[ \frac{qdn}{1+2\Delta q^2 d^2 \alpha(n)} \right] \exp \left\{ -\frac{2q^2 d^2 \alpha(n) + \Delta q^2 d^2 n^2}{2[1+2\Delta q^2 d^2 \alpha(n)]} \right\}}{\sqrt{1 + 2\Delta q^2 d^2 \alpha(n)}} \quad (4.5)$$

$$\alpha(n) = \frac{\eta}{4\pi^2} [\ln(\pi n) + \gamma] \quad (4.6)$$

The Caillé parameter gives information about the flexibility and interactions of the layers, as it is dependent on the splay modulus  $K$  and the compression modulus  $B$  of the smectic structure, and can be expressed by Equation 4.7, where  $q_0$  is the position of the Bragg’s first order peak,  $k_B$  the Boltzmann constant and  $T$  is the temperature.

$$\eta = \frac{q_0^2 k_B T}{8\pi \sqrt{KB}} \quad (4.7)$$

Consequently, as mentioned above, the scattering curves of GO dispersions can describe, simultaneously, the shape of the GO layers and their organisation in the space. The proposed models can be compared and, from the fitting of the experimental data, it is possible to obtain the parameters to describe the system.

### 4.3 Fittings of SAXS curves

Following the procedure described in section 3.2, the GO dispersion is concentrated and then redispersed in different proportions, resulting in samples with different final concentrations. In this step of the study, the more concentrated sample contains around 10% of GO in mass and the more diluted is equivalent to the commercial concentration, *i.e.* a concentration of 0.04%.

For a sample with a GO mass fraction of 4%, SAXS experiments were carried out and the results are presented in Figure 4.3 . The image of the obtained diffractogram is shown in Figure 4.3a, where the first order Bragg's peak can be observed at  $q_0 = 0.029 \text{ \AA}^{-1}$ .

As already discussed in section 3.3, it is possible to observe the presence of a certain degree of orientation in the image. To quantify this level of orientation of the sample, an azimuthal integration around the position of the Bragg's first order peak was performed. The integration was executed for  $2\theta$  varying between  $0.3^\circ$  and  $0.5^\circ$ , which corresponds to  $q$  ranging from  $\approx 0.021 \text{ \AA}^{-1}$  to  $\approx 0.036 \text{ \AA}^{-1}$ . Therefore, the interval of integration is given by  $0.028 \pm 0.007 \text{ \AA}^{-1}$ , and the obtained curve of the intensity as a function of the azimuthal angle  $\psi$  is presented in Figure 4.3b.

The curve can be described by Equation 4.8, where  $A$  is the amplitude,  $\psi$  is the azimuthal angle,  $\psi_0$  is the phase and  $\sigma$  is the standard deviation.

$$I(\psi) = A \exp \left[ -\frac{\cos^2(\psi + \psi_0)}{2\sigma^2} \right] + c \quad (4.8)$$

A parameter describing the azimuthal contrast, which is related to the ordering of the sample, can be defined by Equation 4.9.

$$\text{azimuthal contrast} = \frac{I_{max} - I_{min}}{\frac{I_{max} + I_{min}}{2}} \quad (4.9)$$

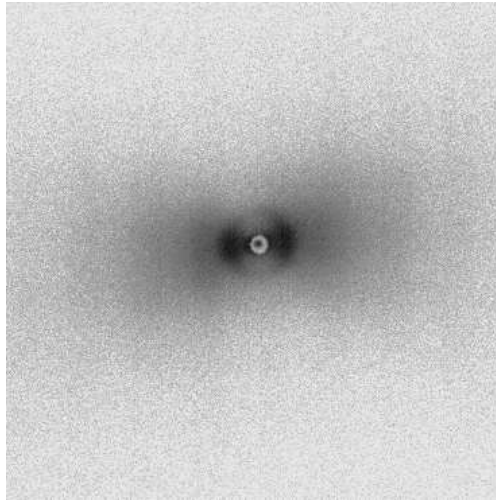
The fitting of the curve gives an azimuthal contrast of 7.4 with a full width at half maximum in the order of  $0.36\pi$  rad, showing that the sample is slightly oriented, but it still can be considered as isotropically distributed for the fittings. The comparison between the integration in the whole azimuthal range and around each maximum of the peaks, with an angular width  $\Delta\psi$  of  $\pi/9$  rad, is presented in Figure 4.3c.

One can observe that there is no significant difference between the obtained curves. The position of the peaks is constant whether for a small sector or not, besides, the averaged curve presents a smoother shape. For these reasons, the integrations for all the investigated samples were carried out in the complete azimuthal domain.

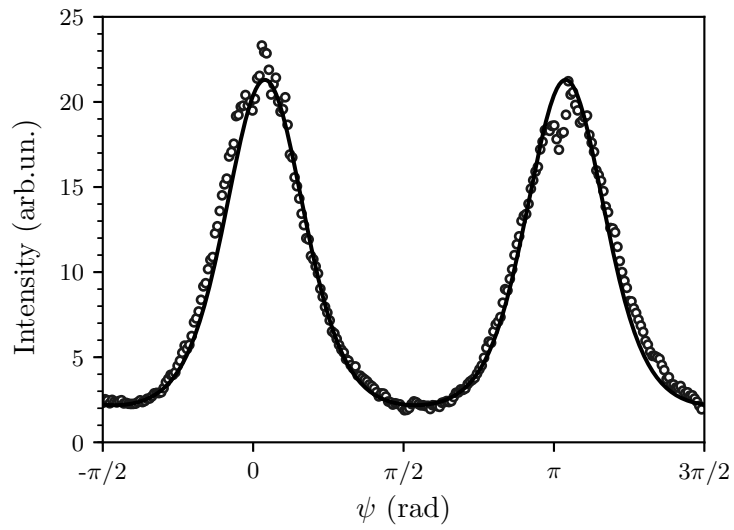
After the integration, the curves are corrected using the absolute scale procedure and some of the curves are presented in Figure 4.4. It is possible to observe an increasing in the intensity with the increasing in the concentration, which is expected because of the higher number of illuminated particles in the solution.

However, among the presented samples, it is possible to observe a superposition of the curves obtained for the more concentrated GO dispersions, showing that the correction procedure is not adapted in this condition. This effect can be related to multiple scattering, where the scattered radiation interacts with more than one particle in the dispersion before reaching the detector.

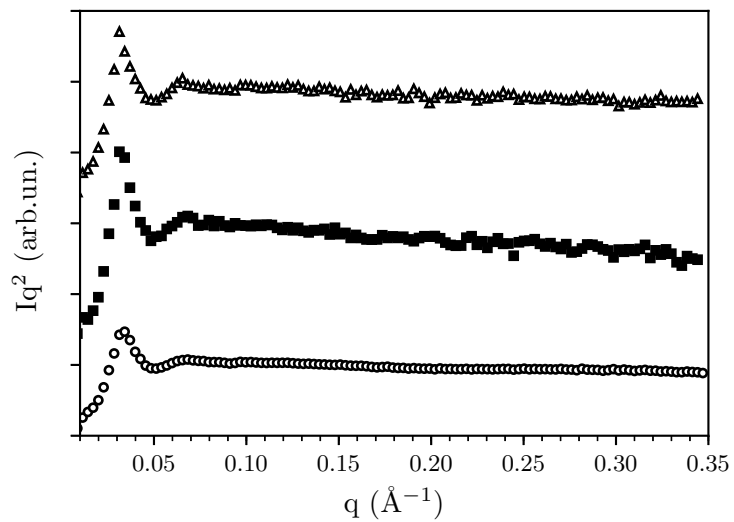
Nevertheless, the curves contain information about the investigated system even if the absolute calibration is not correctly performed. For the most concentrated samples, one



(a) Diffractogram of the sample. Intensity is in log scale.



(b) Intensity as a function of the azimuthal angle around the first order Bragg peak, *i.e.*  $q = 0.028 \pm 0.007 \text{ \AA}^{-1}$ .



(c) Integration in the whole radial range for sectors with  $\Delta\psi = \pi/9$  rad around  $\psi = 0$  rad (■) and around  $\psi = \pi$  rad (Δ), and integration in the complete azimuthal range (○).

Figure 4.3 – SAXS results of a GO dispersion with  $f_m = 0.04$ .

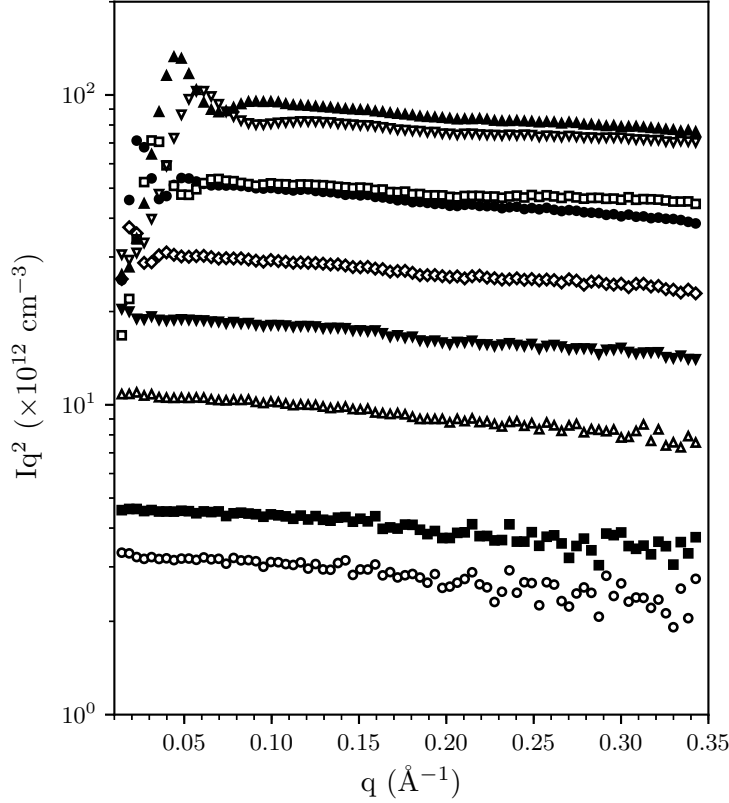


Figure 4.4 – SAXS spectra in absolute scale for GO dispersions with:  $f_m = 0.004$  ( $\circ$ ),  $f_m = 0.005$  ( $\blacksquare$ ),  $f_m = 0.010$  ( $\triangle$ ),  $f_m = 0.015$  ( $\blacktriangledown$ ),  $f_m = 0.020$  ( $\diamond$ ),  $f_m = 0.030$  ( $\bullet$ ),  $f_m = 0.040$  ( $\square$ ),  $f_m = 0.050$  ( $\blacktriangle$ ) and  $f_m = 0.056$  ( $\triangledown$ ).

can see the presence of Bragg’s peaks related to the smectic ordering, which is not visible for the more diluted dispersions. This observation does not mean that the organisation is not a lamellar, but that the window of  $q$  may not be large enough to allow its visualisation.

Once the curves are corrected, the fitting procedure can take place. The minimisation of the difference between the experimental and theoretical curves is executed using the least squares method (Jones et al., 2001), and Figure 4.5 shows the difference between the fittings using the three models for the form factor presented in section 4.2 for a sample containing 5.6% of GO in mass.

It is possible to observe that for small  $q$  there is no significant difference between the fittings. This effect is expected, as this part of the curve is dominated by the structure factor, which is the same in the three cases. Therefore, no difference is expected between the parameters describing the organisation of the lamellar phases for the different fittings.

However, a difference is observed between the theoretical curves in the higher domain of  $q$  for a same experimental data. Although none of the three models completely reproduces the experimental curve, the two-step model satisfactorily describe the curve, followed by the model with constant electron density, with, as expected with a lesser number of fitting parameters, more discrepancies at larger scattering angles.

The fittings were carried out for all the prepared samples and the obtained parameters

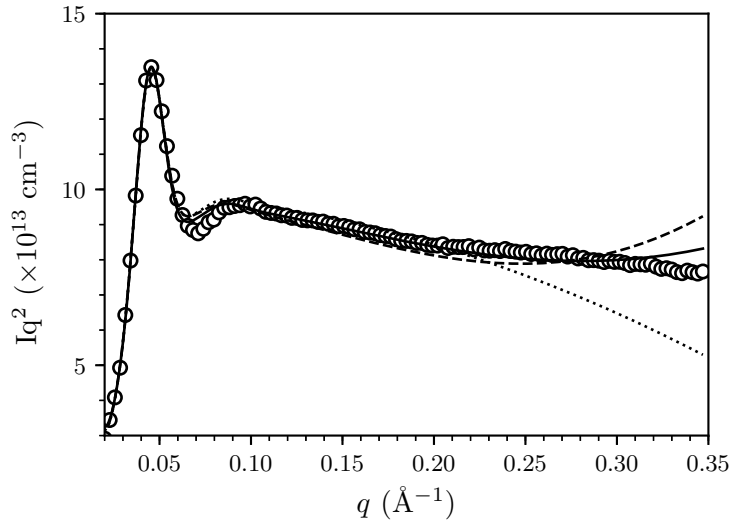


Figure 4.5 – SAXS spectrum of a GO dispersions with  $f_m = 0.056$  and the respective fittings using model: thickness equals zero (dotted line), constant contrast density (dashed line) and contrast density in steps (continuous line).

are presented in Figure 4.6. For the concentrated samples, it is possible to obtain information about the shape and organisation of the layers, through the access of the form and structure factors. However, only the form factor is accessible for the more diluted dispersions, concentrations at which the Bragg’s peaks are not visible.

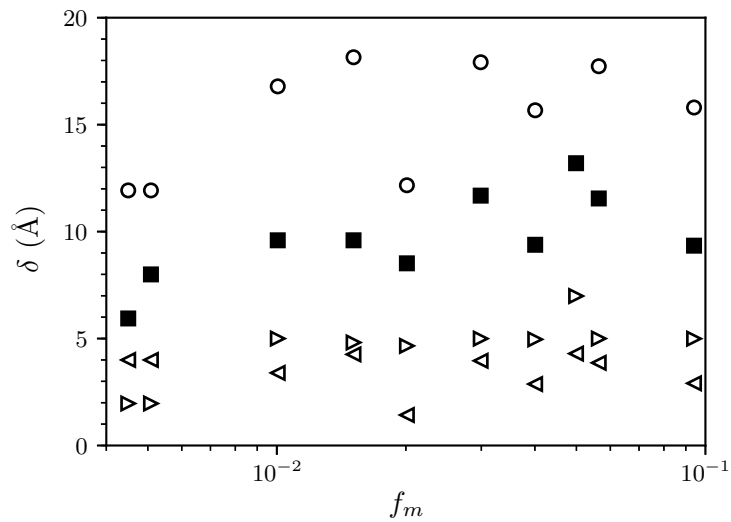
In Figure 4.6a, it is possible to see the thickness of the layers obtained with both models. One can observe that, for a given sample, the thickness revealed by the model in steps is higher than the one retrieved with the constant model.

In addition, despite the fluctuations, these values can be considered to be constant and equal to  $\approx 10 \text{ \AA}$ , for the model with constant electron density, and  $\approx 15 \text{ \AA}$ , for the model in steps. As the thickness of the GO layers can be considered to be constant, a variation on the lamellar periodicity can be considered to be the same as a variation on the distance between the layers.

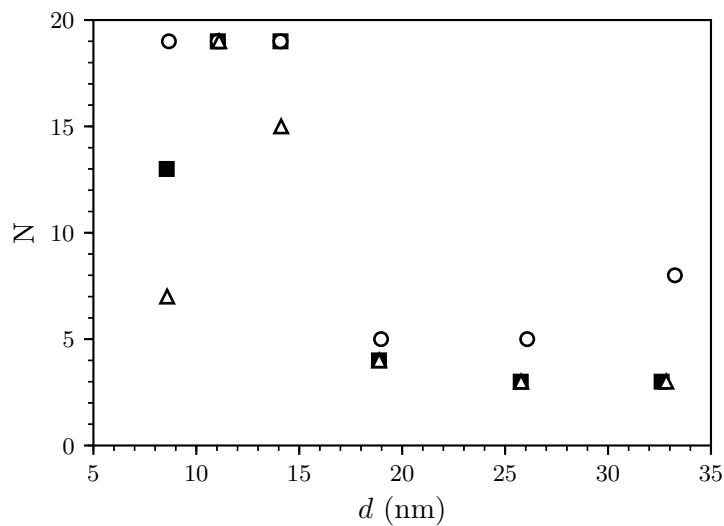
Moreover, for the more detailed thickness described by the model in steps, the total inner length of the sheet, given by  $2\delta_i$ , is in the order of  $6 \text{ \AA}$ . This value is not distant from the thickness of a graphene layer (see section 2.1) and from the value obtained for the geometrical thickness of a GO layers by the swelling law (see section 3.3).

These findings reveal that the inner length obtained with the profile of the electron density in steps can be interpreted as the carbon layer of the GO, while the outer part describes the solvated oxygen groups. Correspondingly, the model with a constant electron density considers an average value between the inner and outer parts of the layer, providing a smaller thickness.

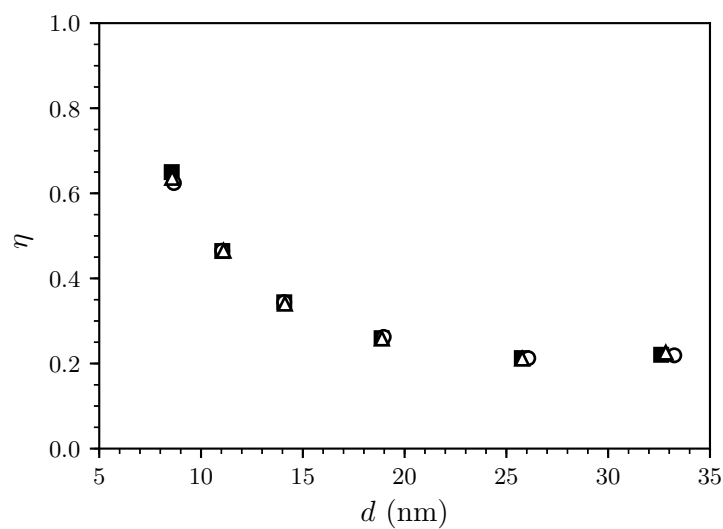
One can observe in the dilution line of the GO aqueous dispersions (Figure 3.14), that for  $d \approx 15 \text{ \AA}$ , an anomaly in the curve is observed. This lamellar periodicity is compatible to the thickness of the GO layer obtained using the model in steps, which indicates that,



(a) Thickness of the GO layers as a function of the GO mass fraction. The thickness described by the model in steps is obtained as twice the sum of the inner ( $\triangleleft$ ) and outer ( $\triangle$ ) lengths.



(b) Number of correlated layers as a function of the lamellar periodicity.



(c) Caillé parameter as a function of the lamellar periodicity.

Figure 4.6 – Parameters obtained from the fittings of the curves of GO dispersions using model: thickness equals zero ( $\triangle$ ), constant contrast density ( $\blacksquare$ ) and contrast density in steps ( $\circ$ ).

for smaller stacking periods, the oxygen groups of neighbouring GO sheets are overlapped.

This configuration may favour hydrogen bonds between these groups, which get weaker when water is added to the system. The water molecules will interact more strongly with the oxygen groups in the surface of the GO than the groups of neighbouring layers, and these molecules will occupy the space swelling the phase. When there is enough water to fill the surface of the GO layers, the oxygen groups are no longer overlapped, and the periodicity reaches the value of the thickness of the GO sheet. From this point, the hydrogen bonds between the oxygen groups of adjacent sheets are broken and they get apart from each other, losing their contact. This phenomenon is schematically represented in Figure 4.7. The nature of the interactions between the sheets is different depending on the configuration of the structure, which may explain the anomalous behaviour of the GO swelling law in the confined regime.

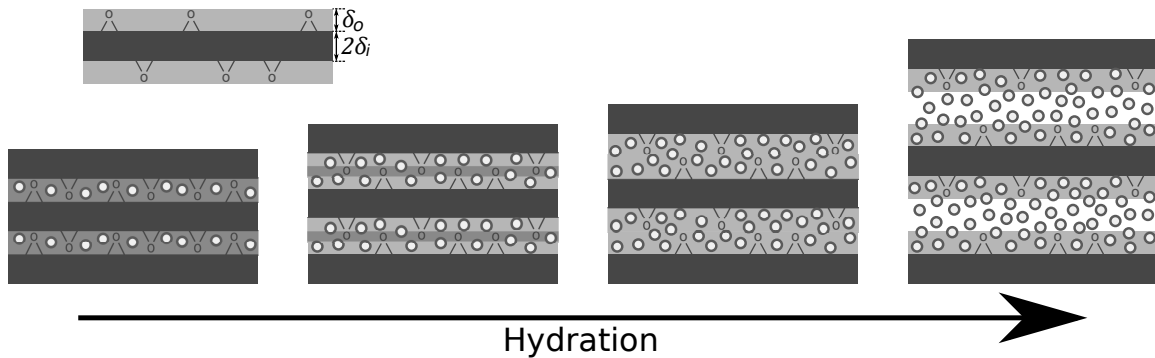


Figure 4.7 – Schematic representation of the swelling of GO sheets lamellar structure in water. The darker layer in the scheme represents the inner part of the GO sheet and the clearer ones represent its outer part, which corresponds to the oxygen groups. The water molecules are represented by circles and the amount of solvent increases from the left to the right.

Concerning the number of correlated layers, whose obtained results are presented in Figure 4.6b, it is possible to observe that the values are dependent on the model used, specially for the model in steps. Nevertheless, a global behaviour can be observed.

This parameter represents the number of layers that are strongly bounded forming the lamellar structure. One can see that, for the more concentrated samples, the number of bounded layers is higher and, when the dispersion is diluted, this number decreases, showing that the higher the concentration of the dispersion, the higher the interaction between the layers.

Figure 4.6c shows the evolution of the Caillé parameter as a function of the lamellar periodicity. We can notice that this quantity decreases as the layers get apart from each other. As this parameter is dependent on both  $K$  and  $B$ , it is difficult to interpret its variation and make a direct relation with the flexibility and/or the interactions of the structure.

Considering that  $K = \kappa/d$ , where  $\kappa$  is the bending rigidity of the GO sheets, whose value can be considered to be constant and equals to  $k_B T$ , as proposed in Poulin et al. (2016), we can expect the behaviour of  $\eta$  to be readily related to the dilution behaviour

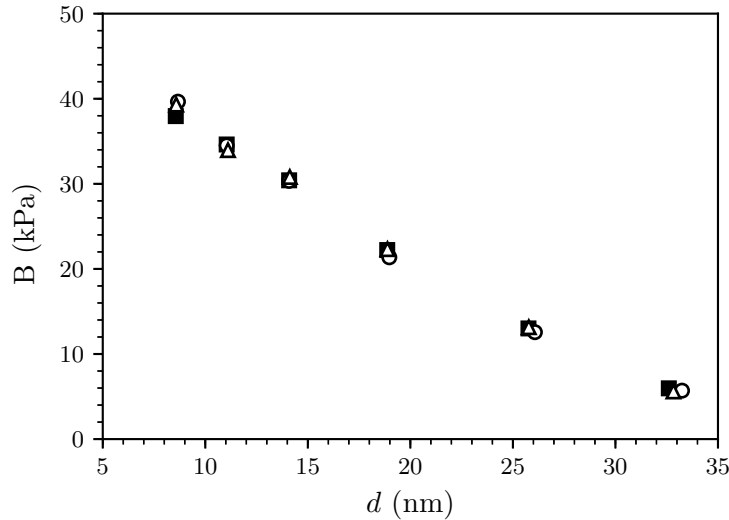


Figure 4.8 – Compression modulus as a function of the lamellar periodicity obtained from the fittings of GO dispersions using model: thickness equals zero ( $\Delta$ ), constant contrast density ( $\blacksquare$ ) and contrast density in steps ( $\circ$ ).

of the compression modulus of the smectic phase.

From Equation 4.7, it is possible to obtain the expression to calculate the compression modulus of the smectic phase, which is given by Equation 4.10.

$$B = \frac{\pi^2 k_B^2 T^2}{4\kappa\eta^2 d^3} \quad (4.10)$$

The compression modulus can be interpreted as the pressure needed to be applied to the system for the layers to be locally displaced from their position of equilibrium. This means that the higher the interaction between the layers, the higher the compression modulus. This parameter can be calculated for each one of the prepared samples and the obtained results are presented in Figure 4.8.

One can observe that, as the lamellar periodicity increases, the compression modulus decreases. This observation is consistent with the presence of dominant repulsive interactions between the layers. Once the layers get closer to each other, the higher becomes the repulsive contribution and the higher will be the force necessary to be applied for the layers to approach each other.

All the obtained results contributed to better characterise and understand the mechanisms of stability of GO layers in aqueous dispersions. We can now use this knowledge to investigate a new system, whose study will be presented in next chapter, consisting specifically on complexes of graphene oxide and surfactant dispersed in water.

# Chapter 5

## Complexes of Graphene Oxide and Surfactant

### 5.1 Self-assembly of surfactant in water

Following the study of the dispersions of graphene oxide in water, we started investigating the system composed of GO sheets and surfactant in water, which will be called as ternary system. As previously described in section 1.2, the objective of this thesis is to explore and characterise the complexes obtained with the coupling of the two materials.

Analogously to the study of the binary GO-water system, prior to the investigation of the ternary complexes, it is of great interest to introduce the binary surfactant-water system. The surfactant used in this work is known as simulsol (see Figure 2.7). The phase diagram of lipid systems associated with ethoxylated fatty acids, such as the simulsol, has been extensively investigated in our group and a partner team (da Silva, 2011; Gerbelli et al., 2013; Rubim, 2014; Bougis, 2016; Rubim et al., 2016).

For the binary simulsol and water system, the samples are prepared by mixing the two components in different proportions and, to accelerate the homogenisation process, a few cycles of soft centrifugation, intercalating between the upright and upside down orientations, are performed every two or three days. The samples are stored at 4°C and, after three weeks, they are considered to be homogeneous and can be analysed.

In previous works, we showed that for mild concentrated samples of simulsol in water, a lamellar structure is formed. With the addition of solvent, the structure can be diluted, following closely the ideal swelling law expressed by Equation 2.3, and no dilution limit was observed in the investigated range of concentration. Nevertheless, when the simulsol concentration is increased, a phase transition is observed (Bougis et al., 2015).

In Figure 5.1, a few of the obtained spectra for a series of aqueous simulsol dispersions with different surfactant volume fractions are presented. It is possible to observe that, for  $\varphi_{\text{surfactant}}$  between 0.70 and 0.75, the shape of the x-ray scattering curves changes considerably, revealing the phase transition. The (rather sharp) Bragg peak, observed

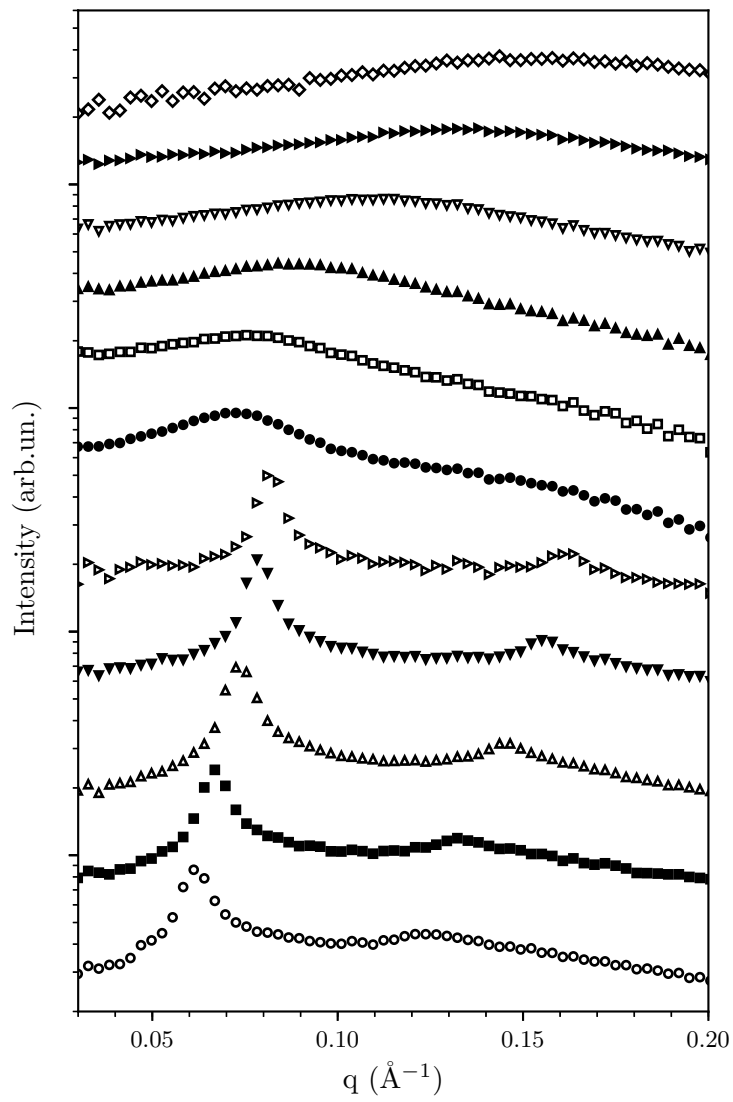


Figure 5.1 – SAXS spectra of surfactant in water with volume fraction of: 0.50 ( $\circ$ ), 0.55 ( $\blacksquare$ ), 0.60 ( $\Delta$ ), 0.65 ( $\blacktriangledown$ ), 0.70 ( $\triangleright$ ), 0.75 ( $\bullet$ ), 0.80 ( $\square$ ), 0.85 ( $\blacktriangle$ ), 0.90 ( $\nabla$ ), 0.95 ( $\blacktriangleright$ ) and 1.00 ( $\diamond$ ). Convenient scaling factors have been used for a better readability of the figure

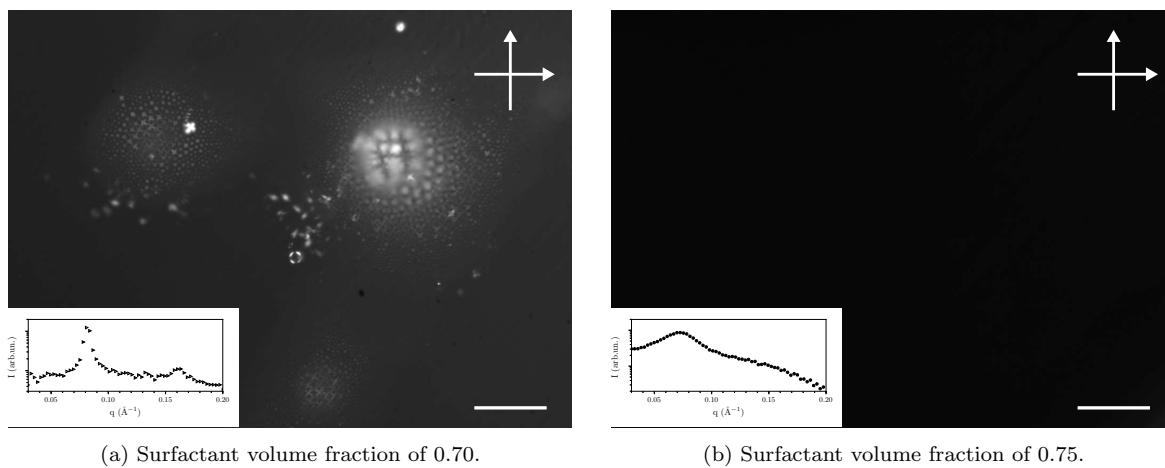


Figure 5.2 – POM images with crossed polarizer and analyser of surfactant aqueous dispersions before and after the phase transition. The scale bars are equivalent to 100  $\mu\text{m}$ . Inset: respective SAXS spectrum.

for diluted samples, is indeed replaced by a much broader hump when the concentration increases, which means that a structural reorganisation took place. A variation in the position of the hump is observed when the concentration is changed.

The two samples on both sides of the transition boundary were observed under POM. Microslides with a constant optical path of 0.2 mm were prepared and the obtained images, with the respective SAXS spectra, are presented in Figure 5.2.

One can observe in Figure 5.2a the presence of weak birefringence, which is related to a lamellar organisation, as it is revealed in SAXS measurements. The texture that is observed in the image can be associated to defects in the lamellar structure, where the layers are oriented in the plane of the image.

However, despite the presence of a certain level of organisation in the more concentrated system, which is evidenced by the hump that is detected in the SAXS curve, no birefringence is observed in POM, as one can see in Figure 5.2b. Up to now, this new phase has not been characterised in depth and its exact structure remains unknown.

For each one of the observed lamellar structures, occurring for the diluted systems, the periodicity  $d$  can be determined using Equation 2.8. After the phase transition, a characteristic distance in the new phase can be calculated using  $2\pi/q^*$ , where  $q^*$  is the position of the hump. The obtained results are presented in Figure 5.3.

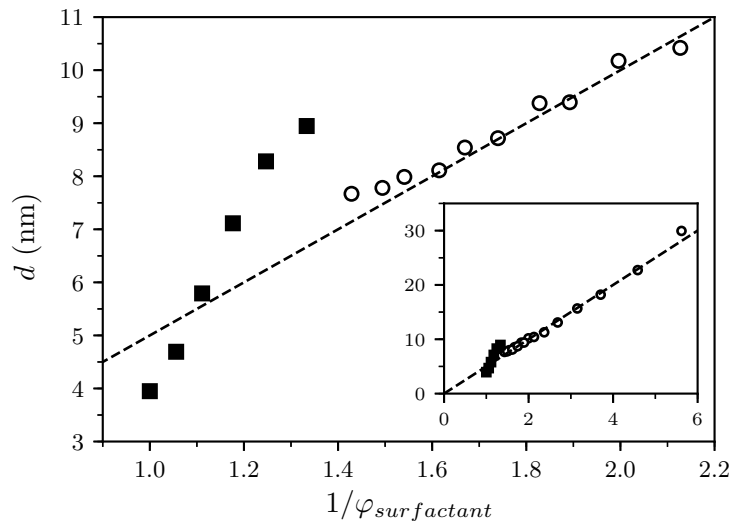


Figure 5.3 – Periodicity as a function of the inverse volume fraction for surfactant dispersions in a lamellar (○) and unknown (■) organisations. Inset: *idem* for the whole investigated dilution range. The dashed line corresponds to the swelling law expressed by Equation 2.3, with  $\delta = 5.0$  nm.

As expected, it is observed that the period of the lamellar stack decreases when water is removed from the structure, following the ideal swelling law. Nevertheless, near the phase transition, it is possible to see a deviation from the dilution curve, where the periodicity is slightly higher than the expected value, which can characterise a region of pretransition. The lower limit is observed when the lamellar periodicity reaches 7.7 nm, the smallest accessible period for stacked bilayers of simulsol in water.

Following the tendency, the characteristic distance of the new phase, just after the transition, is higher than the lower limit lamellar periodicity. Again, the characteristic distance decreases when water is removed from the system, with a dehydration rate much higher than the one observed for the lamellar phases, except around the phase transition and the completely dried system, where the dehydration rate decreases.

Furthermore, in order to reproduce the acid medium of the aqueous GO dispersion, the simulsol dispersions were duplicated using an aqueous solution of hydrochloric acid (HCl) at a pH of 2.5 instead of pure water. The x-ray experiments revealed no difference between both media, indicating that the structure formed by the simulsol molecules is not sensitive to variations in the pH, an important property for the progression of the study.

With the information obtained for the aqueous simulsol dispersions, it is possible to investigate the complexes formed by graphene oxide layers and surfactant. The procedures of preparation and characterisation of the complexes will be discussed in the next sections.

## 5.2 Preparation of GO-surfactant complexes

In order to prepare the GO-simulsol complexes, the surfactant molecules are added to the ultracentrifuged aqueous GO dispersion (see section 3.2) until the sample reaches the wanted proportion between simulsol and GO. This proportion can be defined as the ratio  $\varrho$  between the volume fractions of surfactant and GO, which can be described by Equation 5.1.

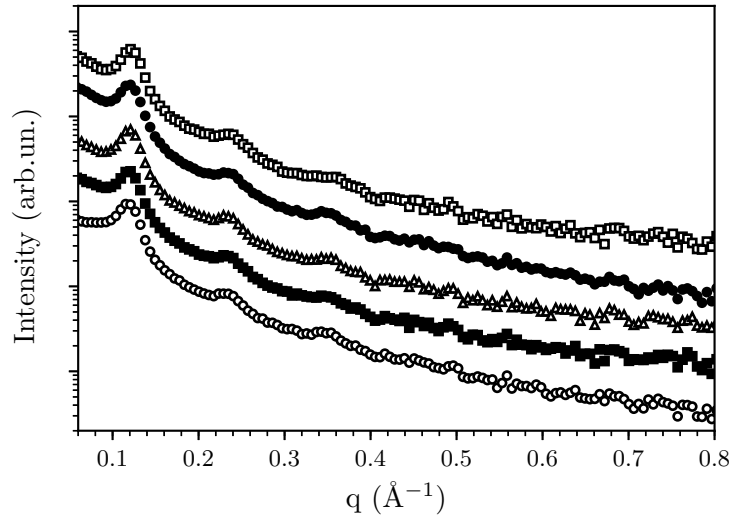
$$\varrho = \frac{\varphi_{\text{surfactant}}}{\varphi_{\text{GO}}} \quad (5.1)$$

To accelerate the homogenisation process, the same procedure used for the binary system surfactant-water is employed. Fixing the proportion between GO and simulsol, it is possible to vary the hydration of the sample, in which case water is added to the sample. In Figure 5.4, Figure 5.5 and Figure 5.6, the X-ray scattering results of three series of samples with constant  $\varrho$  are presented, after three weeks of stabilisation.

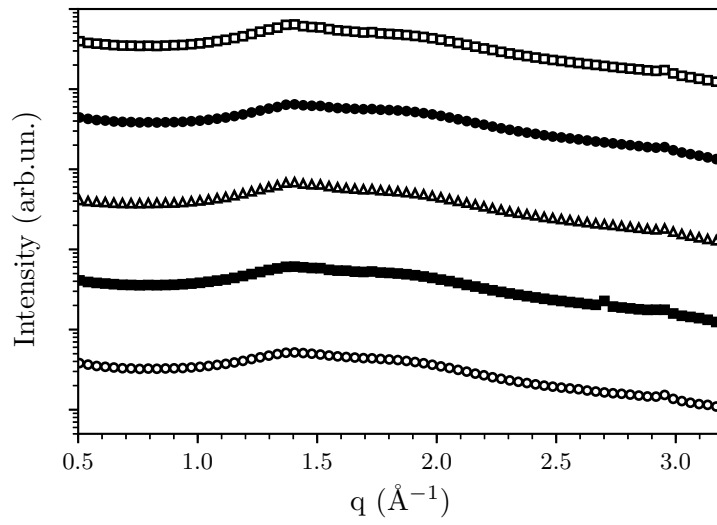
One can observe in the series with highest surfactant proportion (Figure 5.4a), the presence of Bragg's peaks characteristic of a lamellar phase. The peaks are visible up to the third order, with  $q_0 \approx 0.12 \text{ \AA}^{-1}$ . It is also possible to notice that, even if the amount of water is increased, the position of the peaks does not change, indicating that the stacked structure cannot be swelled.

The experiments carried out in a wider window of  $q$ , which is presented in Figure 5.4b, show the presence of two humps, one around  $1.4 \text{ \AA}^{-1}$  and the other around  $1.9 \text{ \AA}^{-1}$ , which are related to the mean distance between the simulsol and water molecules, respectively. The peak related to the distance between the carbon atoms in the plane of the GO layer, *i.e.*  $q = 2.96 \text{ \AA}^{-1}$ , is also visible.

These results show that, as expected, when water is added to the system, the hump

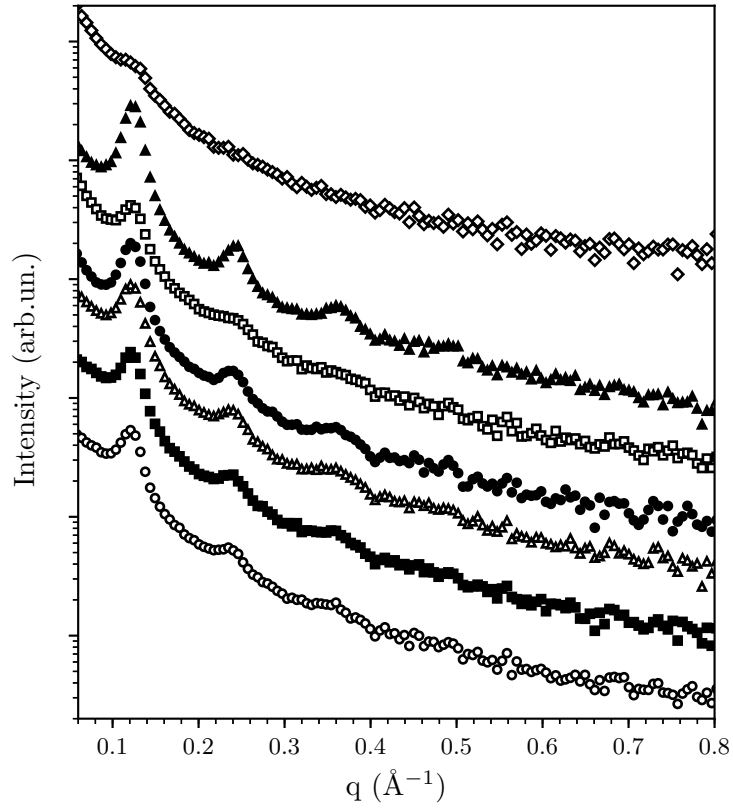


(a) SAXS spectra for water mass fraction of: 0.02 ( $\circ$ ), 0.15 ( $\blacksquare$ ), 0.27 ( $\triangle$ ), 0.38 ( $\bullet$ ) and 0.49 ( $\square$ ).

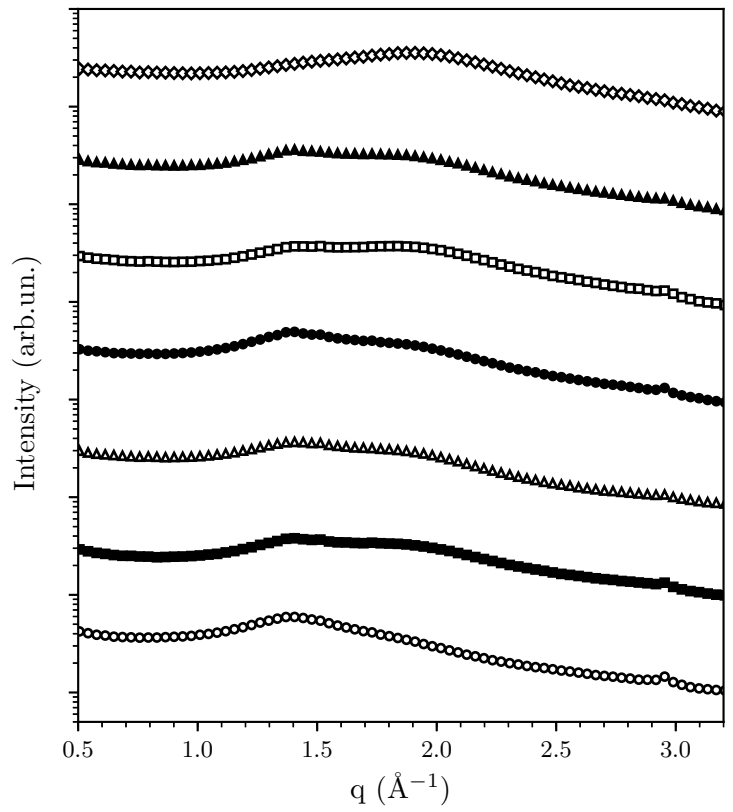


(b) WAXS spectra for water mass fraction of: 0.02 ( $\circ$ ), 0.15 ( $\blacksquare$ ), 0.27 ( $\triangle$ ), 0.38 ( $\bullet$ ) and 0.49 ( $\square$ ).

Figure 5.4 – Spectra of ternary samples with  $\varrho = 5.7$ .

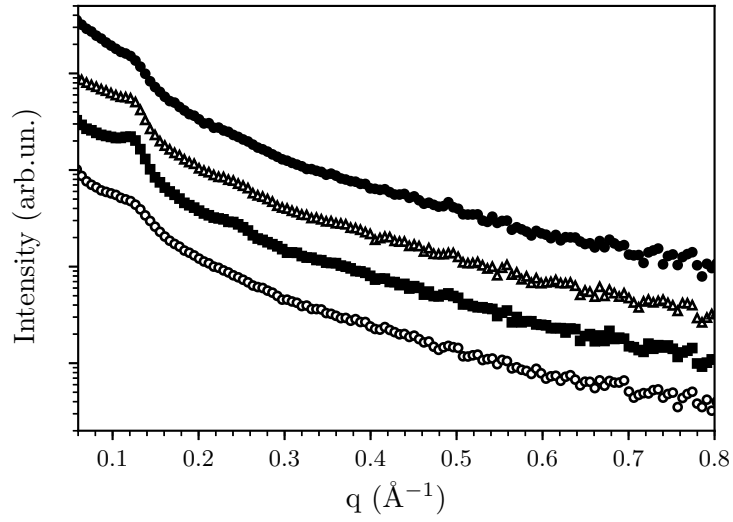


(a) SAXS spectra for water mass fraction of: 0.02 ( $\circ$ ), 0.16 ( $\blacksquare$ ), 0.30 ( $\triangle$ ), 0.43 ( $\bullet$ ), 0.54 ( $\square$ ), 0.65 ( $\blacktriangle$ ) and 0.84 ( $\diamond$ ).

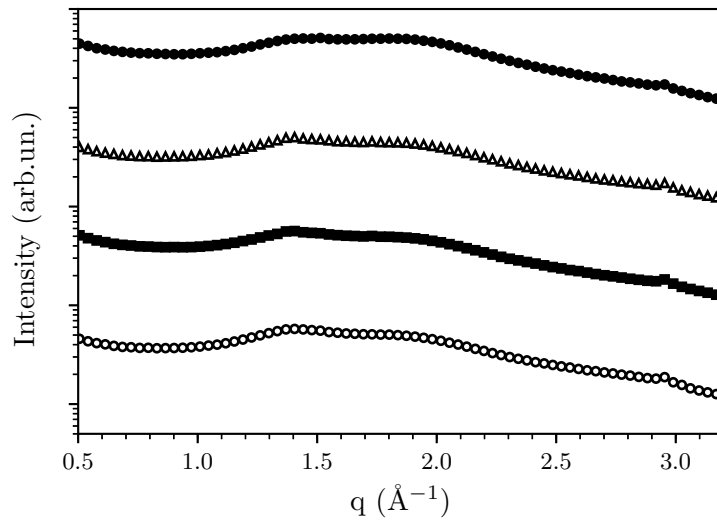


(b) WAXS spectra for water mass fraction of: 0.02 ( $\circ$ ), 0.16 ( $\blacksquare$ ), 0.30 ( $\triangle$ ), 0.43 ( $\bullet$ ), 0.54 ( $\square$ ), 0.65 ( $\blacktriangle$ ) and 0.84 ( $\diamond$ ).

Figure 5.5 – Spectra of ternary samples with  $\varrho = 4.3$ .



(a) SAXS spectra for water mass fraction of: 0.04 ( $\circ$ ), 0.15 ( $\blacksquare$ ), 0.31 ( $\triangle$ ) and 0.46 ( $\bullet$ ).



(b) WAXS spectra for water mass fraction of: 0.04 ( $\circ$ ), 0.15 ( $\blacksquare$ ), 0.31 ( $\triangle$ ) and 0.46 ( $\bullet$ ).

Figure 5.6 – Spectra of ternary samples with  $\varrho = 2.9$ .

characteristic of the water molecules gets more intense, if compared to the hump characteristic of the simulsol molecules. In addition, POM observations of the system revealed the presence of birefringence with no phase separation. These experiments show that water is macroscopically incorporated to the system, but the molecules are not inserted in between the layers of the smectic phase at the microscopic scale.

When  $\rho$  is decreased, as shown in Figure 5.5, equivalent results are observed. The increasing of the amount of water molecules, whose presence is confirmed by WAXS experiments, does not swell the structure. Besides, the lamellar organisation has the same stacking period as the previous composition.

Nevertheless, we can observe for the most diluted sample ( $\varphi_{\text{water}} = 0.84$ ), only the presence of the first order peak, which is also much less intense than the one observed in the less hydrated samples, although its position does not change compared to the previous series of samples. These results show that the stacking period is not dependent on the proportion between simulsol and GO or hydration, for the investigated domain.

Equivalent results are again obtained for the series of samples less charged in simulsol, shown in Figure 5.6. All the presented spectra exhibit Bragg's peaks at the same position observed before, although their intensities are not very high compared to the previous compositions.

These results show that, when formulated, the ternary system form a lamellar phase with a constant periodicity of  $\approx 5$  nm, that does not depend on the proportion between GO sheets and surfactant, nor on the hydration of the system. However, the observations after three weeks of homogenisation revealed a dependency on the stability of this phase with the composition of the system.

For more hydrated systems, the structure seems to loose faster the correlation of the lamellar organisation. The same effect is observed for systems less charged in surfactant. The characterisation of this phase is still to be developed, however, a study of the kinetics of this phase has been developed, in order to evaluate the time needed for the system to stabilise.

A few samples were formulated with a same composition, *i.e.*  $\rho = 1.8$  and  $\varphi_{\text{water}} = 0.71$ , and analysed after different durations of homogenisation. The stability of the sample in time was followed using SAXS and, in Figure 5.7, one can observe the evolution of the spectra.

The obtained results show that, after shorter stabilisation times, the shape of the curves obtained for the investigated samples does not suffer big modifications. The curves show the presence of characteristic peaks of a lamellar phase, corresponding to  $d \approx 5$  nm. However, the intensity of the peaks decreases with the ageing of the sample, which clearly indicates that reaching equilibration requires a large amount of time during which structural changes may occur.

For the longest equilibration time investigated, the first order Bragg's peak is barely visible, may possibly have moved towards smaller scattering angles and higher order

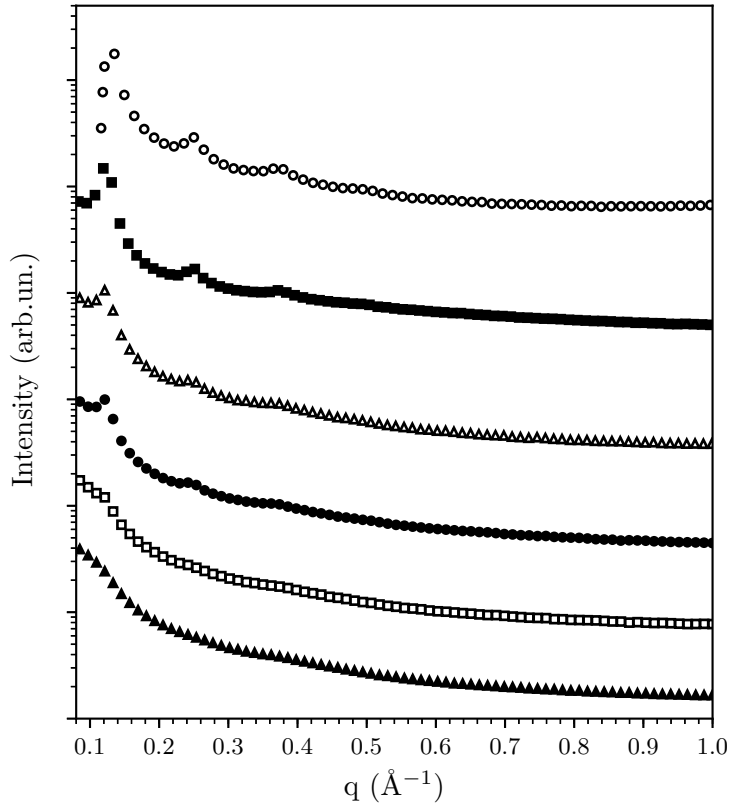


Figure 5.7 – Evolution of SAXS spectra of a ternary sample after: 10 ( $\circ$ ), 14 ( $\blacksquare$ ), 19 ( $\triangle$ ), 21 ( $\bullet$ ), 28 ( $\square$ ) and 40 ( $\blacktriangle$ ) days.

peaks cannot be detected. These observations indicate that the system composed of GO and surfactant presents a slow equilibration process, when compared to its components separately dispersed in aqueous solutions.

Equivalent experiments were carried out varying the proportion between surfactant and GO in the system and the obtained results revealed a dependency in the equilibrium time with  $\varrho$ . The higher the value of  $\varrho$ , the longer will be the time needed for the stabilisation of the system, reaching up to three months for the systems highly concentrated in simulsol.

The long time of stabilisation makes the study of this system practically very difficult, especially when a limited time is available, as in a thesis project. However, after the homogenisation of the samples, the system can be investigated and the obtained phases characterised.

### 5.3 Binary (dehydrated) GO-surfactant complexes

In a first approach, the study will be focused on the investigation of the binary system composed of GO sheets and surfactant. To obtain these samples, the initial step is to prepare a ternary complex with the wanted  $\varrho$ , as described in the section above. After the equilibrium is reached (which may require a very long time), the sample is placed in

the vacuum chamber, where the pressure is controlled, to slowly dehydrate.

The pressure is regulated as a function of the hydration of the system, meaning that the more dehydrated the complex, the lower the pressure inside the chamber, reaching around 5 mbar in the final stage of dehydration. The mass lost by the sample is controlled, similarly to the procedure employed for the binary GO-water system. When the mass of the sample reaches a plateau, the sample is considered to be completely dried. The whole dehydration process can last up to 35 hours. In opposition to what was observed with the binary system GO-water, the water is almost completely removed from the ternary complexes, as observed in the evolution of the mass of the ternary samples during dehydration.

A series of samples was prepared varying the proportion of simulsol and GO, followed by the dehydration procedure after the stabilisation was reached. Although the viscosity of the samples does not allow their observation under POM, they were analysed by X-ray scattering. The obtained results are presented in Figure 5.8.

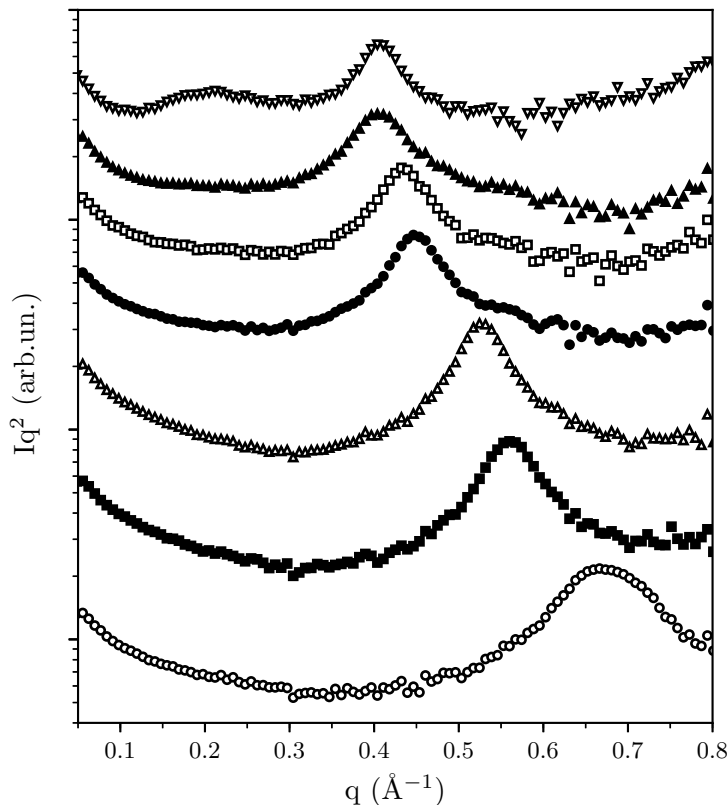


Figure 5.8 – SAXS spectra of GO sheets and surfactant with GO volume fraction of: 0.57 (○), 0.46 (■), 0.36 (△), 0.26 (●), 0.19 (□), 0.15 (▲) and 0.10 (▽).

One can observe, for the more concentrated sample in GO, the presence of a peak, which dislocates to smaller values of  $q$  when the amount of surfactant is increased. This peak could be related to a lamellar structure and, to verify this hypothesis, WAXS experiments were carried out for this sample. The obtained result is shown in Figure 5.9.

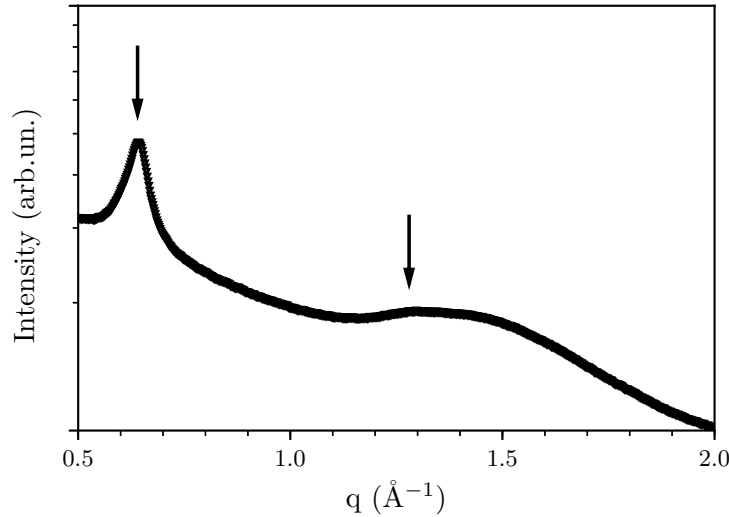


Figure 5.9 – WAXS spectrum of GO sheets and surfactant with GO volume fraction of 0.57.

It is possible to see in the curve the presence of the same characteristic peak observed before, at  $q \approx 0.65 \text{ \AA}^{-1}$ . The presence of a second order peak, which can be seen at  $q \approx 1.3 \text{ \AA}^{-1}$ , although it is partly hidden in the hump characteristic of the distance between the surfactant molecules, confirms the formation of a lamellar structure.

These results show that, when the amount of surfactant is increased in the system, the period of the lamellar stacking increases, which means that the observed structure is a lamellar phase of GO that is diluted by the simulsol molecules. The phenomenon is similar to the swelling of lyotropic liquid crystals, where the surfactant plays the role of the solvent in this particular system, swelling the stacked GO sheets.

For systems highly concentrated in simulsol, one can observe that the position of the peak does not change, which means that a dilution limit has been reached. The occurrence of the dilution limit is observed starting from  $\varphi_{GO} = 0.15$ .

Moreover, for even higher amounts of simulsol, one can see the appearance of a new hump for smaller values of  $q$ . The detected hump can be compared to the curve of the pure simulsol system, and both spectra are presented in Figure 5.10.

The SAXS results show that, after swelling the stacked GO sheets to its limit, the amphiphiles in excess will form a new phase, which consists in a structured liquid, apparently equivalent to the one observed for pure simulsol.

To proceed further in a quantitative analysis, the lamellar periodicity is calculated for each one of the samples. Concerning the phase in excess, a characteristic distance was calculated from the position of the hump, a procedure homologous to the one executed for the surfactant-water system (section 5.1).

The dilution line of the GO sheets dispersed in simulsol, in the whole investigated domain, is presented in Figure 5.11.

The presented results suggest that, for highly concentrated samples in GO, the sur-

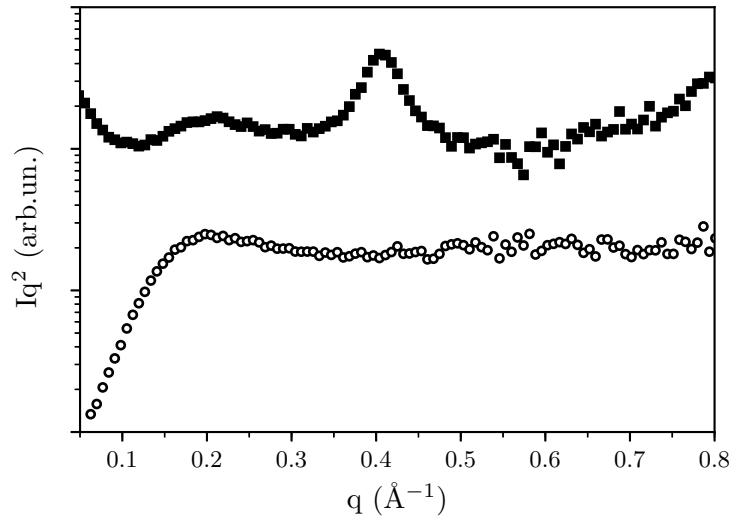


Figure 5.10 – Comparison between the SAXS spectra for  $\varphi_{GO} = 0.0$  (○) and  $\varphi_{GO} = 0.10$  (■).

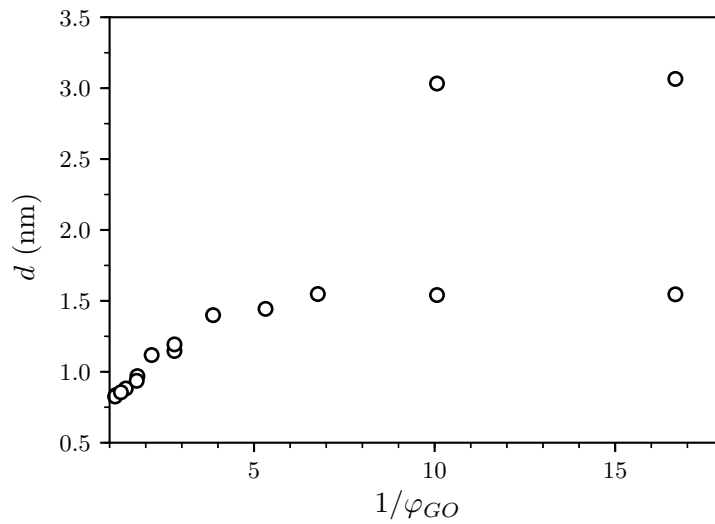


Figure 5.11 – Lamellar periodicity as a function of the inverse of GO volume fraction.

factant molecules are lying parallel to the surface of the sheets, which gives a lamellar periodicity for the system no higher than the thickness of a GO layer, *i.e.* in the order of 0.8 nm.

When the amount of simulsol in the system is increased, the molecules will compete for space in the surface of the GO layer. In this condition, the simulsol molecules will then start to reorient themselves, presumably with the hydrophilic part in contact with the GO sheet and the hydrophobic one to the outside, which increases the distance of separation between the layers.

This phenomenon takes place until the dilution limit is reached, when the hydrophobic part of the amphiphiles is straightened up. This organisation of the surfactant molecules is very similar to a bilayer-like structure, in which case the hydrophobic parts form a double layer, with the hydrophilic parts attached to the surface of the GO sheets. The described structure is schematically represented in Figure 5.12.

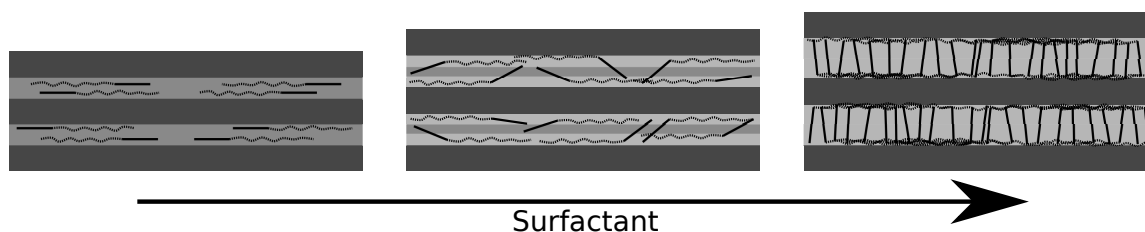


Figure 5.12 – Schematic representation of the swelling of GO sheets lamellar structure with surfactant. The darker layer in the scheme of the GO sheet represents its inner part and the clearer ones represent the outer part, which corresponds to the oxygen groups. The continuous and dashed parts of the surfactant represent, respectively, the hydrophobic and hydrophilic groups. The amount of surfactant increases from the left to the right.

At this point, the lamellar periodicity of the structure reaches  $d \approx 1.5$  nm, which is compatible to the stacking distance at which the anomalous behaviour in the swelling of the binary GO-water system takes place, indicating that both phenomena can be related.

Comparing the structure obtained before the dilution limit is reached with the highly confined GO layers in water, we can picture a structure where the GO sheets are stacked, with the oxygen groups of neighbouring layers overlapped, as the lamellar periodicity is smaller than  $15 \text{ \AA}$ , value obtained for the thickness of the GO. The amphiphiles organise themselves in between the GO sheets and, when the dilution limit is reached, the oxygen groups are no longer overlapped and the simulsol structured.

From this point, it can be postulated that no more space is available in the surface of the GO layers and the additional amphiphiles cannot swell the stacked layers. The molecules in excess will form a new phase, coexisting with the previous one.

The new phase exhibits a structural distance of 3.0 nm, comparable to the characteristic distance observed for the pure simulsol, which can be considered a structured liquid. The exact structure of this system is still to be determined.

Following this study of the binary GO-surfactant system, it is now possible to investigate the addition of water to the obtained complexes.

## 5.4 Ternary (hydrated) GO-surfactant complexes

The procedure of preparation of the ternary samples has already been discussed in section 5.2. However, after adding simulsol to the ultracentrifuged GO dispersion, one of the two different steps presented below can be followed, if necessary.

1. To obtain a more diluted system, water is added, when the sample is formulated, in the right proportion to reach the wanted concentration and it is stored for homogenisation;
2. To obtain a more concentrated system, the formulated sample is stored and, after homogenisation, it is placed in the vacuum chamber to dehydrate. The mass of the sample is controlled during the procedure and the dehydration is stopped when the system reaches the wanted concentration.

The use of this method allows to explore the complete phase diagram of the ternary complexes, following water dilution lines. New series of samples, where the hydration is varied for a given proportion between surfactant and GO, were prepared. The viscosity of the sample depends on the amount of water on the system, which means that, the more dehydrated the sample, the more difficult is its observation in microscopy.

Nevertheless, in the hydrated domain, POM images were recorded for a few samples and are presented in Figure 5.13.

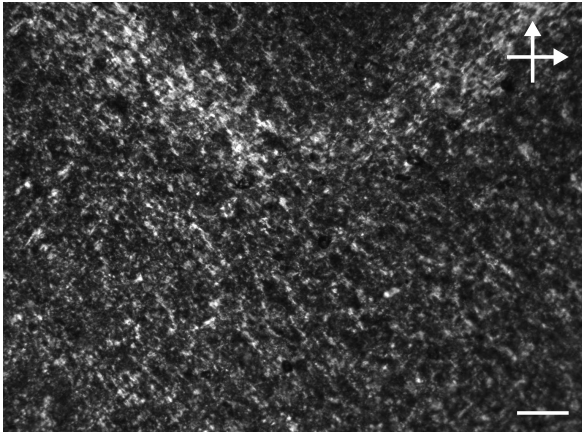
It is possible to observe that all the samples are optically birefringent, indicating the presence of an organised system. To obtain more information about the structure of the complexes, SAXS experiments were carried out in each one of the samples and the results of two of the series of samples, with  $\varrho = 1.8$  and  $\varrho = 5.8$ , are presented in Figure 5.14 and Figure 5.15, respectively.

In the series less charged in simulsol (Figure 5.14), it is possible to observe a peak characteristic of a lamellar structure for the less hydrated sample. When water is added to the system, the position of the peak moves towards smaller scattering angles, indicating an increase in the lamellar periodicity. This means that the phase is swelled, until it reaches a constant value, at  $q \approx 0.4 \text{ \AA}^{-1}$  for this value of  $\varrho = 1.8$ . One can also notice that the intensity of the peak decreases with the hydration of the complex.

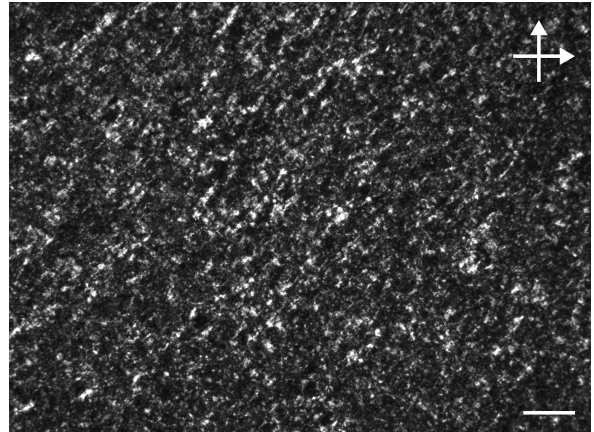
For the system with  $\varphi_{\text{water}} = 0.35$ , it is possible to see the appearance of a second peak, with a smaller value of  $q$ . The appearance of the new structured phase seems to be related to the fact that a dilution limit is reached as it appears when the peak associated to the lamellar structure does not move any more.

At contrast, the peak characterising the second phase moves towards smaller values of scattering vector when the system is hydrated. In addition, it is possible to see that the intensity of this peak increases when water is added.

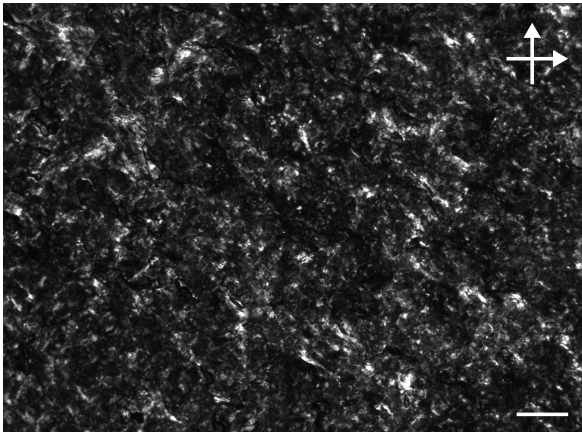
These results indicate that the lamellar phase, obtained with this system, is swelled when water is added, until it reaches a dilution limit. The limit of the stacking period



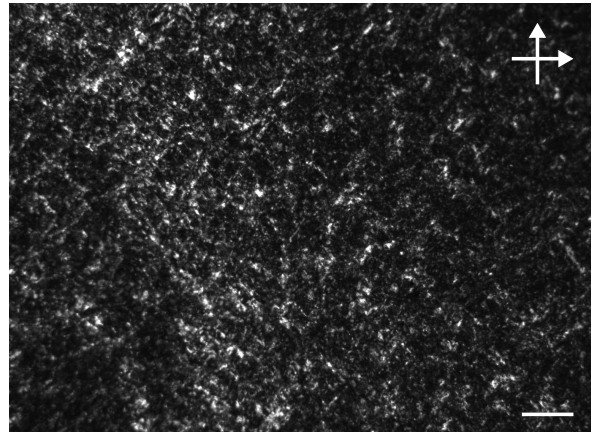
(a)  $\varrho = 0.75$  and  $\varphi_{\text{water}} = 0.93$ .



(b)  $\varrho = 1.80$  and  $\varphi_{\text{water}} = 0.83$ .



(c)  $\varrho = 4.3$  and  $\varphi_{\text{water}} = 0.38$ .



(d)  $\varrho = 9.0$  and  $\varphi_{\text{water}} = 0.61$ .

Figure 5.13 – POM images with crossed polarizer and analyser of ternary systems. The scale bars are equivalent to  $100 \mu\text{m}$ .

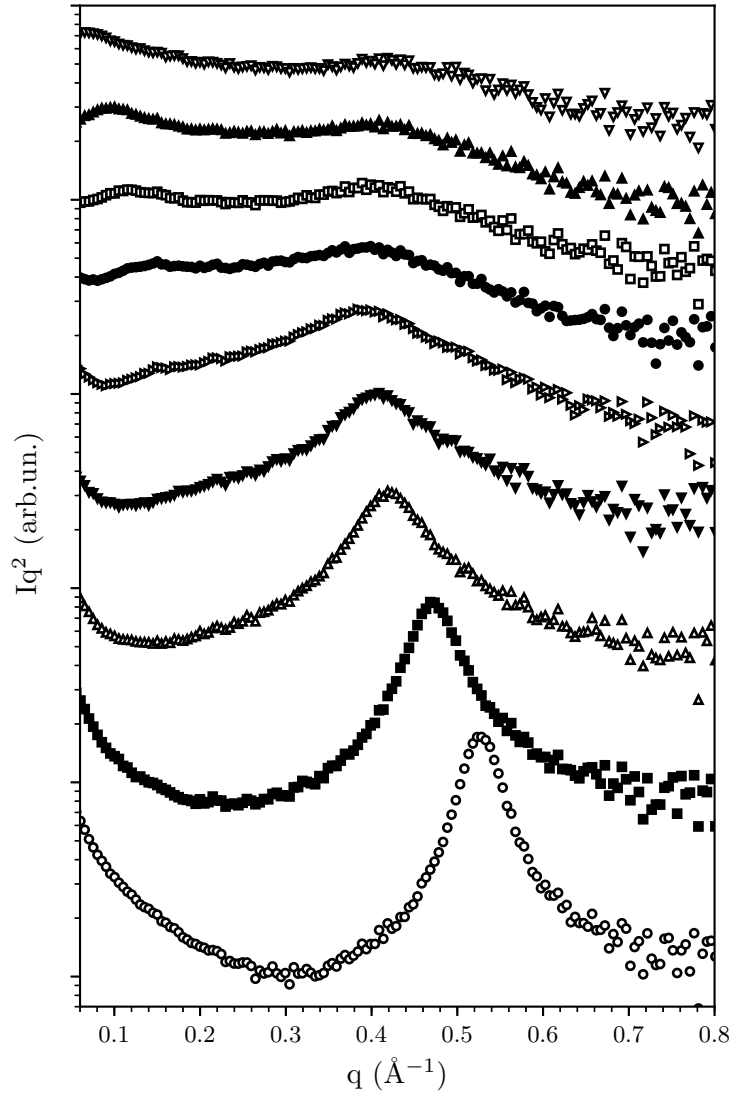


Figure 5.14 – SAXS spectra of ternary samples with  $q = 1.8$  and water mass fraction of: 0.0 ( $\circ$ ), 0.13 ( $\blacksquare$ ), 0.25 ( $\triangle$ ), 0.35 ( $\blacktriangledown$ ), 0.46 ( $\triangleright$ ), 0.56 ( $\bullet$ ), 0.65 ( $\square$ ), 0.74 ( $\blacktriangle$ ) and 0.83 ( $\nabla$ ).

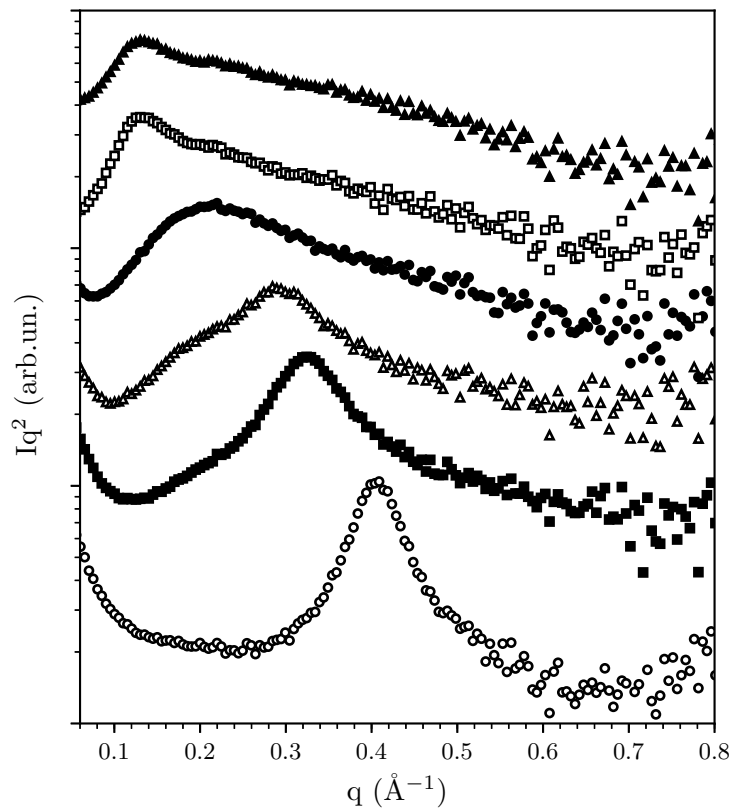


Figure 5.15 – SAXS spectra of ternary samples with  $\varrho = 5.8$  and water mass fraction of: 0.0 ( $\circ$ ), 0.11 ( $\blacksquare$ ), 0.18 ( $\triangle$ ), 0.31 ( $\bullet$ ), 0.43 ( $\square$ ) and 0.53 ( $\blacktriangle$ ).

in the ternary system is around 1.6 nm, very close to the limit observed for the binary GO-surfactant complex.

From the observations, it is possible to presume that this lamellar phase, obtained for the ternary complex and described above, has an organisation that is equivalent to the lamellar phase obtained for the binary GO-simulsol system. The water molecules will insert themselves in the surface of the GO sheets, replacing the hydrophilic part of the simulsol, which prevents their contact with the carbonic chains. The results show that the swelling phenomenon is equivalent using water or surfactant molecules, as the volume occupied between the GO layers by these molecules is the same.

After reaching the dilution limit, if water is still added in the system, the new phase appears, with a higher characteristic structural scale. The new phase can also be swelled when the system is hydrated.

Similar results are obtained for the experiments carried out in the series of samples containing a higher proportion of surfactant ( $\varrho = 5.8$ , see Figure 5.15).

Once more, one can observe, for the less hydrated samples, the peak of the lamellar organisation of the binary GO-surfactant that is swelled when water is added to the system. However, a second phase is observed for  $\varphi_{\text{water}} = 0.11$ , that can, apparently, also be swelled. The relative intensity between the first and second phases peaks also changes.

For this composition, no dilution limit is observed for the first phase, whose peak dislocates for lower  $q$ , until it cannot be distinguished from the peak of the second phase for  $\varphi_{\text{water}} = 0.31$ . When the hydration is increased, the SAXS spectra show the presence of a new phase. The shape of the more hydrated curve is very similar to the one observed for the previous composition, which may indicate that the systems have the same organisation.

In order to try to identify these organisations, the spectra of systems with almost constant simulsol and water contents are presented in Figure 5.16 and Figure 5.17, respectively. Note that the *preparation* dilution lines (varying the amount of water) are no longer followed in such a presentation. A practical consequence is that the studied samples are less closely located on the chosen lines than when water dilutions are presented. For the more hydrated systems presented in Figure 5.16, the experiments were carried out in a smaller window of  $q$  for a better visualisation of the characteristic peaks.

It is possible to observe in Figure 5.16 that the lamellar phase of GO sheets with simulsol in the surface is swelled with addition of water, because of the dislocation of the peak. For  $\varphi_{\text{water}} = 0.56$ , the new phase appears, characterised by a hump in smaller  $q$ . This phase is also swelled by hydration, and the system becomes monophasic again, until the binary surfactant-water lamellar phase is recovered for  $\varphi_{\text{water}} = 0.73$ , when the left-hand side of the ternary phase diagram is reached.

The position of the peaks for the two more hydrated samples are very close, although the shape of the curve are not very similar. This may indicate that the second phase observed is a lamellar stacking of surfactant bilayers, with the GO sheets in the aqueous

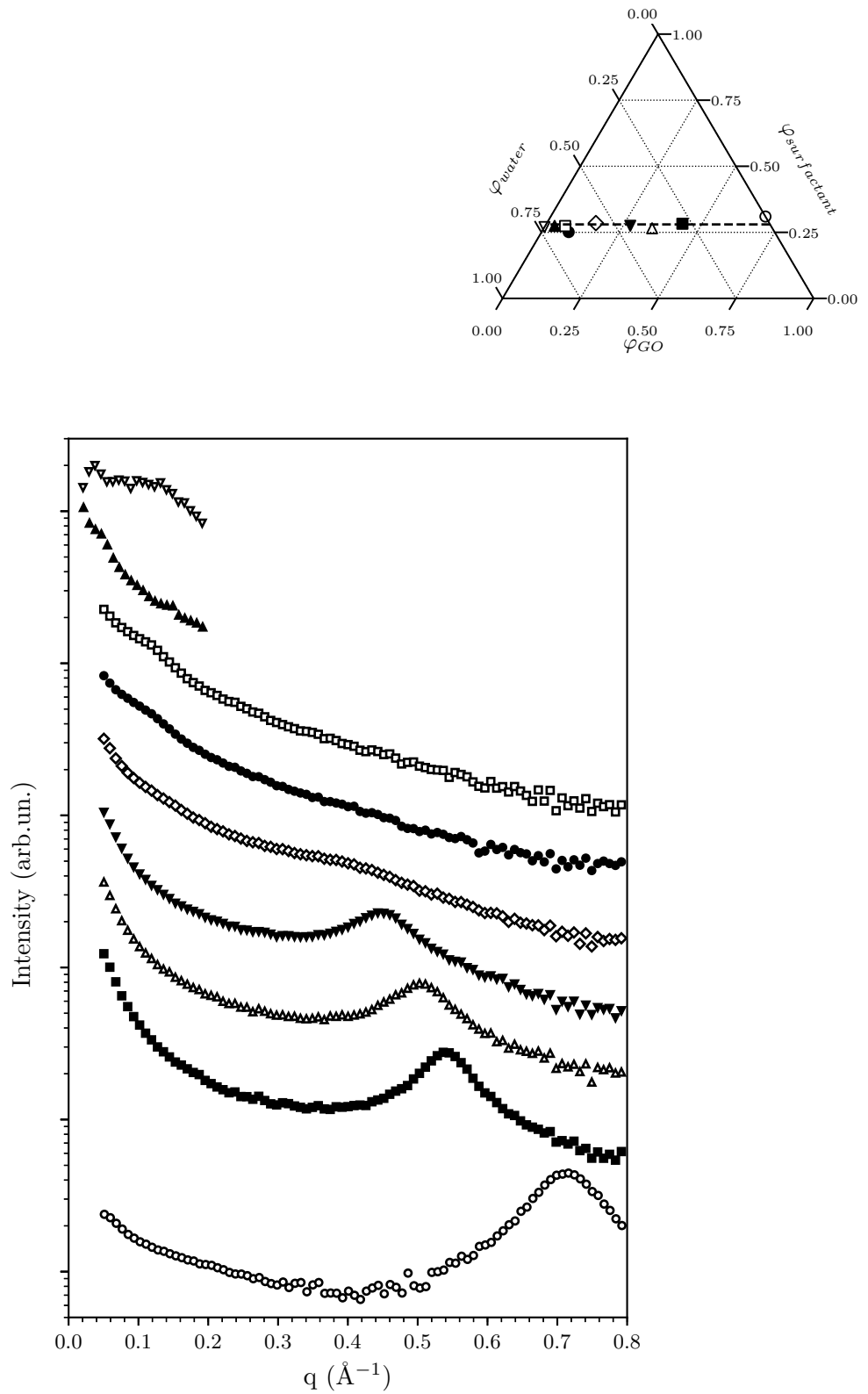


Figure 5.16 – SAXS spectra of systems with fixed  $\varphi_{surfactant} = 0.28 \pm 0.03$  and  $\varphi_{water}$  of: 0.0 ( $\circ$ ), 0.28 ( $\blacksquare$ ), 0.39 ( $\triangle$ ), 0.45 ( $\blacktriangledown$ ), 0.56 ( $\diamond$ ), 0.66 ( $\bullet$ ), 0.67 ( $\square$ ), 0.70 ( $\blacktriangle$ ) and 0.73 ( $\nabla$ ). The ternary diagram shows the position of each composition relative to the line corresponding to  $\varphi_{surfactant} = 0.28$  (dashed line).

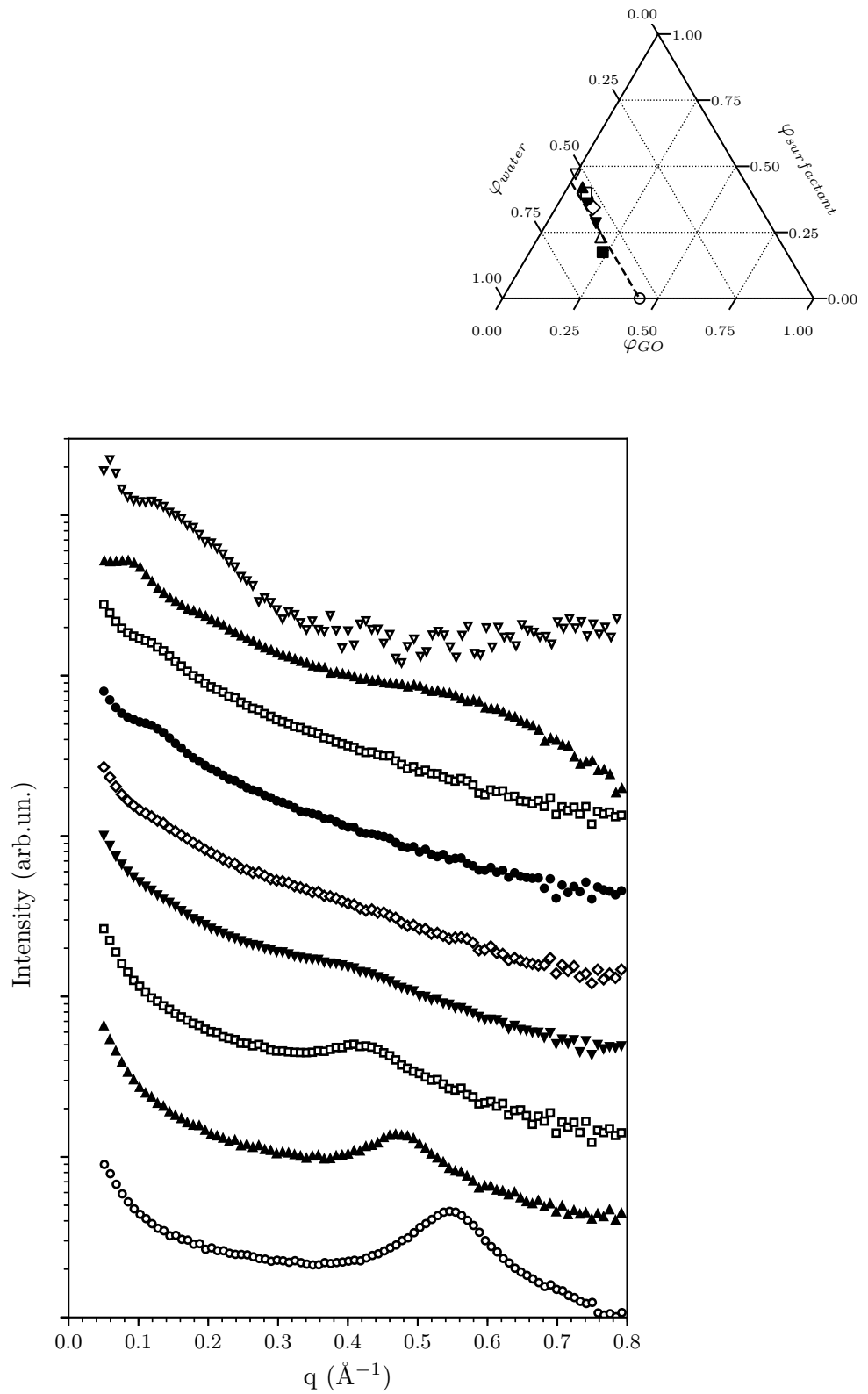


Figure 5.17 – SAXS spectra of systems with fixed  $\varphi_{water} = 0.56 \pm 0.03$  and  $\varphi_{surfactant}$  of: 0.0 ( $\circ$ ), 0.18 ( $\blacksquare$ ), 0.23 ( $\triangle$ ), 0.29 ( $\blacktriangledown$ ), 0.34 ( $\diamond$ ), 0.38 ( $\bullet$ ), 0.40 ( $\square$ ), 0.42 ( $\blacktriangle$ ) and 0.47 ( $\nabla$ ). The ternary diagram shows the position of each composition relative to the line corresponding to  $\varphi_{water} = 0.56$  (dashed line).

layers that separate them.

In Figure 5.17, where the water volume fraction is fixed, broadly similar observations can be done. The binary lamellar phase of GO in water is swelled when simulsol (acting here as a co-solvent for dilution) is inserted in the system, because of the adsorption of the amphiphiles in the surface of the GO sheets.

When  $\varphi_{\text{surfactant}} = 0.34$ , the new phase appears and is swelled with the increasing in the number of surfactant molecules. For more concentrated samples, the first observed phase disappears and the new phase dilutes until the binary lamellar phase of simulsol and water is recovered, again when reaching the left-hand side of the ternary phase diagram. Once more, one can observe a continuous transition between the second phase observed for the ternary system and the periodically-stacked bilayers of simulsol in water.

These results suggest the formation of two distinct structures for the ternary system. The first phase, observed for smaller quantity of surfactant, is obtained by amphiphile molecules adsorbed in the surface of the GO layers, forming a stacked structure that can be swelled, as already discussed.

For higher proportions of simulsol and enough hydrated systems, the surfactant molecules will detach from the GO sheets, and organise themselves in bilayers. The GO sheets will be dispersed in the aqueous layer that separate the membranes, which corresponds to the second phase observed. The domains where each one of the phases can be obtained are separated by a zone of transition, where both phases may coexist. The described ternary structures are schematically represented in Figure 5.18.

With the SAXS results of all the investigated compositions, it is possible to plot the dilution lines for each one of the series of samples (going back to *water* dilutions for series differing in their  $\rho$  values), which are presented in Figure 5.19.

In Figure 5.19a, the dilution lines of the ternary system in the whole investigated range are presented, and one can observe the existence of two groups of curves. In the lower part of the figure, a group of curves, whose  $d$  is no higher than  $\approx 1.6$  nm, is observed and, in the upper part, the curves with higher lamellar periodicities. For a better visualisation and to facilitate the discussion, the groups of curves will be separated in different figures.

For the group of systems with smaller lamellar periodicities, which are presented in Figure 5.19b and corresponds to the systems with lower amount of surfactant, it is possible to observe that, for a given composition, the phase is swelled until it reaches a dilution limit. The limiting distance of periodic stacking seems to have a common value for the investigated systems, *i.e.*  $d \approx 1.5$  nm.

One can observe that the dilution limit is not dependent on the proportion of GO and simulsol. Moreover, the limit of the stacking period is compatible to the value of periodicity at which the anomaly in the GO-water system takes place. This behaviour was already qualitatively described, which means that this group of curves corresponds to the first proposed phase, where stacked GO sheets are adsorbed with amphiphiles and water in their surface.

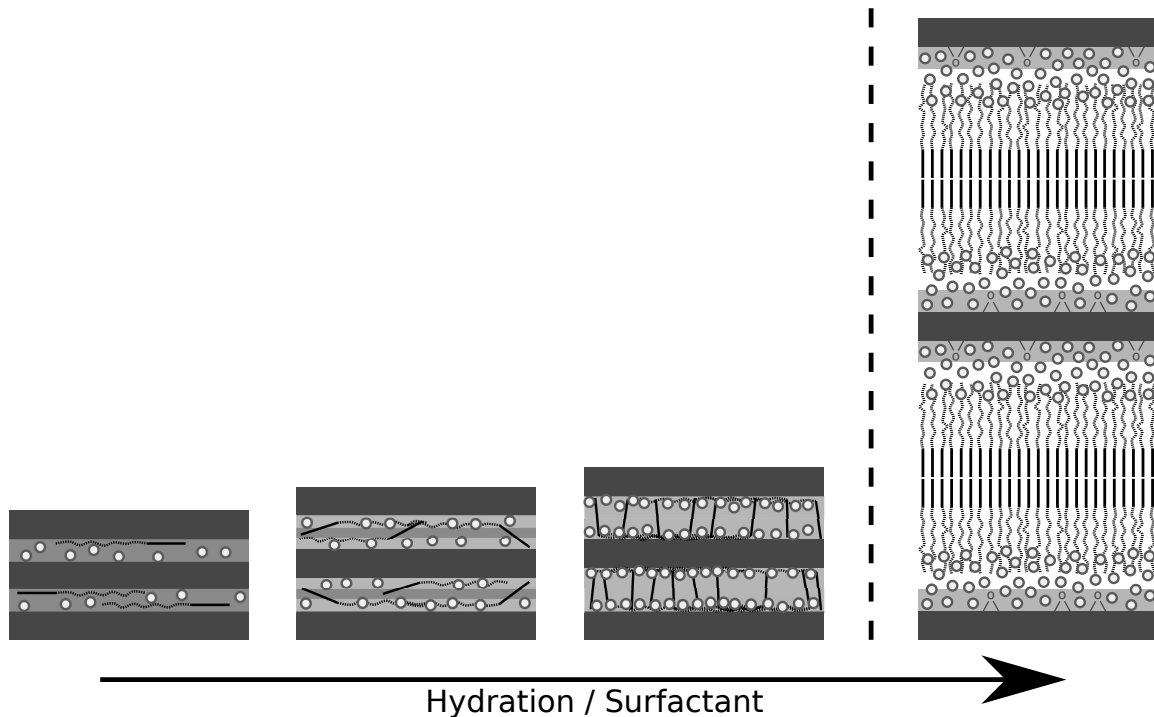


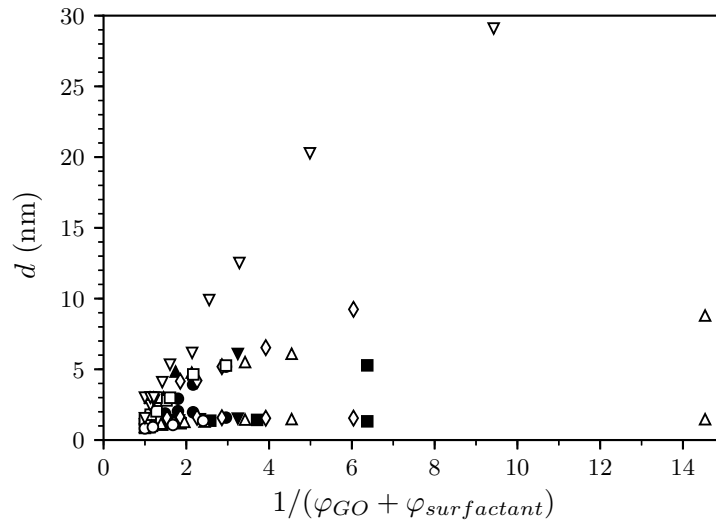
Figure 5.18 – Schematic representation of the obtained ternary structures and the phase transition. The darker layer in the scheme of the GO sheet represents its inner part and the clearer ones represent the outer part, which corresponds to the oxygen groups. The continuous and dashed parts of the surfactant represent, respectively, the hydrophobic and hydrophilic groups. The water molecules are represented by circles. The amount of water and/or surfactant increases from the left to the right.

Nevertheless, a few of the systems presented previously contain more than one structure. In Figure 5.19c, both observed phases in the biphasic samples are presented. One element that can be noticed is the decreasing in the amount of water needed for the second phase to appear, when the proportion of simulsol is increased. As an example, for  $\varrho = 0.31$ , the biphasic samples are not observed before  $1/(\varphi_{GO} + \varphi_{\text{surfactant}}) \approx 6.3$ , while for  $\varrho = 2.9$ , the second phase is observed when  $1/(\varphi_{GO} + \varphi_{\text{surfactant}}) \approx 1.7$ . This result reinforces the hypothesis that the phase transition of the ternary complexes is directly related to the structural transition of the binary GO-water system.

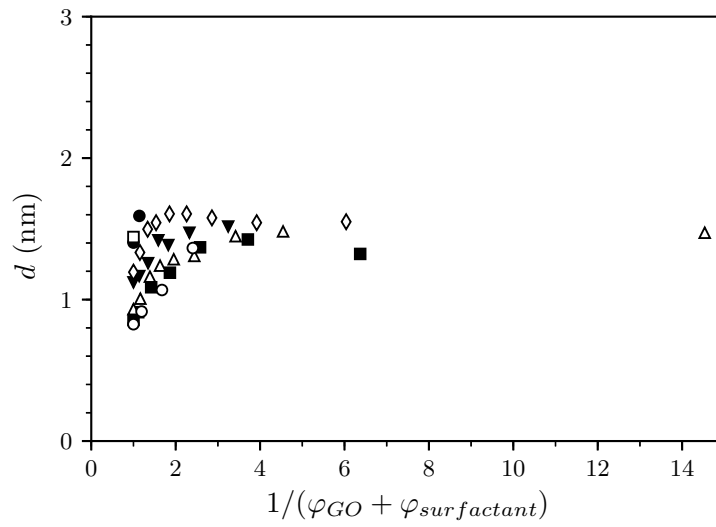
In Figure 5.19d, the monophasic systems containing only the points in the upper group of curves and only the second phase for the biphasic samples showed previously, are presented. It is possible to observe that the lamellar period increases with the addition of surfactant for a given water volume fraction. This effect can be observed for two compositions where  $1/(\varphi_{GO} + \varphi_{\text{surfactant}}) \approx 6.3$ , when the obtained lamellar periodicities are 5.3 nm and 9.2 nm for  $\varrho = 0.31$  and  $\varrho = 1.8$ , respectively.

These observations indicate that, increasing the surfactant proportion, the swelling limit of the lamellar phase also increases. For the series corresponding to the highest proportion in simulsol, it is possible to see that the dilution limit is not observed. The phase obtained for this group of curves corresponds to simulsol bilayers in a lamellar organisation with GO and water in between the layers.

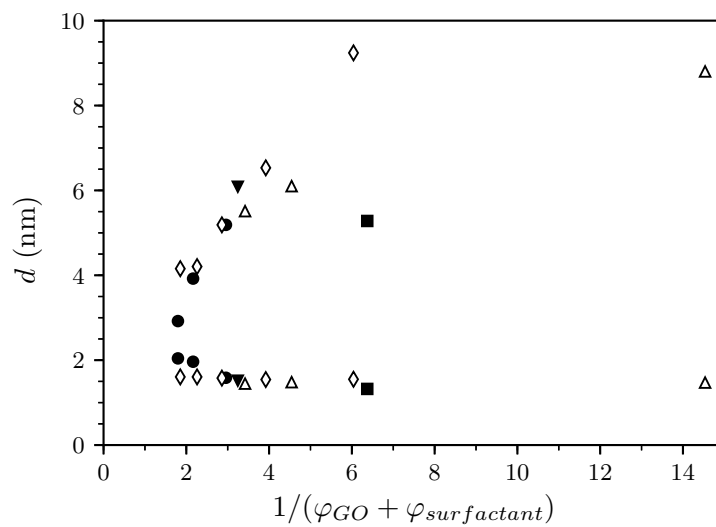
The series of samples with  $\varrho = 9.0$  can be compared to the dilution line of the binary



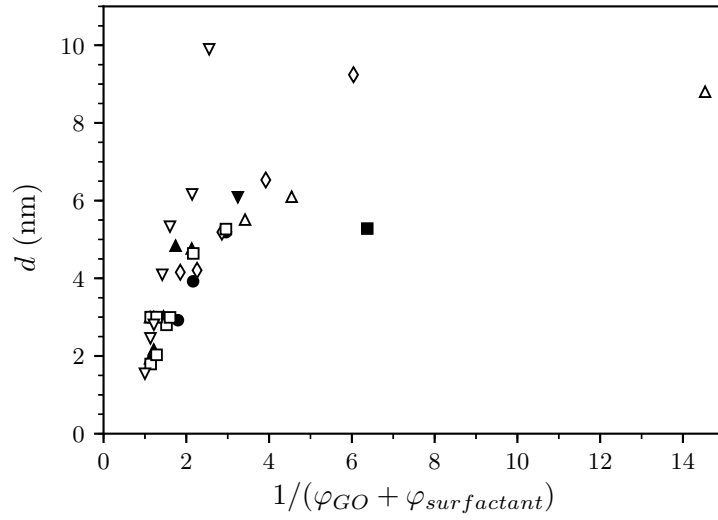
(a) Dilution lines of the ternary systems in the whole investigated range.



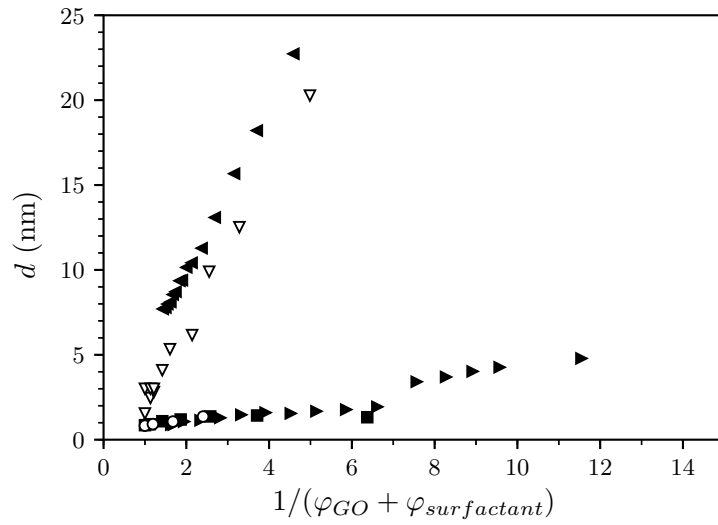
(b) Dilution lines of the first group of curves of the ternary systems.



(c) Dilution lines of the biphasic ternary systems.



(d) Dilution lines of the second group of curves of the ternary systems.



(e) Comparison between the dilution lines of the ternary and binary systems.

Figure 5.19 – Dilution lines of the binary systems with  $\varphi_{GO} = 0$  ( $\blacktriangleleft$ ) and  $\varphi_{surfactant} = 0$  ( $\blacktriangleright$ ), ternary systems with  $\varrho$  of: 0.15 ( $\circ$ ), 0.31 ( $\blacksquare$ ), 0.75 ( $\triangle$ ), 1.17 ( $\blacktriangledown$ ), 1.80 ( $\diamond$ ), 2.9 ( $\bullet$ ), 4.3 ( $\square$ ), 5.8 ( $\blacktriangle$ ) and 9.0 ( $\nabla$ ).

simulsol and water system. The curves are presented in Figure 5.19e, as well as the binary GO-water system and a few ternary complexes from the lower group of dilution lines. It is possible to observe that the GO-water binary system overlaps the first group of samples, with small proportion of simulsol, while the surfactant-water binary system is very close to the richest series in simulsol, confirming the interpretation given for the observed phases of the complexes.

Combining the results of all the studied systems, it is possible to construct a ternary phase diagram summing up all the observations, which is presented in Figure 5.20.

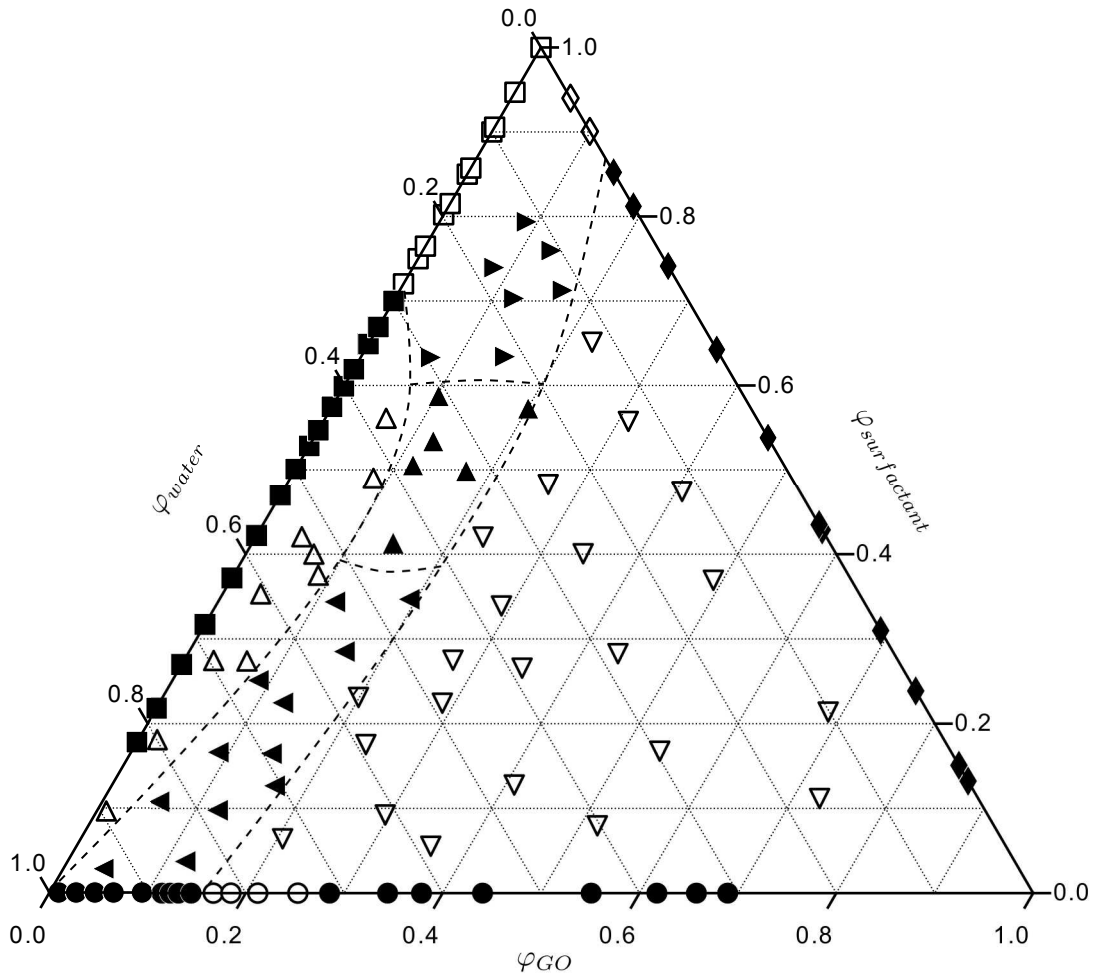


Figure 5.20 – Ternary phase diagram. Lamellar phase of GO sheets in water (●) and region of structural anomaly (○). Lamellar phase of surfactant in water (■) and unknown surfactant-water phase (□). Lamellar phase of GO sheets in surfactant (◆) and biphasic domain (◇). Lamellar phase of GO with surfactant in the surface (▽), lamellar phase of surfactant with GO and water in between (△) and transition domain with different phases (◀, ▲ and ▶).

This diagram shows the domain of existence of the different observed phases. The systems containing higher amounts of GO and smaller quantities of simulsol, whose compositions are represented by  $\nabla$  in the diagram, are formed by monophasic samples.

As already described, this phase is obtained with a lamellar organisation of GO sheets with the simulsol molecules attached to their surface. The hydrophilic part of the am-

phiphile will be in the plane of the GO sheet, while the hydrophobic one will be exposed to outside. This phase can be diluted either by the water or surfactant molecules, until it reaches the dilution limit and a new phase appears.

From the diagram, it is possible to see that the phase transition of the ternary complex occurs at  $\varphi_{GO} \approx 0.14$ , which is not dependent on the  $\varrho$  of the system. This transition is directly related to the anomalous behaviour of the binary GO-water system.

The transition domain shown in the diagram, which corresponds to a region with low amount in GO, compared to the domain described above, can be divided in three parts. In the region represented by  $\blacktriangleleft$ , the previous phase is present coexisting with a second one. The second phase is characterised by surfactant bilayers organised in a lamellar structure separated by water. The GO sheets will be dispersed in the aqueous layers, between the membranes.

For a small domain in the diagram, represented by  $\triangle$ , the monophasic systems containing this new phase are obtained. This organisation is only accessible in the lamellar domain of the binary surfactant-water system.

When the proportion of surfactant is increased, which corresponds to the non lamellar structure in the binary simulsol-water system, a biphasic domain is observed, represented by  $\blacktriangleright$ . In this region, one of the observed phases is the first described phase, where the GO sheets are stacked with water and simulsol molecules attached to their surface. The other phase is composed of amphiphiles in excess and water, corresponding to the phases observed for the binary GO-surfactant system. In this region, the simulsol in excess will form an structured liquid, as it is observed for the binary simulsol-water system.

Finally, in the central region, which is represented by  $\blacktriangle$ , the obtained phase(s) could not be identified. This domain could be characterised by a new phase or a mixture of all the phases previously described.

The phase diagram puts in evidence the rich polymorphism of the GO-simulsol complexes. Real ternary complexes are obtained, with an organisation that depends on the composition of the system and the phase transitions being ruled by the respective binary complexes. These results also show the importance of the study of the respective binary complexes, located over the axis of the diagram, for a better interpretation of the phases.

# Chapter 6

## Conclusions

### 6.1 Results

In the work developed during this thesis, the confinement of graphene oxide (GO) sheets within an anisotropic fluid matrix composed of amphiphilic molecules and water has been studied. Prior to the study of the complexes of the ternary system, the binary system composed of GO and water has been investigated.

A procedure to obtain highly concentrated aqueous GO dispersions has been developed, which allowed the investigation of an extended concentration range of the dispersions. The obtained samples are free of aggregates and can be reversibly swollen or dehydrated, which is not achievable from dried sources of GO.

Small angle x-ray scattering experiments revealed that the aqueous GO dispersion behaves like a liquid crystals, where organised phases can be obtained with the increase in the concentration of the system. The obtained smectic phases obey the usual dilution law, characteristic of lyotropic liquid crystals, which is observed over the investigated hydration range.

The swelling behaviour of the aqueous GO dispersions can be interpreted in terms of the forces acting in the layers. The balance between the attractive and repulsive interactions will stabilise the lamellar structure, and the importance of the electrostatic repulsion in the hydrated domain, competing with other contributions to dilute the stacked structure, has been demonstrated.

Nevertheless, in a small domain of concentration, a discrepancy with the swelling law is observed, which may indicate a structural phase transition. Although the details of this phenomenon are still to be identified, this anomalous behaviour can be related to the fact that, for highly confined phases, the oxygen groups in the surface of the GO sheets are overlapped and, when the structure is diluted, the lamellar periodicity increases, breaking the contact between the layers. This phenomenon affects the interactions between the adjacent sheets, and the effect is detected in the dilution line.

For the more diluted GO dispersions, adapted SAXS models have been employed to

extract structural parameters of the investigated system. The shape and organisation of the layers have been studied.

The thickness of a GO layer, obtained from the electron density, is in good accordance with the value described in the literature. Considering different electron densities for the carbon plane and the oxygen groups, a thickness around 15 Å is obtained. The inner part of the GO layer, which measures around 6 Å, has a length that is compatible with the thickness of a graphene layer. Nevertheless, considering an average electron density for both parts of the sheet, the obtained thickness is approximately 10 Å.

The organised lamellar structures have also been characterised with the implemented models. The Caillé parameter, sensitive to the flexibility of the layers has been obtained, and its behaviour, as a function of the hydration of the system, has been investigated. These results led to the extraction of the compression modulus of the stacked structure. As expected for systems like the lamellar phase of GO dispersions, the smaller the distance between the layers, the higher the force necessary to dislocate the layers from their equilibrium spacing.

The binary system composed of surfactant and (acidic) water has also been investigated, though in lesser details. The experiments revealed the formation of bilayers of amphiphiles organised in a lamellar structure for mild concentrated systems. The structure also obeys the dilution law, being swelled when solvent is added to the system. However, a phase transition takes place for highly concentrated samples, and an undefined structure is observed.

These studies allowed the investigation of the dehydrated binary system composed of GO sheets and surfactant, which has further been rehydrated to provide the ternary complexes. The kinetics of the system showed that inconveniently long times are often needed for the structure to stabilise. The higher the proportions of surfactant and water in the system, the higher will be the duration of the homogenisation process.

For lower amount of surfactant, the GO layers will organise themselves in a stacked structure, where the amphiphiles will adsorb in the surface of the sheets. With the increasing in the amount of surfactant, the molecules will organise themselves in the surface, swelling the structure, until it reaches a dilution limit. At this point, the surfactant will form a bilayer-like structure, with the hydrophilic part of the molecule grafted in the GO sheet. For higher concentration of surfactant, the amphiphilic molecules in excess will form a separated phase, which is also structured.

The described phase can also be swelled by hydration, in which case the water molecules will insert themselves in the surface of the layers. For system with a high proportion in simulsol, representing a small domain in the ternary diagram, a new phase appears. In this phase, the amphiphilic molecules detach from the GO sheets and organise themselves in bilayers separated by water, with the GO sheets dispersed in the aqueous region. The two domains of the ternary diagram, where each one of the phases are observed, are delimited by a transition zone, in which both or multiple phases coexist.

Two distinct ternary complexes have been actually obtained, whose zones of existence are separated by a transition region. This transition domain is related to the transitions of the relevant binary systems. A few structures in the zones of transition are still to be characterised in details.

All the obtained results for the investigated systems allowed the construction of a ternary phase diagram, summing up the observed structures.

## 6.2 Perspectives

For a better comprehension of the binary system GO-water, the evidenced discrepancy with the swelling law, observed for the confined domain, could be investigated in more details. The results would be of great interest to the interpretation of the phase transitions observed in the ternary system. Techniques like the cryogenic electron microscopy or nuclear magnetic resonance spectroscopy could be employed.

Analogously, the characterisation of the phase observed for the binary surfactant-water systems, in the dehydrated domain, would give information about one of the biphasic regions found in the ternary diagram. These findings could be helpful to the interpretation of the phase transition of the ternary complexes.

The parameters obtained from the fitting using SAXS models are compatible to values presented in the literature, however, improvements in the fitting routine could provide more accurate results. Moreover, adapted models for the concentrated systems could also be developed, providing information about the confined structures and the anomalous behaviour of the dilution law in this domain.

In addition, theoretical models describing the ternary complexes could be implemented. This study would give valuable information about the structure and stability of the complexes, and the interpretations of the obtained phases could be verified.

The kinetics of the ternary complexes obtained before the homogenisation could also be investigated. This study would give information about the equilibration of the phase.

At last, the phase diagram shows the rich polymorphism of the ternary complexes. To verify if the observed phase transition, from a lamellar structure of GO sheets “decorated” with surfactants to GO sheets “sandwiched” between membranes, is dependent only in the anomalous behaviour of the dilution of the binary GO-water system, the study could be reproduced using surfactants with different lengths of the hydrophilic and/or hydrophobic parts.



# Bibliography

Seyed Hamed Aboutalebi, Mohsen Moazzami Gudarzi, Qing Bin Zheng, and Jang-Kyo Kim. Spontaneous formation of liquid crystals in ultralarge graphene oxide dispersions. *Advanced Functional Materials*, 21(15):2978–2988, aug 2011. URL <http://doi.org/10.1002/adfm.201100448>.

Shakhawan Al-Zangana, Maria Iliut, Gökçen Boran, Michael Turner, Aravind Vijayaraghavan, and Ingo Dierking. Dielectric spectroscopy of isotropic liquids and liquid crystal phases with dispersed graphene oxide. *Scientific Reports*, 6(1), aug 2016a. URL <http://doi.org/10.1038/srep31885>.

Shakhawan Al-Zangana, Maria Iliut, Michael Turner, Aravind Vijayaraghavan, and Ingo Dierking. Properties of a thermotropic nematic liquid crystal doped with graphene oxide. *Advanced Optical Materials*, 4(10):1541–1548, jun 2016b. URL <http://doi.org/10.1002/adom.201600351>.

Sung Jin An, Yanwu Zhu, Sun Hwa Lee, Meryl D. Stoller, Tryggvi Emilsson, Sungjin Park, Aruna Velamakanni, Jinho An, and Rodney S. Ruoff. Thin film fabrication and simultaneous anodic reduction of deposited graphene oxide platelets by electrophoretic deposition. *The Journal of Physical Chemistry Letters*, 1(8):1259–1263, mar 2010. URL <http://doi.org/10.1021/jz100080c>.

Martin A. Bates and Daan Frenkel. Nematic–isotropic transition in polydisperse systems of infinitely thin hard platelets. *The Journal of Chemical Physics*, 110(13):6553–6559, apr 1999. URL <http://doi.org/10.1063/1.478558>.

Pierre Bauduin, Sylvain Prevost, Pau Farràs, Francesc Teixidor, Olivier Diat, and Thomas Zemb. A theta-shaped amphiphilic cobaltabisdicarbollide anion: Transition from monolayer vesicles to micelles. *Angewandte Chemie International Edition*, 50(23):5298–5300, may 2011. ISSN 1521-3773. URL <http://doi.org/10.1002/anie.201100410>.

Natnael Behabtu, Jay R. Lomeda, Micah J. Green, Amanda L. Higginbotham, Alexander Sinitskii, Dmitry V. Kosynkin, Dmitri Tsentalovich, A. Nicholas G. Parra-Vasquez, Judith Schmidt, Ellina Kesselman, Yachin Cohen, Yeshayahu Talmon, James M. Tour, and Matteo Pasquali. Spontaneous high-concentration dispersions and liquid crystals

- of graphene. *Nature Nanotechnology*, 5(6):406–411, may 2010. URL <http://doi.org/10.1038/nnano.2010.86>.
- J. D. Bernal. The structure of graphite. *Proceedings of the Royal Society A: Mathematical, Physical and Engineering Sciences*, 106(740):749–773, dec 1924. ISSN 0950-1207. URL <http://doi.org/10.1098/rspa.1924.0101>.
- Bruce J. Berne and Robert Pecora. *Dynamic Light Scattering: With Applications to Chemistry, Biology, and Physics*. Dover Books on Physics Series. Dover Publications, 2000. ISBN 0486411559.
- Hari Krishna Bisoyi and Sandeep Kumar. Carbon-based liquid crystals: art and science. *Liquid Crystals*, 38(11-12):1427–1449, nov 2011. URL <https://doi.org/10.1080/02678292.2011.597882>.
- H. P. Boehm, A. Clauss, G. O. Fischer, and U. Hofmann. Das adsorptionsverhalten sehr dünner kohlenstoff-folien. *Zeitschrift für anorganische und allgemeine Chemie*, 316(3-4):119–127, jul 1962. URL <https://doi.org/10.1002/zaac.19623160303>.
- H. P. Boehm, R. Setton, and E. Stumpp. Nomenclature and terminology of graphite intercalation compounds (IUPAC recommendations 1994). *Pure and Applied Chemistry*, 66(9):1893–1901, jan 1994. URL <https://doi.org/10.1351/pac199466091893>.
- K. Bougis, R. Leite Rubim, N. Ziane, J. Peyencet, A. Bentaleb, A. Février, C. L. P. Oliveira, E. Andreoli de Oliveira, L. Navailles, and F. Nallet. Stabilising lamellar stacks of lipid bilayers with soft confinement and steric effects. *The European Physical Journal E*, 38(7), jul 2015. URL <https://doi.org/10.1140/epje/i2015-15078-3>.
- Kévin Bougis. *Fluctuations et interactions en situation de nano-confinement anisotrope*. PhD thesis, Université de Bordeaux, 2016. URL <https://tel.archives-ouvertes.fr/tel-01467066>.
- Savile Bradbury. *An Introduction to the Optical Microscope (Royal Microscopical Society Microscopy Handbooks)*. Oxford University Press, 1989. ISBN 0198564198.
- B. C. Brodie. On the atomic weight of graphite. *Philosophical Transactions of the Royal Society of London*, 149(0):249–259, jan 1859. URL <https://doi.org/10.1098/rstl.1859.0013>.
- Damien Brusselle, Pierre Bauduin, Luc Girard, Adnana Zaulet, Clara Viñas, Francesc Teixidor, Isabelle Ly, and Olivier Diat. Lyotropic lamellar phase formed from monolayered  $\theta$ -shaped carborane-cage amphiphiles. *Angewandte Chemie*, 125(46):12336–12340, nov 2013. ISSN 1521-3757. URL <http://doi.org/10.1002/ange.201307357>.

- Alain Caillé. Remarques sur la diffusion des rayons x dans les smectiques A. *Comptes rendus hebdomadaires des séances de l'Académie des sciences. Série B*, 274(14):891–893, apr 1972. URL <http://gallica.bnf.fr/ark:/12148/bpt6k5619055g/f83.item>.
- Jing Cao, Hua-Jie Yin, and Rui Song. Circular dichroism of graphene oxide: the chiral structure model. *Frontiers of Materials Sciences*, 7(1):83–90, jan 2013. URL <https://doi.org/10.1007/s11706-013-0192-x>.
- Giorgio Cinacchi and Alessandro Tani. The isotropic–nematic phase transition in hard, slightly curved, lens-like particles. *The Journal of Chemical Physics*, 141(15):154901, oct 2014. URL <https://doi.org/10.1063/1.4897565>.
- Giorgio Cinacchi and Alessandro Tani. Isotropic–nematic phase transition in hard platelets as described by a third-virial theory. *The Journal of Physical Chemistry B*, 119(17):5671–5676, apr 2015. URL <https://doi.org/10.1021/acs.jpcc.5b00389>.
- Laura J. Cote, Rodolfo Cruz-Silva, and Jiaying Huang. Flash reduction and patterning of graphite oxide and its polymer composite. *Journal of the American Chemical Society*, 131(31):11027–11032, aug 2009. URL <https://doi.org/10.1021/ja902348k>.
- Emerson Rodrigo Teixeira da Silva. *Structure and dynamics of DNA confined in-between non-cationic lipid membranes*. PhD thesis, Universities of São Paulo and Bordeaux, 11 2011. URL <https://tel.archives-ouvertes.fr/tel-00755050>.
- Budhadipta Dan, Natnael Behabtu, Angel Martinez, Julian S. Evans, Dmitry V. Kosynkin, James M. Tour, Matteo Pasquali, and Ivan I. Smalyukh. Liquid crystals of aqueous, giant graphene oxide flakes. *Soft Matter*, 7(23):11154–11159, oct 2011. URL <https://doi.org/10.1039/C1SM06418E>.
- Pierre-Gilles de Gennes and Jacques Prost. *The Physics of Liquid Crystals*. OXFORD UNIV PR, 1995. ISBN 0198517858.
- Dietrich Demus and Lothar Richter. *Textures of Liquid Crystals*. VEB Deutscher Verlag für Grundstoffindustrie, 1978. ISBN 3527257969.
- A. Di Mauro, R. Randazzo, S. F. Spano, G. Compagnini, M. Gaeta, L. D’Urso, R. Paolesse, G. Pomarico, C. Di Natale, V. Villari, N. Micali, M. E. Fragala, A. D’Urso, and R. Purrello. Vortexes tune the chirality of graphene oxide and its non-covalent hosts. *Chem. Commun.*, 52(89):13094–13096, 2016. URL <http://doi.org/10.1039/C6CC05177D>.
- Ingo Dierking and Shakhawan Al-Zangana. Lyotropic liquid crystal phases from anisotropic nanomaterials. *Nanomaterials*, 7(10):305, oct 2017. URL <http://doi.org/10.3390/nano7100305>.

- Dmitriy A. Dikin, Sasha Stankovich, Eric J. Zimney, Richard D. Piner, Geoffrey H. B. Dommett, Guennadi Evmenenko, SonBinh T. Nguyen, and Rodney S. Ruoff. Preparation and characterization of graphene oxide paper. *Nature*, 448(7152):457–460, jul 2007. URL <http://doi.org/10.1038/nature06016>.
- Per Ekwall. Composition, properties and structures of liquid crystalline phases in systems of amphiphilic compounds. In *Advances in Liquid Crystals*, pages 1–142. Elsevier, 1975. URL <http://doi.org/10.1016/b978-0-12-025001-1.50007-x>.
- L.A. Feigin and D.I. Svergun. *Structure Analysis by Small-Angle X-Ray and Neutron Scattering*. Springer, 1987. ISBN 0306426293.
- Krister Fontell, Leo Mandell, Heikki Lehtinen, and Per Ekwall. The three-component system sodium caprylate-decanol-water: III. the structure of the mesophases at 20°C. *Acta Polytechnica Scandinavica, Chemistry including metallurgy series*, 74(3):1–56, 1968. ISSN 0001-6853.
- R. E. Franklin. The structure of graphitic carbons. *Acta Crystallographica*, 4(3):253–261, may 1951. URL <http://doi.org/10.1107/s0365110x51000842>.
- Daan Frenkel and Rob Eppenga. Monte Carlo study of the isotropic-nematic transition in a fluid of thin hard disks. *Physical Review Letters*, 49(15):1089–1092, oct 1982. URL <http://doi.org/10.1103/physrevlett.49.1089>.
- Éric Freyssingeas, Didier Roux, and Frédéric Nallet. Quasi-elastic light scattering study of highly swollen lamellar and “sponge” phases. *Journal de Physique II*, 7(6):913–929, jun 1997. URL <http://doi.org/10.1051/jp2:1997162>.
- Rickard Frost, Gustav Edman Jönsson, Dinko Chakarov, Sofia Svedhem, and Bengt Kasemo. Graphene oxide and lipid membranes: Interactions and nanocomposite structures. *Nano Letters*, 12(7):3356–3362, jun 2012. URL <http://doi.org/10.1021/nl203107k>.
- Jean-Christophe P. Gabriel, Franck Camerel, Bruno J. Lemaire, Hervé Desvaux, Patrick Davidson, and Patrick Batail. Swollen liquid-crystalline lamellar phase based on extended solid-like sheets. *Nature*, 413:504–508, 2001. URL <https://doi.org/10.1038/35097046>.
- Wei Gao, Lawrence B. Alemany, Lijie Ci, and Pulickel M. Ajayan. New insights into the structure and reduction of graphite oxide. *Nature Chemistry*, 1(5):403–408, jul 2009. URL <https://doi.org/10.1038/nchem.281>.
- A. K. Geim. Graphene: Status and prospects. *Science*, 324(5934):1530–1534, jun 2009. URL <https://doi.org/10.1126/science.1158877>.

- A. K. Geim and K. S. Novoselov. The rise of graphene. *Nature Materials*, 6(3):183–191, mar 2007. URL <https://doi.org/10.1038/nmat1849>.
- Fengxia Geng, Renzhi Ma, Akira Nakamura, Kosho Akatsuka, Yasuo Ebina, Yusuke Yamauchi, Nobuyoshi Miyamoto, Yoshitaka Tateyama, and Takayoshi Sasaki. Unusually stable  $\sim 100$ -fold reversible and instantaneous swelling of inorganic layered materials. *Nature Communications*, 4:1632, mar 2013. URL <https://doi.org/10.1038/ncomms2641>.
- Barbara B. Gerbelli, Rafael L. Rubim, Emerson R. Silva, Frédéric Nallet, Laurence Navailles, Cristiano L. P. Oliveira, and Elisabeth A. de Oliveira. Steric-induced effects on stabilizing a lamellar structure. *Langmuir*, 29(45):13717–13722, nov 2013. URL <https://doi.org/10.1021/la402962c>.
- Otto Glatter and Otto Kratky. *Small Angle X-Ray Scattering*. Academic Pr, 1982. ISBN 0122862805.
- Graphenea. Product Datasheet: Graphene Oxide, 2014. Accessed: 2018-04-16. URL [https://cdn.shopify.com/s/files/1/0191/2296/files/Graphenea\\_GO\\_Datasheet\\_2014-03-25.pdf](https://cdn.shopify.com/s/files/1/0191/2296/files/Graphenea_GO_Datasheet_2014-03-25.pdf).
- Mohsen Moazzami Gudarzi. Colloidal stability of graphene oxide: Aggregation in two dimensions. *Langmuir*, 32(20):5058–5068, may 2016. URL <https://doi.org/10.1021/acs.langmuir.6b01012>.
- Leon Gunther, Yoseph Imry, and Joseph Lajzerowicz. X-ray scattering in smectic-A liquid crystals. *Physical Review A*, 22(4):1733–1740, oct 1980. URL <https://doi.org/10.1103/physreva.22.1733>.
- Fei Guo, Franklin Kim, Tae Hee Han, Vivek B. Shenoy, Jiaying Huang, and Robert H. Hurt. Hydration-responsive folding and unfolding in graphene oxide liquid crystal phases. *ACS Nano*, 5(10):8019–8025, septembre 2011. URL <https://doi.org/10.1021/nn2025644>.
- Heon Ham, Tran Van Khai, No-Hyung Park, Dae Sup So, Joon-Woo Lee, Han Gil Na, Yong Jung Kwon, Hong Yeon Cho, and Hyoun Woo Kim. Freeze-drying-induced changes in the properties of graphene oxides. *Nanotechnology*, 25(23):1–8, june 2014. URL <https://doi.org/10.1088/0957-4484/25/23/235601>.
- Norman Holt Hartshorne. *The Microscopy of Liquid Crystals*. Monographs in microscope series. Microscope Publications, 1974. ISBN 0904962032.
- W. Helfrich. Steric interaction of fluid membranes in multilayer systems. *Zeitschrift für Naturforschung A*, 33(3), jan 1978. URL <https://doi.org/10.1515/zna-1978-0308>.

- T. C. Huang, H. Toraya, T. N. Blanton, and Y. Wu. X-ray powder diffraction analysis of silver behenate, a possible low-angle diffraction standard. *Journal of Applied Crystallography*, 26(2):180–184, apr 1993. URL <https://doi.org/10.1107/s0021889892009762>.
- A. W. Hull. A new method of x-ray crystal analysis. *Physical Review*, 10(6):661–696, dec 1917. URL <https://doi.org/10.1103/physrev.10.661>.
- William S. Hummers and Richard E. Offeman. Preparation of graphitic oxide. *Journal of the American Chemical Society*, 80(6):1339–1339, 1958. URL <http://doi.org/10.1021/ja01539a017>.
- Seung Hun. Thermal reduction of graphene oxide. In *Physics and Applications of Graphene - Experiments*. InTech, apr 2011. URL <http://doi.org/10.5772/14156>.
- John D. Hunter. Matplotlib: A 2d graphics environment. *Computing in Science & Engineering*, 9(3):90–95, 2007. URL <http://doi.org/10.1109/MCSE.2007.55>.
- Jacob N. Israelachvili. *Intermolecular and Surface Forces*. Academic Press, 2015. ISBN 978-0-12-375182-9.
- Masateru M. M. Ito, Kohzo Ito, Mitsuhiro Shibayama, Kenji Sugiyama, and Hideaki Yokoyama. Phase behavior of block copolymers in selective supercritical solvent. *Macromolecules*, 48(11):3590–3597, may 2015. URL <http://doi.org/10.1021/acs.macromol.5b00162>.
- Rouhollah Jalili, Seyed Hamed Aboutalebi, Dorna Esrafilzadeh, Konstantin Konstantinov, Simon E. Moulton, Joselito M. Razal, and Gordon G. Wallace. Organic solvent-based graphene oxide liquid crystals: A facile route toward the next generation of self-assembled layer-by-layer multifunctional 3D architectures. *ACS Nano*, 7(5):3981–3990, 2013. URL <http://doi.org/10.1021/nn305906z>.
- Eric Jones, Travis Oliphant, Pearu Peterson, et al. SciPy: Open source scientific tools for Python, 2001. Accessed: 2018-08-29. URL <http://www.scipy.org/>.
- Richard A. L. Jones. *Soft Condensed Matter (Oxford Master Series in Condensed Matter Physics, Vol. 6)*. Oxford University Press, 2002. ISBN 0198505892.
- Hans Kelker and Rolf Hatz. *Handbook of Liquid Crystals*. Wiley-VCH Verlag GmbH, 1980. ISBN 3-527-25481-1.
- Brian Kelly. *Physics of Graphite*. Springer, 1981. ISBN 0853349606.
- Jaemyung Kim, Laura J. Cote, and Jiaying Huang. Two dimensional soft material: New faces of graphene oxide. *Accounts of Chemical Research*, 45(8):1356–1364, june 2012. URL <http://doi.org/10.1021/ar300047s>.

- Ji Eun Kim, Dr. Tae Hee Han, Dr. Sun Hwa Lee, Ju Young Kim, Dr. Chi Won Ahn, Dr. Je Moon Yun, and Prof. Sang Ouk Kim. Graphene oxide liquid crystals. *Angewandte Chemie International Edition*, 50(13):3043–3047, march 2011. URL <https://doi.org/10.1002/anie.201004692>.
- Dzina Kleshchanok, Peter Holmqvist, Janne-Mieke Meijer, and Henk N. W. Lekkerkerker. Lyotropic smectic B phase formed in suspensions of charged colloidal platelets. *Journal of the American Chemical Society*, 134(13):5985–5990, mar 2012. URL <https://doi.org/10.1021/ja300527w>.
- Bharathi Konkena and Sukumaran Vasudevan. Glass, gel, and liquid crystals: Arrested states of graphene oxide aqueous dispersions. *The Journal of Physical Chemistry C*, 118(37):21706–21713, august 2014. URL <https://doi.org/10.1021/jp507266t>.
- Otto Kratky and Gunther Porod. Diffuse small-angle scattering of x-rays in colloid systems. *Journal of Colloid Science*, 4(1):35–70, 1949. URL [http://doi.org/10.1016/0095-8522\(49\)90032-X](http://doi.org/10.1016/0095-8522(49)90032-X).
- F. V. Kusmartsev, W. M. Wu, M. P. Pierpoint, and K. C. Yung. Application of graphene within optoelectronic devices and transistors. In *Progress in Optical Science and Photonics*, pages 191–221. Springer Singapore, oct 2014. URL [https://doi.org/10.1007/978-981-287-242-5\\_9](https://doi.org/10.1007/978-981-287-242-5_9).
- Lev Davidovich Landau. On the theory of phase transitions. *Zh. Eksp. Teor. Fiz.*, 7: 19–32, 1937. Translated and reprinted at Ukr. J. Phys. 2008, Vol. 53, Special Issue, p.25-35. URL <http://archive.ujp.bitp.kiev.ua/files/journals/53/si/53SI08p.pdf>.
- F. C. Larche, J. Appell, G. Porte, P. Bassereau, and J. Marignan. Extreme swelling of a lyotropic lamellar liquid crystal. *Physical Review Letters*, 56(16):1700–1703, apr 1986. URL <https://doi.org/10.1103/physrevlett.56.1700>.
- A. Lerf, A. Buchsteiner, J. Pieper, S. Schöttl, I. Dekany, T. Szabo, and H.P. Boehm. Hydration behavior and dynamics of water molecules in graphite oxide. *Journal of Physics and Chemistry of Solids*, 67(5-6):1106–1110, may 2006. URL <https://doi.org/10.1016/j.jpcs.2006.01.031>.
- Lionel Liebert, editor. *Liquid Crystals*, volume 14 of *Solid State Physics Supplements*. Academic Press Inc, 1978. ISBN 0-12-607774-6.
- Peter Lindner and Thomas Zemb, editors. *Neutron, X-rays and Light. Scattering Methods Applied to Soft Condensed Matter (North-Holland Delta Series)*. North Holland, 2002. ISBN 0444511229.

- Reinhard Lipowsky and Stanislas Leibler. Unbinding transitions of interacting membranes. *Physical Review Letters*, 56(23):2541–2544, jun 1986. URL <https://doi.org/10.1103/physrevlett.56.2541>.
- V. Luzzati and F. Husson. The structure of the liquid-crystalline phases of lipid-water systems. *The Journal of Cell Biology*, 12(2):207–219, feb 1962. ISSN 0021-9525. URL <http://doi.org/10.1083/jcb.12.2.207>.
- Massimo Marcaccio and Francesco Paolucci, editors. *Making and Exploiting Fullerenes, Graphene, and Carbon Nanotubes*. Springer Berlin Heidelberg, 2014. URL <https://doi.org/10.1007/978-3-642-55083-6>.
- Daniela C. Marcano, Dmitry V. Kosynkin, Jacob M. Berlin, Alexander Sinitskii, Zhengzong Sun, Alexander Slesarev, Lawrence B. Alemany, Wei Lu, and James M. Tour. Improved synthesis of graphene oxide. *ACS Nano*, 4(8):4806–4814, jul 2010. URL <https://doi.org/10.1021/nn1006368>.
- Nikhil V. Medhekar, Ashwin Ramasubramaniam, Rodney S. Ruoff, and Vivek B. Shenoy. Hydrogen bond networks in graphene oxide composite paper: Structure and mechanical properties. *ACS Nano*, 4(4):2300–2306, apr 2010. URL <https://doi.org/10.1021/nn901934u>.
- N. D. Mermin. Crystalline order in two dimensions. *Physical Review*, 176(1):250–254, dec 1968. URL <https://doi.org/10.1103/physrev.176.250>.
- Laurent J. Michot, Isabelle Bihannic, Solange Maddi, Sérgio S. Funari, Christophe Baravian, Pierre Levitz, and Patrick Davidson. Liquid-crystalline aqueous clay suspensions. *Proceedings of the National Academy of Sciences*, 103:16101–16104, 2006. URL <https://doi.org/10.1073/pnas.0605201103>.
- S. T. Milner and D. Roux. Flory theory of the unbinding transition. *Journal de Physique I*, 2(9):1741–1754, sep 1992. URL <https://doi.org/10.1051/jp1:1992108>.
- Velram Balaji Mohan, Kin tak Lau, David Hui, and Debes Bhattacharyya. Graphene-based materials and their composites: A review on production, applications and product limitations. *Composites Part B: Engineering*, 142:200–220, jun 2018. URL <https://doi.org/10.1016/j.compositesb.2018.01.013>.
- Drew Myers. *Surfaces, Interfaces, and Colloids: Principles and Applications, 2nd Edition*. Wiley-VCH, 1999. ISBN 0471330604.
- Frédéric Nallet. Introduction à la diffusion aux petits angles. *École thématique de la Société Française de la Neutronique*, 11:17–42, 2010. URL <https://doi.org/10.1051/sfn/201011003>.

- Frédéric Nallet. Surfactant films in lyotropic lamellar (and related) phases: Fluctuations and interactions. *Advances in Colloid and Interface Science*, 247:363–373, sep 2017. URL <https://doi.org/10.1016/j.cis.2017.06.009>.
- Frédéric Nallet, René Laversanne, and Didier Roux. Modelling x-ray or neutron scattering spectra of lyotropic lamellar phases: Interplay between form and structure factors. *Journal de Physique II*, 3(4):487–502, 1993. URL <http://doi.org/10.1051/jp2:1993146>.
- Miloslav Nič, Jiří Jirát, Bedřich Košata, Aubrey Jenkins, and Alan McNaught, editors. *IUPAC Compendium of Chemical Terminology*. IUPAC, jun 2009. URL <https://doi.org/10.1351/goldbook>.
- B.W. Ninham. On progress in forces since the DLVO theory. *Advances in Colloid and Interface Science*, 83(1-3):1–17, dec 1999. URL [https://doi.org/10.1016/s0001-8686\(99\)00008-1](https://doi.org/10.1016/s0001-8686(99)00008-1).
- Massimo G. Noro and William M. Gelbart. Theory of lamellar–lamellar phase transitions in pure and mixed surfactant solutions. *The Journal of Chemical Physics*, 111(8): 3733–3743, aug 1999. URL <https://doi.org/10.1063/1.479654>.
- K. S. Novoselov, A. K. Geim, S. V. Morozov, D. Jiang, Y. Zhang, S. V. Dubonos, I. V. Grigorieva, and A. A. Firsov. Electric field effect in atomically thin carbon films. *Science*, 306(5696):666–669, 2004. ISSN 0036-8075. URL <https://doi.org/10.1126/science.1102896>.
- Cristiano Luis Pinto Oliveira and Jan Pedersen. Supersaxs package. Unpublished.
- Lars Onsager. The effect of shape on the interaction of colloidal particles. *Annals of the New York Academy of Sciences*, 51:627–659, May 1949. URL <https://doi.org/10.1111/j.1749-6632.1949.tb27296.x>.
- Doris Orthaber, Alexander Bergmann, and Otto Glatter. SAXS experiments on absolute scale with Kratky systems using water as a secondary standard. *Journal of Applied Crystallography*, 33(2):218–225, apr 2000. URL <https://doi.org/10.1107/s0021889899015216>.
- Jae Hyun Park and N.R. Aluru. Self-assembly of graphenes. *Surface Science*, 605(17-18): 1616–1620, sep 2011. URL <https://doi.org/10.1016/j.susc.2011.02.011>.
- Songfeng Pei and Hui-Ming Cheng. The reduction of graphene oxide. *Carbon*, 50(9): 3210–3228, aug 2012. URL <https://doi.org/10.1016/j.carbon.2011.11.010>.
- Philippe Poulin, Rouhollah Jalili, Wilfrid Neri, Frédéric Nallet, Thibaut Divoux, Annie Colin, Seyed Hamed Aboutalebi, Gordon Wallace, and Cécile Zakri. Superflexibility of graphene oxide. *Proceedings of the National Academy of Sciences*, 2016. URL <https://doi.org/10.1073/pnas.1605121113>.

- Oleg V. Prezhdov. Graphene — the ultimate surface material. *Surface Science*, 605(17-18): 1607–1610, sep 2011. URL <https://doi.org/10.1016/j.susc.2011.05.009>.
- Ling Qiu, Jeffery Z. Liu, Shery L.Y. Chang, Yanzhe Wu, and Dan Li. Biomimetic superelastic graphene-based cellular monoliths. *Nature Communications*, 3(1), jan 2012. URL <https://doi.org/10.1038/ncomms2251>.
- Ludwig Reimer and Helmut Kohl. *Transmission Electron Microscopy*, volume 36 of *Springer Series in Optical Sciences*. Springer-Verlag GmbH, 5 edition, 2008. ISBN 0387400931.
- B. Rezania, Nikolai Severin, Alexandr V. Talyzin, and Jürgen P. Rabe. Hydration of bilayered graphene oxide. *Nano Letters*, 14(7):3993–3998, jun 2014. URL <https://doi.org/10.1021/nl5013689>.
- Stéphan Rouzière, J. David Núñez, Erwan Paineau, Ana M. Benito, Wolfgang K. Maser, and Pascale Launois. Intercalated water in multi-layered graphene oxide paper: an x-ray scattering study. *Journal of Applied Crystallography*, 50(3):876–884, may 2017. URL <https://doi.org/10.1107/s1600576717006227>.
- R. Leite Rubim, B. B. Gerbelli, K. Bougis, C. L. Pinto de Oliveira, L. Navailles, F. Nallet, and E. Andreoli de Oliveira. Water activity in lamellar stacks of lipid bilayers: “hydration forces” revisited. *The European Physical Journal E*, 39(1), jan 2016. URL <https://doi.org/10.1140/epje/i2016-16003-0>.
- Rafael Leite Rubim. Study of interactions between lipid membranes by SAXS experiments: the role of the composition. Master’s thesis, 2014. URL <https://doi.org/10.11606/D.43.2014.tde-27112014-121446>.
- Rafael Leite Rubim, Margarida Abrantes Barros, Thomas Missègue, Kévin Bougis, Laurence Navailles, and Frédéric Nallet. Highly confined stacks of graphene oxide sheets in water. *The European Physical Journal E*, 41(3), mar 2018. URL <https://doi.org/10.1140/epje/i2018-11636-5>.
- Eli Ruckenstein and Marian Manciu. On the stability of lyotropic lamellar liquid crystals and the thicknesses of their lamellae. *Langmuir*, 17(18):5464–5475, sep 2001. URL <https://doi.org/10.1021/la010385e>.
- C. R. Safinya, D. Roux, G. S. Smith, S. K. Sinha, P. Dimon, N. A. Clark, and A. M. Bellocq. Steric interactions in a model multimembrane system: A synchrotron x-ray study. *Physical Review Letters*, 57(21):2718–2721, nov 1986. URL <https://doi.org/10.1103/physrevlett.57.2718>.

- Hannes C. Schniepp, Je-Luen Li, Michael J. McAllister, Hiroaki Sai, Margarita Herrera-Alonso, Douglas H. Adamson, Robert K. Prud'homme, Roberto Car, Dudley A. Saville, and Ilhan A. Aksay. Functionalized single graphene sheets derived from splitting graphite oxide. *The Journal of Physical Chemistry B*, 110(17):8535–8539, may 2006. URL <https://doi.org/10.1021/jp060936f>.
- W. Scholz and H. P. Boehm. Untersuchungen am graphitoxid. VI. betrachtungen zur struktur des graphitoxids. *Zeitschrift für anorganische und allgemeine Chemie*, 369(3-6):327–340, oct 1969. URL <https://doi.org/10.1002/zaac.19693690322>.
- Duncan Shaw. *Introduction to Colloid and Surface Chemistry, Fourth Edition (Colloid & Surface Engineering S)*. Butterworth-Heinemann, 1992. ISBN 0750611820.
- Mitsuhiro Shibayama and Takeji Hashimoto. Small-angle x-ray scattering analyses of lamellar microdomains based on a model of one-dimensional paracrystal with uniaxial orientation. *Macromolecules*, 19(3):740–749, may 1986. URL <http://doi.org/10.1021/ma00157a043>.
- Dinesh Pratap Singh, Carlos Eugenio Herrera, Brijesh Singh, Shipra Singh, Rajesh Kumar Singh, and Rajesh Kumar. Graphene oxide: An efficient material and recent approach for biotechnological and biomedical applications. *Materials Science and Engineering: C*, 86:173–197, may 2018. URL <http://doi.org/10.1016/j.msec.2018.01.004>.
- Konstantinos Spyrou and Petra Rudolf. An introduction to graphene. In Vasilios Georgakilas, editor, *Functionalization of Graphene*, chapter 1, pages 1–20. Wiley-VCH Verlag GmbH & Co. KGaA., 2014. URL <http://doi.org/10.1002/9783527672790.ch1>.
- Sasha Stankovich, Dmitriy A. Dikin, Geoffrey H. B. Dommett, Kevin M. Kohlhaas, Eric J. Zimney, Eric A. Stach, Richard D. Piner, SonBinh T. Nguyen, and Rodney S. Ruoff. Graphene-based composite materials. *Nature*, 442(7100):282–286, jul 2006a. URL <http://doi.org/10.1038/nature04969>.
- Sasha Stankovich, Richard D. Piner, SonBinh T. Nguyen, and Rodney S. Ruoff. Synthesis and exfoliation of isocyanate-treated graphene oxide nanoplatelets. *Carbon*, 44(15):3342–3347, dec 2006b. URL <http://doi.org/10.1016/j.carbon.2006.06.004>.
- Sasha Stankovich, Dmitriy A. Dikin, Richard D. Piner, Kevin A. Kohlhaas, Alfred Kleinhammes, Yuanyuan Jia, Yue Wu, SonBinh T. Nguyen, and Rodney S. Ruoff. Synthesis of graphene-based nanosheets via chemical reduction of exfoliated graphite oxide. *Carbon*, 45(7):1558–1565, june 2007. URL <https://doi.org/10.1016/j.carbon.2007.02.034>.
- Reinhard Strey, Reinhard Schomäcker, Didier Roux, Frederic Nallet, and Ulf Olsson. Dilute lamellar and L<sub>3</sub> phases in the binary water–C<sub>12</sub>E<sub>5</sub> system. *J. Chem. Soc., Faraday Trans.*, 86(12):2253–2261, 1990. URL <http://doi.org/10.1039/ft9908602253>.

- Pengzhan Sun, Yanlei Wang, He Liu, Kunlin Wang, Dehai Wu, Zhiping Xu, and Hongwei Zhu. Structure evolution of graphene oxide during thermally driven phase transformation: Is the oxygen content really preserved? *PLoS ONE*, 9(11):1–8, november 2014. URL <https://doi.org/10.1371/journal.pone.0111908>.
- Rachel Tkacz, Rudolf Oldenbourg, Shalin B. Mehta, Morteza Miansari, Amitabh Verma, and Mainak Majumder. pH dependent isotropic to nematic phase transitions in graphene oxide dispersions reveal droplet liquid crystalline phases. *Chemical Communications*, 50(50):6668–6671, may 2014. URL <https://doi.org/10.1039/C4CC00970C>.
- Liping Tong, Wei Qi, Mengfan Wang, Renliang Huang, Rongxin Sua, and Zhimin Hea. Long-range ordered graphite oxide liquid crystals. *Chemical Communications*, 50(58):7776–7779, april 2014. URL <https://doi.org/10.1039/C4CC01347F>.
- Yoshiaki Uchida, Takuma Nishizawa, Takeru Omiya, Yuichiro Hirota, and Norikazu Nishiyama. Nanosheet formation in hyperswollen lyotropic lamellar phases. *Journal of the American Chemical Society*, 138(4):1103–1105, jan 2016. URL <http://doi.org/10.1021/jacs.5b11256>.
- Felix M. van der Kooij and Henk N. W. Lekkerkerker. Formation of nematic liquid crystals in suspensions of hard colloidal platelets. *The Journal of Physical Chemistry B*, 102(40):7829–7832, 1998. URL <http://doi.org/10.1021/jp981534d>.
- P. R. Wallace. The band theory of graphite. *Physical Review*, 71(9):622–634, may 1947. URL <http://doi.org/10.1103/physrev.71.622>.
- Guoxiu Wang, Juan Yang, Jinsoo Park, Xinglong Gou, Bei Wang, Hao Liu, and Jane Yao. Facile synthesis and characterization of graphene nanosheets. *The Journal of Physical Chemistry C*, 112(22):8192–8195, 2008. URL <http://doi.org/10.1021/jp710931h>.
- Lin Wang, Xia Xin, Mengzhou Yang, Xin Ma, Zhenyu Feng, Rui Chen, Jinglin Shen, and Shiling Yuan. Comparative study of n-dodecyl tetraethylene monoether lyotropic liquid crystals incorporated with graphene and graphene oxide. *Phys. Chem. Chem. Phys.*, 16:20932–20940, 2014. URL <http://doi.org/10.1039/C4CP02634A>.
- Lin Wang, Xia Xin, Mengzhou Yang, Jinglin Shen, and Shiling Yuan. Incorporation of graphene oxide into C<sub>12</sub>E<sub>4</sub>/C<sub>12</sub>mimBr hybrid lyotropic liquid crystal and its thermosensitive properties. *RSC Adv.*, 5:68404–68412, 2015. URL <http://doi.org/10.1039/C5RA13497H>.
- Zhen Xu and Chao Gao. Aqueous liquid crystals of graphene oxide. *ACS Nano*, 5(4):2908–2915, march 2011a. URL <http://doi.org/10.1021/nn200069w>.

- Zhen Xu and Chao Gao. Graphene chiral liquid crystals and macroscopic assembled fibres. *Nature Communications*, 2(571):1–13, december 2011b. URL <http://doi.org/10.1038/ncomms1583>.
- Zhen Xu and Chao Gao. Graphene in macroscopic order: Liquid crystals and wet-spun fibers. *Accounts of Chemical Research*, 47(4):1267–1276, february 2014. URL <http://doi.org/10.1021/ar4002813>.
- Zhen Xu, Haiyan Sun, Xiaoli Zhao, and Chao Gao. Ultrastrong fibers assembled from giant graphene oxide sheets. *Advanced Materials*, 25(2):188–193, january 2013. URL <https://doi.org/10.1002/adma.201203448>.
- Xiaoming Yang, Chengxin Guo, Liangliang Ji, Yaowen Li, and Yingfeng Tu. Liquid crystalline and shear-induced properties of an aqueous solution of graphene oxide sheets. *Langmuir*, 29(25):8103–8107, may 2013. URL <http://doi.org/10.1021/la401038c>.
- Cécile Zakri, Christophe Blanc, Eric Grelet, Camilo Zamora-Ledezma, Nicolas Puech, Eric Anglaret, and Philippe Poulin. Liquid crystals of carbon nanotubes and graphene. *Philosophical Transactions A*, 371(1988), march 2013. URL <http://doi.org/10.1098/rsta.2012.0499>.
- Camilo Zamora-Ledezma, Nicolas Puech, Cécile Zakri, Eric Grelet, Simon E. Moulton, Gordon G. Wallace, Sanjeev Gambhir, Christophe Blanc, Eric Anglaret, and Philippe Poulin. Liquid crystallinity and dimensions of surfactant-stabilized sheets of reduced graphene oxide. *The Journal of Physical Chemistry Letters*, 3(17):2425–2430, 2012. URL <http://doi.org/10.1021/jz3008479>.
- Jianmin Zhang, Yumei Ren, Tao Xu, Hongxia Yang, and Qun Xu. Liquid crystal graphene oxide with different layers: fabrication, characterization and applications. *RSC Advances*, 5(115):94809–94813, 2015. URL <http://doi.org/10.1039/c5ra16539c>.
- Ruitian Zhang, Robert M. Suter, and John F. Nagle. Theory of the structure factor of lipid bilayers. *Physical Review E*, 50(6):5047–5060, dec 1994. URL <http://doi.org/10.1103/physreve.50.5047>.
- Ming Zhou, Yuling Wang, Yueming Zhai, Junfeng Zhai, Wen Ren, Fuan Wang, and Shaojun Dong. Controlled synthesis of large-area and patterned electrochemically reduced graphene oxide films. *Chemistry - A European Journal*, 15(25):6116–6120, jun 2009. URL <http://doi.org/10.1002/chem.200900596>.
- Xiaoyan Zhou, Bing Wang, Tu Lan, Hanqing Chen, Hailong Wang, Ye Tao, Zhihong Li, Kurash Ibrahim, Dongqi Wang, and Weiyue Feng. Chirality of graphene oxide–humic acid sandwich complex induced by a twisted, long-range-ordered nanostructure. *The Journal of Physical Chemistry C*, 120(45):25789–25795, nov 2016. URL <http://doi.org/10.1021/acs.jpcc.6b07582>.



# List of symbols and acronyms

$\eta$  Caillé parameter 57

$\psi$  Azimuthal angle 58

$\varrho$  Ratio between surfactant and GO volume fractions 68

$\varsigma$  Aspect ratio 22

$2\theta$  Scattering angle 28

**B** Compression modulus 57

**d** Lamellar periodicity 22, 25

**DLS** Dynamic Light Scattering 27

**GO** Graphene Oxide 20

**K** Splay modulus 57

**LC** Liquid crystal 21

**P(q)** Form factor 55

**POM** Polarized Optical Microscopy 27

**q** Scattering vector 28

**S(q)** Structure factor 57

**SAXS** Small Angle X-Ray Scattering 29

**TEM** Transmission Electron Microscopy 27

**WAXS** Wide Angle X-Ray Scattering 30



# List of Figures

2.1	Structural representation of carbon materials. . . . .	18
a	Graphite in perspective and top views. . . . .	18
b	Graphene and reduced Graphene Oxide. . . . .	18
c	Graphene Oxide. . . . .	18
2.2	Interlayer distance <i>vs.</i> water mass fraction. . . . .	19
2.3	Mass fraction of GO in water when the phase transitions are observed. . .	23
2.4	Lamellar periodicity <i>vs.</i> GO mass fraction. . . . .	23
2.5	Representation of an amphiphilic molecule. . . . .	24
2.6	Representation of a smectic A mesophase. . . . .	25
2.7	Structural formula of simulsol. . . . .	26
3.1	POM images of aqueous dispersions prepared with lyophilised GO. . . . .	34
a	Concentration of 4 mg/mL. . . . .	34
b	Concentration of 20 mg/mL. . . . .	34
3.2	POM images of commercial GO aqueous dispersions. . . . .	35
a	Direct observation. . . . .	35
b	Crossed polarizer and analyser. . . . .	35
3.3	TEM images of GO sheets. . . . .	35
a	Commercial dispersion diluted 50x. . . . .	35
b	Commercial dispersion diluted 75x. . . . .	35
3.4	Size distribution of GO layers. . . . .	36
3.5	DLS results for GO dispersions. . . . .	37
a	Correlation functions of a GO dispersion. . . . .	37
b	Characteristic relaxation frequency. . . . .	37
c	Exponent of the stretched exponential. . . . .	37
3.6	Evolution of the GO layers hydrodynamic radii. . . . .	38
3.7	POM images of a concentrated GO aqueous dispersion. . . . .	39
a	Direct observation. . . . .	39
b	Crossed polarizer and analyser. . . . .	39
3.8	Device to dehydrate aqueous GO dispersions. . . . .	40
3.9	GO mass fraction <i>vs.</i> dehydration time. . . . .	41
3.10	SAXS spectra of GO dispersions at same final concentration. . . . .	42

3.11 SAXS results of dehydrated GO dispersions. Data shifted vertically for a better visualisation. . . . .	44
a    Diffractogram of a dispersion with $f_m = 0.04$ . . . . .	44
b    Diffractogram of a dispersion with $f_m = 0.16$ . . . . .	44
c    Spectra in a smaller range of $q$ for GO dispersions. . . . .	44
d    Spectra in a larger range of $q$ for GO dispersions. . . . .	44
3.12 X-ray scattering spectrum of the driest GO dispersion. . . . .	45
3.13 X-ray spectrum of natural graphite. . . . .	46
3.14 Lamellar periodicity <i>vs.</i> inverse GO volume fraction. . . . .	47
3.15 Schematic representation of swelling of GO sheets lamellar structure. . . . .	47
3.16 SAXS spectra in the Kratky representation for GO dispersions. . . . .	49
a    GO mass fraction fixed to $f_m = 0.014$ varying salt concentration. . . . .	49
b    GO mass fraction fixed to $f_m = 0.043$ varying salt concentration. . . . .	49
3.17 POM images of GO dispersions with NaCl. . . . .	51
a $1 \times 10^{-2}$ M of NaCl in direct observation. . . . .	51
b $1 \times 10^{-2}$ M of NaCl in crossed polarization. . . . .	51
c $1 \times 10^{-1}$ M of NaCl in direct observation. . . . .	51
d $1 \times 10^{-1}$ M of NaCl in crossed polarization. . . . .	51
3.18 Lamellar periodicity <i>vs.</i> NaCl concentration. . . . .	51
4.1 Spectra obtained before and after the correction. . . . .	54
4.2 Schematic electron density profile of GO layers. . . . .	56
4.3 SAXS results of a GO dispersion with $f_m = 0.04$ . . . . .	59
a    Diffractogram of the sample. . . . .	59
b    Intensity <i>vs.</i> azimuthal angle. . . . .	59
c    Integration in the whole radial range. . . . .	59
4.4 SAXS spectra in absolute scale for GO dispersions. . . . .	60
4.5 SAXS spectrum and the respective fittings. . . . .	61
4.6 Parameters obtained from the fittings of the GO dispersions. . . . .	62
a    Thickness of the GO layers. . . . .	62
b    Number of correlated layers. . . . .	62
c    Caillé parameter. . . . .	62
4.7 Schematic representation of GO lamellar structure in water. . . . .	63
4.8 Compression modulus <i>vs.</i> lamellar periodicity. . . . .	64
5.1 SAXS spectra of surfactant in water. . . . .	66
5.2 POM images of surfactant aqueous dispersions. . . . .	66
a    Surfactant volume fraction of 0.70. . . . .	66
b    Surfactant volume fraction of 0.75. . . . .	66
5.3 Periodicity <i>vs.</i> inverse surfactant volume fraction. . . . .	67
5.4 Spectra of ternary samples with $\varrho = 5.7$ . . . . .	69

a	SAXS spectra varying the water content. . . . .	69
b	WAXS spectra varying the water content. . . . .	69
5.5	Spectra of ternary samples with $\varrho = 4.3$ . . . . .	70
a	SAXS spectra varying the water content. . . . .	70
b	WAXS spectra varying the water content. . . . .	70
5.6	Spectra of ternary samples with $\varrho = 2.9$ . . . . .	71
a	SAXS spectra varying the water content. . . . .	71
b	WAXS spectra varying the water content. . . . .	71
5.7	Evolution of SAXS spectra of a ternary sample in time. . . . .	73
5.8	SAXS spectra of GO sheets and surfactant. . . . .	74
5.9	WAXS spectrum of GO sheets and surfactant. . . . .	75
5.10	Comparison between the SAXS spectra. . . . .	76
5.11	Lamellar periodicity <i>vs</i> inverse of GO volume fraction. . . . .	76
5.12	Schematic representation of GO lamellar structure with surfactant. . . . .	77
5.13	POM images of ternary systems. . . . .	79
a	$\varrho = 0.75$ and $\varphi_{\text{water}} = 0.93$ . . . . .	79
b	$\varrho = 1.80$ and $\varphi_{\text{water}} = 0.83$ . . . . .	79
c	$\varrho = 4.3$ and $\varphi_{\text{water}} = 0.38$ . . . . .	79
d	$\varrho = 9.0$ and $\varphi_{\text{water}} = 0.61$ . . . . .	79
5.14	SAXS spectra of ternary samples with $\varrho = 1.8$ varying the water content. . . . .	80
5.15	SAXS spectra of ternary samples with $\varrho = 5.8$ varying the water content. . . . .	81
5.16	SAXS spectra of systems with constant surfactant content. . . . .	83
5.17	SAXS spectra of systems with constant water content. . . . .	84
5.18	Schematic representation of obtained ternary structures. . . . .	86
5.19	Dilution lines of the investigated systems. . . . .	88
a	Dilution lines of the ternary systems. . . . .	88
b	Dilution lines of the first phase. . . . .	88
c	Dilution lines of the biphasic systems. . . . .	88
d	Dilution lines of the second phase. . . . .	88
e	Dilution lines of the ternary and binary systems. . . . .	88
5.20	Ternary phase diagram. . . . .	89

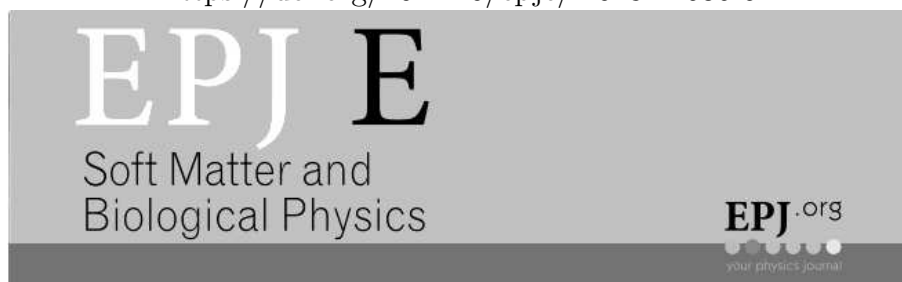


# Appendix A

## Published Article

The article already published in direct relation with the thesis project is reproduced below for convenience. Three other articles, not directly related to the thesis project but keys to many of its aspects, may be found in Refs. Gerbelli et al. (2013); Bougis et al. (2015); Rubim et al. (2016).

<https://doi.org/10.1140/epje/i2018-11636-5>



Eur. Phys. J. E (2018) **41**: 30

DOI 10.1140/epje/i2018-11636-5

### **Highly confined stacks of graphene oxide sheets in water**

Rafael Leite Rubim, Margarida Abrantes Barros, Thomas Missègue,  
Kévin Bougis, Laurence Navailles and Frédéric Nallet

# Highly Confined Stacks of Graphene Oxide Sheets in Water

Rafael Leite Rubim<sup>1</sup>, Margarida Abrantes Barros<sup>1,2</sup>, Thomas Missègue<sup>1</sup>, Kévin Bougis<sup>1a</sup>, Laurence Navailles<sup>1</sup>, and Frédéric Nallet<sup>1</sup>

<sup>1</sup> Université de Bordeaux, Centre de recherche Paul-Pascal–CNRS, 115 avenue du Docteur-Schweitzer, F-33600 Pessac, France

<sup>2</sup> Técnico Lisboa, Av. Rovisco Pais, 1, PT-1049-001 Lisboa, Portugal

Accepted for publication 2018-02-21

**Abstract** Since the discovery of graphene oxide (GO), the most accessible of the precursors of graphene, this material has been widely studied for applications in science and technology. In this work, we describe a procedure to obtain GO dispersions in water at high concentrations, these highly dehydrated dispersions being in addition fully redispersible by dilution. With the availability of such concentrated samples, it was possible to investigate the structure of hydrated GO sheets in a previously unexplored range of concentrations, and to evidence a structural phase transition. Tentatively applying models designed for describing the small-angle scattering curve in the Smectic A (or  $L_\alpha$ ) phase of lyotropic systems, it was possible to extract elastic parameters characterising the system on the dilute side of the transition, thereby evidencing the relevance of both electrostatic and steric (HELFRICH) interactions in stabilising aqueous lamellar stacks of GO sheets.

## 1 Introduction

Graphene oxide (GO) is a material obtained by mild oxidation and exfoliation of graphite, and one of the most common manner of preparing it is HUMMER’s modified method [1, 2]. This material is attracting a lot of interest, in particular because it can easily be dispersed in various solvents, including water, and many GO-based materials and composites have been developed by solution processing [3–8].

The structure of GO sheets, as well as their structural organisation in water have been investigated using various techniques, including atomic force microscopy (AFM), polarised optical microscopy (POM), circular dichroism (CD) and small-angle x-ray scattering (SAXS)—see for instance [4, 6, 9–14]. Most of these works—either directly (AFM) or indirectly (SAXS)—points to an atomic thickness  $t$  for the GO sheet, significantly below 1 nm (assuming for the GO density  $\rho_{GO}$  a value around 1.8 g/cm<sup>3</sup> in the SAXS-based method). Furthermore, it is now a consensus from POM and SAXS studies that the phase diagram of the lyotropic GO–water dispersion exhibits isotropic, nematic and lamellar (or lamellar-like) phases, phase transitions being driven by the increase of GO concentration in the dispersion, as also observed in somehow similar materials made of planar, solid-like sheets of near-atomic thickness [15, 16]—or a bit thicker [17].

In qualitative accordance with ONSAGER’s theory for the isotropic-to-nematic phase transition in suspensions of

*hard* colloids, quantitatively valid for slender particles [18], the particle volume fraction  $\varphi_I$  at the transition onset is given in numerical simulations for “pancake” particles by [19–21]

$$\varphi_I \approx 3.2 \frac{t}{L} \quad (1)$$

in terms of the particle aspect ratio  $L/t$ . Equation (1) describes reasonably well the *mass* fraction  $f_m^B$  of GO when birefringence first occurs (*viz.* when the nematic phase first appears) using  $f_m^B = \varphi_I \times \rho_{GO} / \rho_{H_2O}$ , considering the dispersity  $\mathfrak{D}$  in lateral extensions  $L$  [22, 23], as well as uncertainties in GO thickness  $t$  and density  $\rho_{GO}$ . Such an agreement is considered as a convincing argument for the GO sheets being *rigid* enough to remain essentially uncrumpled in dilute suspensions [4, 6].

Structures commonly described as *lamellar* are observed in more concentrated GO dispersions, as mainly results from SAXS studies [6, 9, 12, 24], a behaviour also found in similar (inorganic) materials such as phosphoantimonates, clays or titanium-iron acid oxides [15–17, 25]. The structure (sometimes depicted more cautiously as a nematic gel, a locally layered system, or a pseudo-smectic phase because compelling evidence for *positional* long-range order is not easily found) is formed by stacking GO sheets (or other kinds of solid-like sheets), separated by layers of water, with a given distance of repetition  $\ell$  of the unit cell along the stacking axis  $z$ . In the plane perpendicular to  $z$ , the structure of the two-dimensional solid-like sheet is well-defined locally, but more difficult to ascertain at scales larger than  $L$ . Owing to the repulsive interaction along  $z$  between two facing sheets, with a significant electrostatic contribution according to refs. [6, 15, 16], the

<sup>a</sup> *Present address:* Solvay–Laboratoire du futur, 178 avenue du Docteur-Schweitzer, F-33608 Pessac, France

Correspondence to: frederic.nallet@u-bordeaux.fr

thickness of the water layers increases, with therefore an increase in  $\ell$ , when (low ionic strength) water is added to the system. In a geometric description of the swelling process where  $L \rightarrow \infty$  and  $t$  is a constant, a simple dilution law, namely

$$\ell = t/\varphi \quad (2)$$

is expected and indeed observed, as in refs. [6, 12], at least for a restricted range of particle volume fractions  $\varphi$ , see [15, 16]. The dilution law, eq. (2), yields the above-mentioned SAXS (indirect) estimate for the GO sheet thickness  $t$ .

One of the purpose of the present contribution is to explore the validity of eq. (2) towards more *concentrated* GO dispersions than previously investigated. In the next sections, we describe how our samples are characterised using dynamic light (sect. 2.1) or small-angle x-ray (sect. 2.3) scattering techniques, and dehydrated in a controlled way to almost complete dryness while remaining fully redispersible in water (sect. 2.2). Our main results are summarised in sect. 3.1, with evidences for a structural phase transition between lamellar structures, not reported previously, as dehydration proceeds. In sect. 3.2, we discuss possible mechanisms stabilising in water the lamellar stacks of GO sheets, drawing an analogy with lamellar stacks of self-assembled amphiphilic bilayers. Though we give no clues as regards the most concentrated regime, the lamellar stack of GO sheets appears to be well described in the dilute regime by the so-called “unbinding transition” phenomenon that results from repulsive HELFRICH [26] and electrostatic interactions between stacked layers competing with attractive VAN DER WAALS interactions [27, 28].

## 2 Materials and methods

### 2.1 Sample characterisation

The graphene oxide suspensions are prepared from a commercial aqueous solution sold by Graphenea (San Sebastian, Spain), with nominal concentration 4 mg/mL. Such a solution is concentrated enough to be birefringent, as revealed by POM, but does not yet exhibit any significant increase in viscosity compared to water. According to the producer, the dispersion presents more than 95 % of carbon monolayers and an amount between 41 and 50% of oxygen atoms, with variable sheet dimensions  $L$  below 10  $\mu\text{m}$ , usually around 1–2  $\mu\text{m}$  [29]. Owing to the presence of COOH groups attached to the sheet surface, the aqueous GO suspensions are expected to be acid and, indeed, their measured  $\text{pH}$  is about 2.4. Two different batches were bought and used to prepare the samples. For both batches, dynamic light scattering (DLS) experiments were carried out, using a research goniometer and laser light scattering system from Brookhaven Instruments Corporation (Holtville, NY, USA). Freshly prepared samples were diluted in water to 0.04 mg/mL. At such a concentration, the samples are no longer birefringent but faint depolarised fluctuations can be observed by POM in an

optically thick (0.800 mm) cell from VitroCom (Mountain Lakes, NJ, USA). The DLS experiment is performed with incident light polarised perpendicular to the scattering plane, without analysing the polarisation of the scattered signal. DLS experiments have been repeated from time to time on ageing samples prepared with the first batch along a total period of about 2 months in an attempt to characterise ageing, if any. Some representative results on freshly prepared samples are shown in fig. 1. Fit-

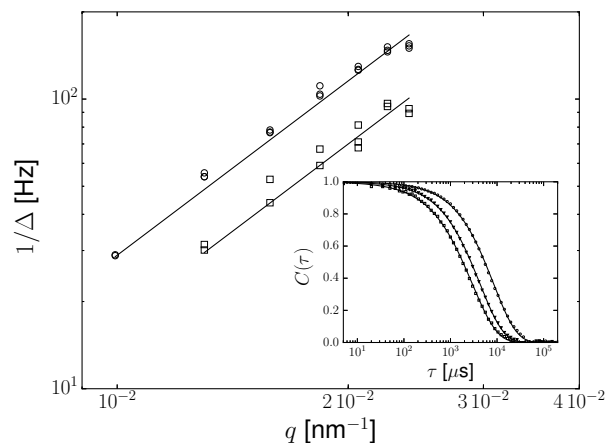


**Figure 1.** Characteristic relaxation frequency  $\Delta^{-1}$  of the autocorrelation function measured in DLS as a function of the scattering vector  $q$  for GO dispersions prepared from two separate batches—batch 1:  $\circ$ , batch 2:  $\square$ . Inset: Stretched-exponential model fitted to selected DLS data.

ting the DLS data to a stretched exponential model, see eq. 3, as a convenient (but *ad hoc*) way to somehow take into account the GO dispersity, two parameters (a characteristic time and a stretching exponent) were obtained as a function of the scattering wave vector  $q$ .

The model correlation function is expressed as

$$C(\tau) = \exp\left[-2\left(\frac{\tau}{\Delta}\right)^\beta\right] \quad (3)$$

where  $\Delta$  is the characteristic relaxation time and  $\beta$  the stretching exponent. Parameter  $\beta$  was found to decrease from *ca.* 0.9 to 0.7 as the scattering vector  $q$  increases from *ca.*  $1 \times 10^{-2}$  to  $2.2 \times 10^{-2}$   $\text{nm}^{-1}$ . Besides, as illustrated in fig. 1 by the straight lines with a slope 2, the relaxation frequency  $\Delta^{-1}$  is proportional to  $q^2$ , meaning that an *effective* diffusion coefficient—or a hydrodynamic radius  $R_H$ —can be defined. From the standard Stokes-Einstein relation

$$R_H = \frac{k_B T \Delta}{6\pi\eta} \times q^2 \quad (4)$$

with  $k_B$  the Boltzmann constant,  $T$  the absolute temperature of the GO dispersion and  $\eta$  the solvent viscosity, hydrodynamic radii were found equal to 0.74  $\mu\text{m}$  and 1.22  $\mu\text{m}$  for batches 1 and 2, respectively.

As mentioned above, possible effects of ageing were checked on samples prepared from the first batch, with three distinct histories:

1. Samples were diluted to the concentration appropriate for DLS (*ca.* 0.04 mg/mL) *immediately* after receiving the solution from Graphenea, then stored for ageing;
2. Samples were diluted to the concentration appropriate for DLS from the solution *stored for ageing* received from the manufacturer;
3. Samples *concentrated* to  $\approx 160$  mg/mL immediately after reception of the Graphenea solution (see below, sect. 2.2, for details regarding the concentration procedure) were stored for ageing, then diluted to the concentration appropriate for DLS.

Whatever the sample history, the storage conditions were the same, namely stable temperature (22°C) and no exposure to direct light. In all cases, DLS did not reveal any significant ageing over a period of about 2 months.

## 2.2 Sample preparation

A procedure to increase the concentration of the commercial GO dispersions was implemented, requiring two steps. Centrifugation and ultracentrifugation are used in the first step. The commercial dispersion is first centrifuged for about 20 min at 1400*g*, in order to remove “large” aggregates from the sample. After discarding the bottom phase, the supernatant is then ultracentrifuged at a much higher speed (302000*g*) for 5 h. The recovered supernatant, mostly water at *pH*=2.6, occupying almost the total volume of the centrifuge cell, is also discarded. The remaining phase appears as a highly viscous material with a dark, almost black colour. As explained below—see also fig. 2—, it turns out that the GO mass fraction  $f_m$  achieved at this stage is around 0.16, thus corresponding to an increase in GO concentration by a factor about 40. We have checked that increasing the duration of the ultracentrifugation procedure does not significantly increase  $f_m$ , while decreasing it below *ca.* 3 h does not lead to concentrated enough dispersions.

After a period of about one week left for homogenisation in a closed container—required because the presence of small and uncontrolled amounts of water at the surface of the concentrated dispersion cannot be avoided when recovering the pellet from the centrifuge cell—the second step begins. A home-designed device is set up to *slowly* evaporate at room temperature the aqueous solvent from samples. It consists in a diaphragm pump connected to a desiccator where a dozen of (open) Eppendorfs containing the desired material are stored, with a pressure control system maintaining 300 mbar inside the vacuum chamber.

Figure 2 shows the evolution in time of the GO mass fraction for three dispersions resulting from the first, centrifugation-based step. As it appeared retrospectively, they differed by their *initial* mass fractions. The mass fraction  $f_m(\tau)$  ( $\tau = 0$  when dehydration begins in the vacuum chamber) is determined, indeed, by weighing the sample at time  $\tau$ , which obviously requires *opening* the vacuum chamber. The measured mass is  $m(\tau)$ . The clock is

stopped (and the Eppendorfs closed) for the duration  $\delta$  of the weighing operations, with an optional (mild) shaking intended to re-homogenise samples visually displaying drier patches. The same procedure is repeated at regular intervals of, typically, 1 h (in “vacuum times”, *i.e.* subtracting the  $\delta$ ’s from the actually elapsed time). It has been observed that for  $\tau \gtrsim 30$  h the mass  $m(\tau)$  does not decrease any more, and keeps a constant value  $m_\infty$ . We have checked on a few sacrificial samples, submitted to a somehow stronger vacuum (pressure in the mbar range) for about 15 h, that remaining water cannot be extracted with our set-up: Achieving complete dehydration would require ultra-vacuum or elevated temperatures [30–32]. On the basis of our x-ray measurements (see below, Section 3.1), we estimate the weight fraction of “bound” water from Ref. [30] to be  $f_w^\infty \approx 27.7\%$ , with therefore  $f_m(\tau) = (1 - f_w^\infty) \times m_\infty / m(\tau)$ .

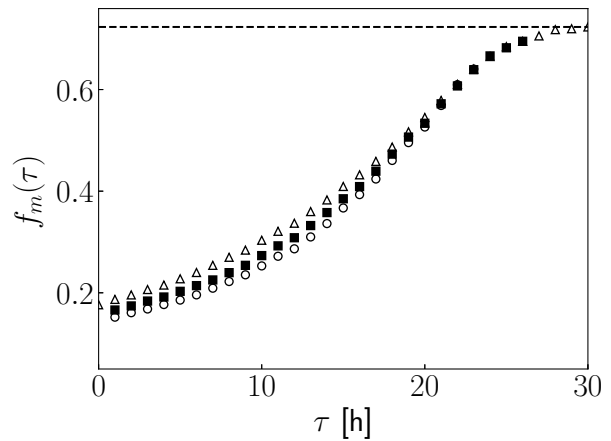


**Figure 2.** GO mass fractions  $f_m(\tau)$  as a function of the dehydration time in the vacuum chamber ( $p = 300$  mbar) for three samples differing by their *initial* water content:  $\circ$  14.4 %,  $\blacksquare$  15.7 %,  $\triangle$  17.6 %. The horizontal dashed line at  $f_m = 0.723$  corresponds to the limiting GO mass fraction, and accounts for water molecules that cannot be removed with our drying set-up.

Notably—and similarly to the first step—, the second step of the dehydration procedure is *reversible*. As shown by SAXS (see below, sect. 3), adding water to a sample extracted at time  $\tau_>$  from the desiccator in the required amounts to mimic the composition of a sample stored for a lesser time  $\tau_<$  leads to essentially identical diffractograms for the “wet” and “dried-rehydrated” samples when they both originate from the same centrifuged material. At contrast with what has been observed with, *e.g.*, freeze-dried GO dispersions where the GO chemical structure is strongly affected [33], it seems to be preserved in our case as no aggregates were found in the slowly dried samples redispersed in water.

### 2.3 Experimental techniques

Samples removed at time  $\tau$  from the desiccator were left for at least a week in their (now closed) preparation Ependorfs to ensure relaxation of possible humidity gradients. After homogenisation, the samples were analysed by POM. Due to their extreme opacity when  $f_m$  exceeds 50%, highly dehydrated samples could not be successfully observed. For samples with smaller mass fractions, images were recorded (data not shown) using an Olympus BX 51 microscope with crossed polarisers and a  $\times 20$  objective. The samples were sandwiched between a glass slide and a cover-slip, without special precautions for ensuring a constant optical path, estimated below  $10\ \mu\text{m}$ , but preventing water evaporation by means of a UV-curing glue. Birefringence was always observed, indicating a liquid-crystalline organisation. The samples were homogeneous, as revealed by observing them without the analyser, indicating that aggregates were not present. The samples were also investigated by small angle x-ray scattering. The thick pastes were spread on a circular (diameter  $1.3\ \text{mm}$ ), machine-drilled opening perpendicular to the long axis of cylindrical stainless steel supports ( $2.0 \times 20.0\ \text{mm}$ ) which were then introduced in quartz capillaries with a nominal diameter of  $2.5\ \text{mm}$ . The spreading procedure did not allow a control of the optical path better than  $\approx 25\ \%$ . The quartz capillaries were further flame-sealed, to ensure tightness. Diffractograms were recorded on a Bruker-AXS Nanostar machine equipped with a Hi-Star detector, also from Bruker (Karlsruhe, Germany). From the entrance pinhole to the beryllium window in front of the detector, the whole flight path is evacuated. A crossed-coupled pair of Göbel mirrors (Bruker) selects the  $\lambda = 1.5418\ \text{\AA}$  radiation of a copper source (Siemens), operated at  $40\ \text{kV}$  and  $35\ \text{mA}$ . A 3-pin-hole system is used for collimating the incident beam, with a size (FWHM) at sample position *ca.*  $0.43\ \text{mm}$  in both vertical and horizontal directions. Two sample-to-detector distances, found close to  $0.25\ \text{m}$  and  $1.05\ \text{m}$  respectively, calibrated using silver behenate as standard [34], were used to match the variable stacking periods of the samples. From the Gaussian width of the first order Bragg peak of silver behenate, we estimate a resolution width (FWHM)  $\Delta q \approx 5 \times 10^{-2}\ \text{\AA}^{-1}$  or  $\Delta q \approx 6.0 \times 10^{-3}\ \text{\AA}^{-1}$  for the two configurations, respectively. Owing to the intrinsic broadening of silver behenate [34], the latter value could be slightly over-estimated. The scattering wave vectors that are practically accessible after subtracting the signal of a reference (water) capillary range from  $0.04\ \text{\AA}^{-1}$  to  $0.8\ \text{\AA}^{-1}$  in the “large-angle” configuration, and from  $0.01\ \text{\AA}^{-1}$  to  $0.2\ \text{\AA}^{-1}$  in the “small-angle” one. For accessing to even higher scattering wave vector values (typically  $0.5\text{--}3.3\ \text{\AA}^{-1}$ ), as required to assess the *in-plane* order of the GO sheets, we use a custom-made instrument with a copper rotating-anode-based setup and crossed-coupled pair of Göbel mirrors, both from Rigaku (Tokyo, Japan), a 3-pin-hole collimation system similar to the Bruker one and a mar345 image plate detector (marXperts, Norderstedt, Germany) with sample-to-detector distance  $0.15\ \text{m}$ . At contrast with the Bruker system, only the collimation flight path is evacu-

ated. Acquisition times on the instruments were in the order of 5 hours (Bruker Nanostar) or 1 hour (custom instrument). Temperature, fixed at  $20^\circ\text{C}$ , is controlled to within  $\pm 0.2^\circ\text{C}$  by a water circulation system (Bruker Nanostar) or, with a lesser precision, by the air-conditioning system of the room (custom instrument). For both instruments, the 2D detector images were most often characteristic of slightly oriented samples, as previously observed [6, 12], presumably because of the shear applied when filling the x-ray capillaries, or spreading the thick samples on the circular opening of the sample holders. Data was therefore azimuthally averaged to yield (normalised) intensities  $I$  vs. scattering wave vector  $q$  curves.

## 3 Experimental results and discussion

### 3.1 Results

SAXS results (“small” and “large” angle configurations) for ten selected samples are shown for illustration in fig. 3, in the  $Iq^2$  Kratky representation that factorises out the characteristic  $1/q^2$  intensity decrease of very extended, thin and flat particles with random orientations [35]. The

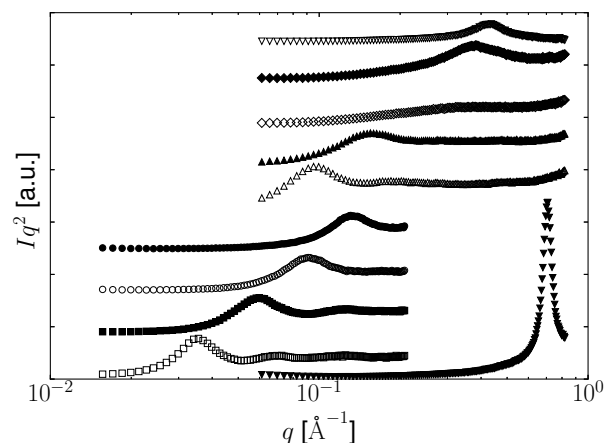


**Figure 3.** SAXS spectra (Kratky plot:  $Iq^2$  vs.  $q$ ) for GO aqueous dispersions differing by their GO mass fractions  $f_m$ : 0.04 ( $\square$ ), 0.07 ( $\blacksquare$ ), 0.10 ( $\circ$ ), 0.14 ( $\bullet$ ), 0.12 ( $\triangle$ ), 0.16 ( $\blacktriangle$ ), 0.21 ( $\diamond$ ), 0.26 ( $\blacklozenge$ ), 0.38 ( $\nabla$ ) and 0.62 ( $\blacktriangledown$ ). Data shifted vertically by amounts allowing a better visualisation

observed peak, characteristic of the lamellar stacking, moves towards higher scattering wave vector as dehydration proceeds. The second order peak, though clearly observed in either the “small” or “large” angle configurations for the two more hydrated samples in the corresponding series (GO mass fractions  $f_m$  0.04 and 0.07, or 0.12 and 0.16, respectively), barely appears in the “large” angle configuration for the other samples—even though it still falls within the observation window. Nevertheless, as shown in fig. 4 with an observation window extending to much larger scattering wave vector values, the second order Bragg peak

of the lamellar stacking, though weak, is clearly observed in one of the most dehydrated sample ( $f_m = 0.792$ ). As

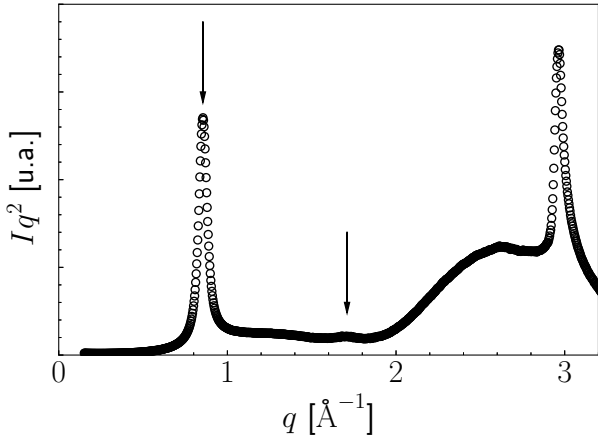


**Figure 4.** X-ray scattering data for the driest GO dispersion ( $f_m = 0.792$ ). Lamellar stacking peaks marked by vertical arrows at  $q_0 = 8.548 \times 10^{-1} \text{ \AA}^{-1}$  and  $\approx 1.71 \text{ \AA}^{-1}$ . The 2D, in-plane order of the carbon atoms in GO sheets gives rise to the intense and thin peak observed at  $q_G = 2.964 \text{ \AA}^{-1}$ . Other intensity humps at  $\approx 2.6 \text{ \AA}^{-1}$ : Unidentified features, possibly related to experimental artefacts arising from background scattering

a matter of fact, upon increasing the GO content up to  $f_m \approx 0.23$ , the intensity ratio between the second and first order peaks decreases until the second order peak apparently disappears, to be unambiguously recovered when  $f_m$  reaches *ca.* 0.29. In this concentration range, the first order peak is also significantly *broadened*—see fig. 5. Such

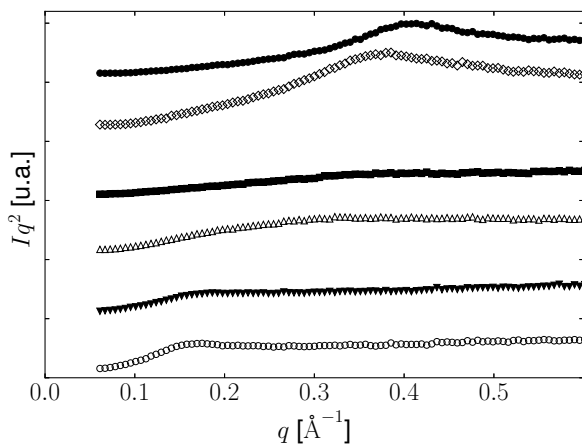


**Figure 5.** SAXS spectra in the Kratky representation for hydration values of the GO aqueous dispersions corresponding to a very broad first order Bragg peak. GO mass fraction  $f_m$ : 0.17 ( $\circ$ ), 0.19 ( $\blacktriangledown$ ), 0.21 ( $\triangle$ ), 0.23 ( $\blacksquare$ ), 0.26 ( $\diamond$ ), and 0.29 ( $\bullet$ ). Data shifted vertically by amounts allowing a better visualisation

features of the SAXS diffractograms may point to a structural phase transition. It is, however, not evidenced in the POM observations. We return to this intriguing point immediately below.

From Bragg's law, namely  $\ell = 2\pi/q_0$ , it is found that, as expected, the period of the lamellar stack decreases when water is removed from the structure. The experimental dilution law  $\ell(\varphi)$ , with volume fractions  $\varphi$  derived from mass fractions  $f_m$  through the relation

$$\varphi = \frac{\rho_{\text{H}_2\text{O}} f_m}{\rho_{\text{H}_2\text{O}} f_m + \rho_{\text{GO}} (1 - f_m)} \quad (5)$$

(assuming volume additivity) is shown in fig. 6. A striking

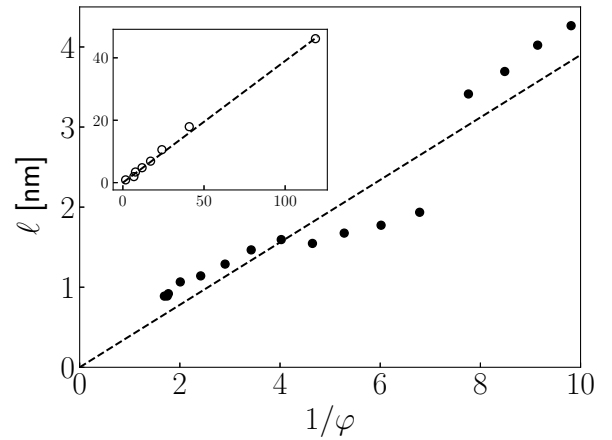


**Figure 6.** Stacking period  $\ell$  as a function of the inverse volume fraction  $1/\varphi$  for highly dehydrated GO dispersions ( $0.1 \leq \varphi$ , or  $0.17 \leq f_m$ ). Inset: *idem* for the whole dilution range. Dashed line: Simple swelling law  $\ell = t/\varphi$ , drawn with  $t = 0.39 \text{ nm}$

*discontinuous* behaviour near  $\varphi \approx 0.14$  ( $f_m$  close to 0.23) is clearly observed in the dehydrated limit of the dilution line. Besides, the discontinuity is precisely found to occur in the hydration range where broadening of the first order peak, as well as the disappearance of the second order peak have been observed, hinting again at the occurrence of a structural phase transition. Still, as evidenced in the inset to fig. 6 where SAXS data from samples submitted to the first concentration step (sect. 2.2)—some of them re-diluted—or only mildly dehydrated in the second step has been included, our data remains broadly compatible with the simple swelling law, eq. (2). This latter observation is nicely in agreement with the findings of previous studies, limited then to significantly more *dilute* GO dispersions [6, 12] than investigated here. The fit to the dilution data leads to a sheet thickness  $t \approx 0.39 \text{ nm}$ , a value close to, yet slightly lower than the value found in ref. [12]. The structural phase transition, if any, does therefore not strongly weaken the relevance of the simple geometric arguments at the origin of the simple swelling law.

As shown for illustration in fig. 4 corresponding to our driest sample ( $f_m = 0.792$ ), the expected locally planar

hexagonal structure of the carbon atoms in the graphene layers is observed using x-ray scattering at large angles. The peak found for  $q_G \approx 2.964 \text{ \AA}^{-1}$  can be related to the C-C nearest-neighbour distance  $d_{C-C}$  in a given graphene layer using  $3d_{C-C} = 4\pi/q_G$ , which indeed yields a result (1.41 Å) close to the commonly accepted value  $d_{C-C} = 1.42 \text{ \AA}$  [36]. The same result is found for more hydrated samples, as long as there is enough signal for this peak to emerge from the background.

Two peaks (locations  $q_0 = 0.85$  and  $1.71 \text{ \AA}^{-1}$ , close to  $2q_0$ ) can be found in the lower  $q$ -range part of fig. 4. They are related to the lamellar stacking order of the GO sheets. The corresponding periodicity, about 0.74 nm, is *ca.*  $1.9\times$  higher than the geometric parameter  $t \approx 0.39 \text{ nm}$  found in fitting the simple dilution law to the whole set of SAXS data, that is to say about twice higher than the interlayer distance in *graphite* [36]. This result is to be attributed to the water molecules remaining trapped between the GO sheets, about 46% in volume fraction from eq. (2), a value found in rather reasonable agreement with eq. (5), leading to  $\varphi_w \equiv 1 - \varphi = 0.32$ .

### 3.2 Discussion

Despite a possible structural transition, occurring near  $\varphi = 0.14$  and remaining to be characterised in details, it appears that GO aqueous dispersions exhibit a lamellar order over a quite extended concentration range, with a stacking period  $\ell$  varying from about 0.8 nm in the driest available system to more than 45 nm in our most hydrated samples. It is worth noting here that periods as large as  $\ell \approx 100 \text{ nm}$  have even been found in other studies [6]. The physical mechanism stabilising the lamellar structure for vastly different water contents is therefore of obvious interest.

In the so-called lyotropic lamellar phases (self-assembled bilayers of surfactant or lipid molecules separated by layers of solvent, or solvent-swollen block-copolymer systems), a similar swelling of the lamellar structure over very extended composition ranges is also commonly observed [37–42]. It is similarly present in systems structurally similar to GO, *viz.* based on extended solid-like sheets–phosphoantimonate, for instance [15], or clay-based systems [16]–dispersed in aqueous solutions. Such a swelling is commonly attributed to long-range, either direct or effective, repulsive interactions between the stacked sheets, acting across the solvent layers and of electrostatic origin, or resulting from the “undulation interaction” mechanism proposed by HELFRICH [26].

In the case of GO aqueous dispersions, the two mechanisms have already been identified [6, 43], at least indirectly in the case of HELFRICH’s mechanism [43]. An electrostatic contribution is clearly evidenced when experimentally studying the swelling properties in the presence of added salts (in order to vary the ionic strength of the aqueous solvent layers). Using NaCl as a typical univalent salt in the (nominal) concentration range  $10^{-6}$ – $10^{-1} \text{ M}$ , the same effect as described in ref. [6] is observed here, namely a *decreasing* stacking period  $\ell$  with increasing salt

content above a  $f_m$ -dependent salt concentration  $c_s^*$ . In-

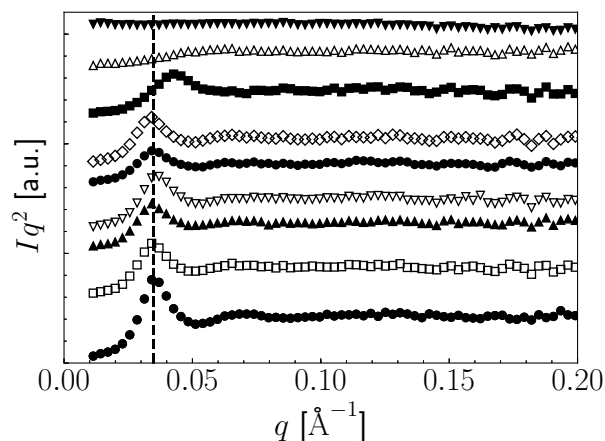


**Figure 7.** SAXS spectra in the Kratky representation for GO aqueous dispersions differing in added NaCl content  $c_s$ . GO mass fraction fixed to  $f_m = 4.3\%$ . Nominal salt concentrations  $c_s = 1 \times 10^{-6} \text{ M}$  ( $\bullet$ ),  $1 \times 10^{-5} \text{ M}$  ( $\square$ ),  $5 \times 10^{-5} \text{ M}$  ( $\blacktriangle$ ),  $1 \times 10^{-4} \text{ M}$  ( $\nabla$ ),  $5 \times 10^{-4} \text{ M}$  ( $\circ$ ),  $1 \times 10^{-3} \text{ M}$  ( $\diamond$ ),  $5 \times 10^{-3} \text{ M}$  ( $\blacksquare$ ),  $5 \times 10^{-2} \text{ M}$  ( $\triangle$ ) and  $1 \times 10^{-1} \text{ M}$  ( $\blacktriangledown$ ). Data shifted vertically by amounts allowing a better visualisation. The vertical dashed line is drawn at  $q_0 = 3.49 \times 10^{-2} \text{ \AA}^{-1}$

deed, as shown in fig. 7, up to the salt concentration  $c_s^*$  (found about  $1 \times 10^{-3} \text{ M}$  for  $f_m = 4.3\%$ ), the first order Bragg peak position  $q_0$  does not significantly change, and the overall appearance of the SAXS spectra remains the same. Conversely, the stacking period decreases and, simultaneously, the first order Bragg peak broadens, then becomes barely noticeable as the salt concentration increases above  $c_s^*$ . Repeating the experiment at a different value for the GO mass fraction ( $f_m = 1.4\%$ ) yields qualitatively similar observations (data not shown), with however a significant *decrease* in the value (about  $1 \times 10^{-4} \text{ M}$ ) for  $c_s^*$ .

Regarding now “undulation interactions”, results have been interpreted in recent rheoSAXS experiments by introducing a bending modulus  $\kappa$  for GO layers in the order of  $k_B T$ , that is to say “superflexible” sheets [43]. Such a low value suggests quite strong steric repulsions between adjacent GO layers, owing to the confinement of undulation fluctuations. This would nicely explain the conspicuous swelling properties of the system and, in particular, the salt effect mentioned above. Indeed, as has been firmly established since HELFRICH’s seminal article [26], swelling properties in lamellar stacks of *flexible* sheets result from a competition between, on one hand, the “unbinding” tendency of undulation fluctuations and, on the other hand, direct sheet–sheet interactions that may favour “bound” systems if attractive enough [27, 28]. An illustration may be found in a recent study of lamellar stacks of lipid bilayers [44–46], where the delicate interplay between “unbinding” tendencies and interactions favouring “bound” systems was varied by controlling the bilayer molecular composition. This amounted to varying simultaneously

the bending modulus  $\kappa$  (“unbinding” tendencies) and the virial coefficient  $\chi$  that encapsulates in the model the effect of interactions [28, 44–46], in a way somehow similar to the theoretical approach to the lamellar–lamellar phase coexistence proposed in ref. [47].

As regards the salt effect on GO stacks, interpretations may be simpler than in refs. [45, 46], at least if it is safe to assume that the main effect of salt (screening electrostatic repulsive interactions through the decrease of the Debye screening length) falls upon the parameter  $\chi$  *only*,  $\kappa$  being therefore unaffected. In such a simple limit, the MILNER–ROUX virial coefficient  $\chi$  should be a monotonously increasing function of  $c_s$ , since VAN DER WAALS attractions between GO sheets would be less and less counterbalanced by electrostatic repulsions [28], as classically described for colloidal particles in the DLVO theory [48]. The thermodynamic analysis of the unbinding transition then leads to a (schematic) phase diagram, displayed in the  $(\varphi, \chi)$ -plane in fig. 8, following refs. [28, 49].

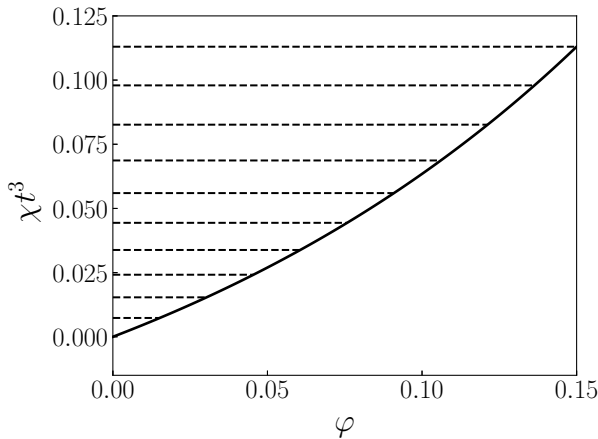


**Figure 8.** Phase diagram of a stack of GO sheets in the  $(\varphi, \chi)$  plane drawn in the case where bending modulus  $\kappa/(k_B T) = 1$ . The MILNER–ROUX virial coefficient  $\chi$  is made dimensionless by normalising to the volume built from the sheet thickness  $t$ . Horizontal dashed lines are binodals, linking excess solvent with a “bound” lamellar stack

The general features of the phase diagram are in qualitative agreement with available observations. As long as the salt concentration  $c_s$  is low enough, interactions between GO sheets are essentially repulsive,  $\chi$  should remain “small” (possibly negative) and the system is homogeneous–blank region in fig. 8. In this case, for any given  $\varphi$ ,  $\ell$  cannot depend on  $c_s$  and obtains according to eq. (2) as  $\ell = t/\varphi$ . However, when  $c_s$  increases above a threshold concentration  $c_s^*(\varphi)$ , VAN DER WAALS attractions start being dominant in the sense that the virial coefficient  $\chi(c_s)$  becomes larger than the swelling limit line  $\chi(\varphi)$  drawn in fig. 8. For the same given overall composition  $\varphi$ , the swollen stack of GO sheets phase-separates, part of the volume being filled with *pure* solvent ( $\varphi_l = 0$ ), a *more concentrated* GO–solvent system with  $\varphi_r \geq \varphi$  occupying the remaining volume–left- and right-end of dashed binodals in fig. 8.

Since  $\ell$  remains equal to  $t/\varphi_r$  in the swollen stack, the observed stacking period starts *decreasing*. Because the swelling limit line  $\chi(\varphi)$  in fig. 8 increases with  $\varphi$ , the phase separation phenomenon occurs earlier (*i.e.* for a lower salt content) if the lamellar stack is initially more dilute.

To proceed further in quantitative terms, it would be desirable to directly measure the properties controlling the swelling behaviour in GO stacks, *viz.* the bending modulus  $\kappa$  of the GO sheet and the sheet–sheet interaction potential or, at least, the MILNER–ROUX virial coefficient  $\chi$  [28], in particular as a function of  $c_s$ . As an intermediate step before reaching this ultimate goal, we propose below a method (based upon a model description of the small-angle x-ray–or neutron–diffractograms) for estimating the CAILLÉ exponent  $\eta$ . This parameter was originally introduced for describing elastic fluctuations in smectic A liquid crystals [50–52] and is related to both smectic layer flexibility and interactions. It also proved useful in interpreting characteristic features of diffractograms of lyotropic lamellar  $L_\alpha$  phases see, *e.g.*, [38, 44, 53, 54], as well as of GO stacks [6].

The intensity  $I$  of the radiation scattered by unoriented (“powder”) lamellar samples can be shown to a good approximation to be proportional to the product of two main terms [35, 53]

$$I(q) = A \frac{2\pi}{q^2} P(q) S(q) \quad (6)$$

where  $P$  and  $S$  are, respectively, the form and structure factors, accounting for the scattering along their normal by isolated flat “particles” and, along the stacking axis, by a 1D periodic structure. In eq. (6),  $q$  is the magnitude of the scattering wave vector and  $A$  is a normalising constant that depends on “particle”–solvent contrast, composition, etc. The  $1/q^2$  term accounts at large enough wave vectors for the powder average [35], and can also be considered as the “particle” *in-plane* form factor [53].

With the further simplification of considering the GO sheets as *zero-thickness* “particles”, the form factor  $P$  no longer depends on  $q$  and remains equal to 1, an acceptable approximation in the investigated SAXS range. On the other hand, the structure factor is conveniently expressed as results from the following equations (7) and (8)

$$S(q) = 1 + 2 \sum_1^{N-1} \left(1 - \frac{n}{N}\right) \times \cos \left[ \frac{q\ell n}{1 + 2\Delta q^2 \ell^2 \alpha(n)} \right] \times \frac{\exp \left\{ -\frac{2q^2 \ell^2 \alpha(n) + \Delta q^2 \ell^2 n^2}{2[1 + 2\Delta q^2 \ell^2 \alpha(n)]} \right\}}{\sqrt{1 + 2\Delta q^2 \ell^2 \alpha(n)}} \quad (7)$$

$$\alpha(n) = \frac{\eta}{4\pi^2} [\log(\pi n) + \gamma] \quad (8)$$

where  $N$  is the number of correlated GO sheets in the lamellar stack,  $\ell$  the period of the structure,  $\Delta q$  the Gaussian width of the resolution (or FWHM/ $\sqrt{8 \ln 2}$ ), and  $\gamma \approx$

0.57721... the value of EULER's constant [53]. Note that owing to the logarithmic term in eq. (8), characteristic of the anomalous fluctuation properties in one-dimensional systems [50–52], the structure factor given in eq. (7) differs essentially from the results relevant for the so-called disorders of the first or second kinds, or para-crystalline theory—see, *e.g.*, [54, 55].

The model, though being somehow equivocal because the resolution of our experiment is limited, the distinction between (small)  $N$  and (large)  $\eta$  roles therefore becoming less clear-cut in some cases, has nevertheless been used to tentatively describe the diffractograms for some rather dilute samples (without adding salt), with GO mass fractions  $f_m = 1.4\%$ ,  $2.8\%$ ,  $4.3\%$  and  $7.1\%$  (volume fractions respectively  $\varphi \approx 0.8\%$ ,  $\approx 1.6\%$ ,  $\approx 2.4\%$  and  $\approx 4.1\%$ ). Figure 9 displays two results, and fitting parameters are given in table 1.

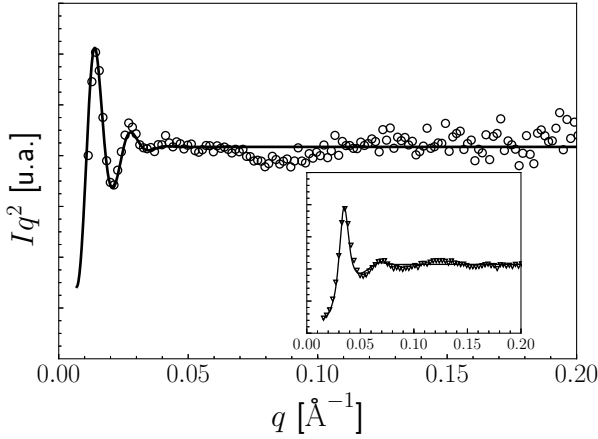


**Figure 9.** SAXS spectra in the Kratky representation for a  $f_m = 1.4\%$  GO dispersion in pure water ( $\circ$ ). The full line is the best fit of eq. (7) to the data. Inset:  $f_m = 4.3\%$  system ( $\nabla$ )

**Table 1.** Model parameters

Parameter	$f_m = 0.014$	$f_m = 0.028$	$f_m = 0.043$	$f_m = 0.071$
$\ell$ [nm]	42.7	23.8	17.4	10.2
$\eta$	0.39	0.75	0.65	0.93
$N$	20	10	10	7

A fair description of the small-angle scattering features is obtained when using the proposed model, with nevertheless obvious shortcomings for scattering wave vectors in the range  $\approx 0.08 - 0.16 \text{ \AA}^{-1}$  that may result from the crudeness of our assumption as regards the GO sheet form factor. In particular, the dangling oxygen-rich groups present in GO sheets may increase locally the sheet thickness, therefore contributing to out-of-plane features of the form factor not accounted for in our simplified description.

From the fitted values of the CAILLÉ exponent  $\eta$ , the smectic compression modulus  $B$  of the lamellar structure made of stacked GO sheets may be estimated. With

$$\eta = \frac{q_0^2 k_B T}{8\pi\sqrt{KB}} \quad (9)$$

from ref. [50], and using for the smectic splay modulus  $K$  the relation  $K = \kappa/\ell$  [26], we get

$$\frac{\ell^3 B}{k_B T} = \frac{\pi^2 k_B T}{4\kappa\eta^2} \quad (10)$$

or  $B \approx 6$  for  $f_m = 4.3\%$  (respectively,  $B \approx 16$  for  $f_m = 1.4\%$ ) in  $k_B T/\ell^3$  units if, as proposed in ref. [43], the value of the GO sheet bending modulus  $\kappa$  is actually equal to  $k_B T$ . Such values for the smectic compression modulus  $B$ , significantly *larger* than predicted in the HELFRICH model, namely  $\ell^3 B_H/(k_B T) = 9\pi^2 k_B T/(64\kappa)$  [26, 38] (or  $\approx 1.4$  in  $k_B T/\ell^3$  units), are quite reasonable in the presence of dominantly *repulsive* interactions between GO sheets. Indeed, from MILNER-ROUX analysis of the “un-binding” transition [28], the smectic compression modulus  $B$  should be expressed as [44]

$$\frac{\ell^3 B}{k_B T} = \frac{9\pi^2 k_B T}{64\kappa(1-t/\ell)^4} - 2\chi\ell t^2 \quad (11)$$

which, from eq. (10) with  $\ell$  and  $\eta$  values as given in table 1, yields roughly the same estimate for the virial coefficient  $\chi t^3 \approx -0.04$  for the two GO concentrations, with a *negative* sign as expected for overall repulsive interactions.

The structural phase transition that occurs in the vicinity of  $\ell = 2.5 \text{ nm}$  is actually also amenable, qualitatively at least, to an interpretation in terms of MILNER-ROUX arguments. As shown in fig. 10, the CAILLÉ exponent is

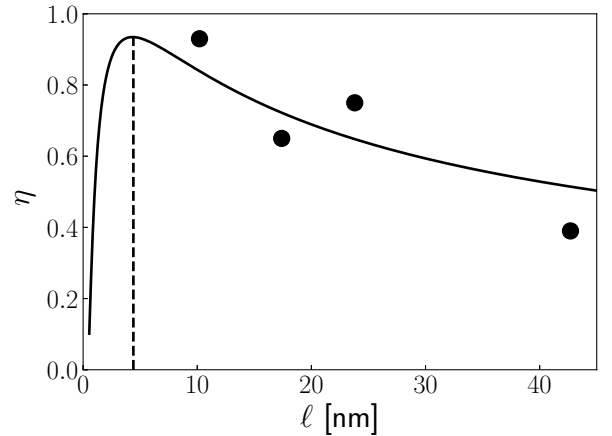


**Figure 10.** CAILLÉ exponent along the dilution line with pure water, as resulting from equations (9) and (11), with  $\kappa/k_B T = 1$ ,  $\chi t^3 = -0.036$ . GO sheet thickness  $t = 0.39 \text{ nm}$ . Vertical dashed line drawn at  $\ell^* = 5.4 \text{ nm}$ . Data points from table 1

expected to strongly *increase* when the lamellar stack of

GO sheets is dehydrated, until a characteristic period  $\ell^*$  is reached beyond which  $\eta$  decreases to very small values. As larger  $\eta$  values are associated to (lamellar) Bragg peaks with lesser peak intensities and broader tails, the quasi-disappearance of the first and second order Bragg peaks in a given dilution range (see fig. 5) may thus be understood, even though the predicted  $\ell^*$  value, namely 5.4 nm, clearly differs from its experimental counterpart. However, since the MILNER-ROUX description of the unbinding transition is a mean-field, *perturbative* theory, we believe that such a discrepancy should not be too seriously deplored for such concentration ranges where direct interactions between GO sheets are definitely strong.

## 4 Conclusion

A procedure to concentrate aqueous GO dispersions to significant dryness, with the benefit of avoiding the formation of aggregates has been implemented. The lamellar stacks of GO sheets obtained in an extended concentration range, from *ca.* 2 % to 72 %, can be reversibly swollen or dehydrated. The simple one-dimensional dilution law is largely obeyed over all the investigated hydration range, even though conspicuous discrepancies have been revealed by small-angle x-ray scattering studies that may indicate the occurrence of an underlying, as yet unidentified, structural phase transition.

The swelling behaviour of the aqueous GO dispersions can be interpreted, similarly to many lyotropic lamellar  $L_\alpha$  phases in amphiphilic systems, in terms of an entropic “force” arising from the confinement of undulation fluctuations (also known as HELFRICH undulation interactions) acting together, or competing with, direct forces, respectively electrostatic repulsions and VAN DER WAALS attractions. The so-called “unbinding transition” mechanism appears here to be mainly driven by the ionic strength of the aqueous medium swelling the GO sheets, as indirectly suggested by the quantitative analysis of the small-angle x-ray diffractograms in terms of a parameter, the CAILLÉ exponent  $\eta$ , that combines the bending and compression moduli characterising the elastic properties of lamellar phases. The analysis confirms the recently proposed “super-flexible” nature of GO sheets [43].

We thank Philippe Poulin, Cécile Zakri and Wilfrid Neri for fruitful discussions. We also thank Conselho Nacional de Desenvolvimento Científico e Tecnológico (CNPq - Brazil) for providing support to Rafael Leite Rubim through the program “Ciência sem Fronteiras” (processo CNPq nº 250085/2013-5).

Figures have been drawn with the 2D graphics package `Matplotlib` [56]

## 5 Author contribution statement

L.N., and F.N. conceived and planned the research. R.L.R. conceived and implemented the drying procedure. R.L.R., M.A.B., T.M., and K.B. contributed to sample preparation and carried out the experiments. All authors provided

critical feedback and helped shape the research, analysis and manuscript. All the authors have read and approved the final manuscript.

## References

1. William S. Hummers and Richard E. Offeman. Preparation of graphitic oxide. *Journal of the American Chemical Society*, 80(6):1339–1339, 1958.
2. Sasha Stankovich, Dmitriy A. Dikin, Richard D. Piner, Kevin A. Kohlhaas, Alfred Kleinhammes, Yuanyuan Jia, Yue Wu, SonBinh T. Nguyen, and Rodney S. Ruoff. Synthesis of graphene-based nanosheets via chemical reduction of exfoliated graphite oxide. *Carbon*, 45(7):1558–1565, June 2007.
3. Natnael Behabtu, Jay R. Lomeda, Micah J. Green, Amanda L. Higginbotham, Alexander Sinitiskii, Dmitry V. Kosynkin, Dmitri Tsentelovich, A. Nicholas G. Parra-Vasquez, Judith Schmidt, Ellina Kesselman, Yachin Cohen, Yeshayahu Talmon, James M. Tour, and Matteo Pasquali. Spontaneous high-concentration dispersions and liquid crystals of graphene. *Nature Nanotechnology*, 5:406–411, 2010.
4. Ji Eun Kim, Tae Hee Han, Sun Hwa Lee, Ju Young Kim, Chi Won Ahn, Je Moon Yun, and Sang Ouk Kim. Graphene oxide liquid crystals. *Angewandte Chemie International Edition*, 50(13):3043–3047, March 2011.
5. Hari Krishna Bisoyi and Sandeep Kumar. Carbon-based liquid crystals: art and science. *Liquid Crystals*, 38(11-12):1427–1449, November 2011.
6. Zhen Xu and Chao Gao. Graphene chiral liquid crystals and macroscopic assembled fibres. *Nature Communications*, 2:571, December 2011.
7. Rickard Frost, Gustav Edman Jönsson, Dinko Chakarov, Sofia Svedhem, and Bengt Kasemo. Graphene oxide and lipid membranes: Interactions and nanocomposite structures. *NANO Letters*, 12:3356–3362, June 2012.
8. Jaemyung Kim, Laura J. Cote, and Jiaying Huang. Two dimensional soft material: New faces of graphene oxide. *Accounts of Chemical Research*, 45(8):1356–1364, June 2012.
9. Zhen Xu and Chao Gao. Aqueous liquid crystals of graphene oxide. *ACS Nano*, 5(4):2908–2915, March 2011.
10. Seyed Hamed Aboutalebi, Mohsen Moazzami Gudarzi, Qing Bin Zheng, and Jang-Kyo Kim. Spontaneous formation of liquid crystals in ultralarge graphene oxide dispersions. *Advanced Functional Materials*, 21(15):2978–2988, August 2011.
11. Budhadipta Dan, Natnael Behabtu, Angel Martinez, Julian S. Evans, Dmitry V. Kosynkin, James M. Tour, Matteo Pasquali, and Ivan I. Smalyukh. Liquid crystals of aqueous, giant graphene oxide flakes. *Soft Matter*, 7(23):11154–11159, 2011.
12. Camilo Zamora-Ledezma, Nicolas Puech, Cécile Zakri, Eric Grelet, Simon E. Moulton, Gordon G. Wallace, Sanjeev Gambhir, Christophe Blanc, Eric Anglaret, and Philippe Poulin. Liquid crystallinity and dimensions of surfactant-stabilized sheets of reduced graphene oxide. *The Journal of Physical Chemistry Letters*, 3(17):2425–2430, 2012.

13. Jing Cao, Hua-Jie Yin, and Rui Song. Circular dichroism of graphene oxide: the chiral structure model. *Frontiers of Materials Sciences*, 7:83–90, 2013.
14. A. Di Mauro, R. Randazzo, S. F. Spano, G. Compagnini, M. Gaeta, L. D’Urso, R. Paolesse, G. Pomarico, C. Di Natale, V. Villari, N. Micali, M. E. Fragala, A. D’Urso, and R. Purrello. Vortexes tune the chirality of graphene oxide and its non-covalent hosts. *Chem. Commun.*, 52:13094–13096, 2016.
15. Jean-Christophe P. Gabriel, Franck Camerel, Bruno J. Lemaire, Hervé Desvaux, Patrick Davidson, and Patrick Batail. Swollen liquid-crystalline lamellar phase based on extended solid-like sheets. *Nature*, 413:504–508, 2001.
16. Laurent J. Michot, Isabelle Bihannic, Solange Maddi, Sérgio S. Funari, Christophe Baravian, Pierre Levitz, and Patrick Davidson. Liquid-crystalline aqueous clay suspensions. *Proceedings of the National Academy of Sciences*, 103:16101–16104, 2006.
17. Dzina Kleshchanok, Peter Holmqvist, Janne-Mieke Meijer, and Henk N. W. Lekkerkerker. Lyotropic smectic B phase formed in suspensions of charged colloidal platelets. *Journal of the American Chemical Society*, 134:5985–5990, 2012.
18. Lars Onsager. The effect of shape on the interaction of colloidal particles. *Annals of the New York Academy of Sciences*, 51:627–659, May 1949.
19. Daan Frenkel and Rob Eppenga. Monte Carlo study of the isotropic–nematic transition in a fluid of thin hard disks. *Physical Review Letters*, 49:1089–1092, 1982.
20. Giorgio Cinacchi and Alessandro Tani. The isotropic–nematic phase transition in hard, slightly curved, lens-like particles. *The Journal of Chemical Physics*, 141:154901, 2014.
21. Giorgio Cinacchi and Alessandro Tani. Isotropic–nematic phase transition in hard platelets as described by a third-virial theory. *The Journal of Physical Chemistry B*, 119:5671–5676, 2015.
22. Felix M. van der Kooij and Henk N. W. Lekkerkerker. Formation of nematic liquid crystals in suspensions of hard colloidal platelets. *The Journal of Physical Chemistry B*, 102(40):7829–7832, 1998.
23. Martin A. Bates and Daan Frenkel. Nematic–isotropic transition in polydisperse systems of infinitely thin hard platelets. *The Journal of Chemical Physics*, 110(13):6553–6559, 1999.
24. Zhen Xu and Chao Gao. Graphene in macroscopic order: Liquid crystals and wet-spun fibers. *Accounts of Chemical Research*, 47(4):1267–1276, February 2014.
25. Fengxia Geng, Renzhi Ma, Akira Nakamura, Kosho Akatsuka, Yasuo Ebina, Yusuke Yamauchi, Nobuyoshi Miyamoto, Yoshitaka Tateyama, and Takayoshi Sasaki. Unusually stable  $\sim 100$ -fold reversible and instantaneous swelling of inorganic layered materials. *Nature Communications*, 4:1632, 2013.
26. W. Helfrich. Steric interactions of fluid membranes in multilayer systems. *Zeitschrift für Naturforschung*, 33A:305–315, 1978.
27. Reinhard Lipowski and Stanislas Leibler. Unbinding transitions of interacting membranes. *Physical Review Letters*, 56:2541–2544, 1986.
28. S. T. Milner and D. Roux. Flory theory of the unbinding transition. *Journal de Physique I France*, 2:1741–1754, 1992.
29. Product Datasheet: Graphenea Graphene Oxide. [https://cdn.shopify.com/s/files/1/0191/2296/files/Graphenea\\_G0\\_Datasheet\\_2016-10-03.pdf?8258700468234452297](https://cdn.shopify.com/s/files/1/0191/2296/files/Graphenea_G0_Datasheet_2016-10-03.pdf?8258700468234452297). Accessed: 2015-05-03.
30. W. Scholz and H.P. Boehm. Betrachtungen zur struktur des graphitoxids. *Zeitschrift für anorganische und allgemeine Chemie*, 369:327–340, 1969.
31. A. Lurf, A. Buchsteiner, J. Pieper, S. Schottl, I. Dekany, T. Szabo, and H.P. Boehm. Hydration behavior and dynamics of water molecules in graphite oxide. *Journal of Physics and Chemistry of Solids*, 67:1106–1110, 2006.
32. Stéphan Rouzière, J. David Núñez, Erwan Paineau, Ana M. Benito, Wolfgang K. Maser, and Pascale Launois. Intercalated water in multi-layered graphene oxide paper: an X-ray scattering study. *Journal of Applied Crystallography*, 50:876–884, 2017.
33. Heon Ham, Tran Van Khai, No-Hyung Park, Dae Sup So, Joon-Woo Lee, Han Gil Na, Yong Jung Kwon, Hong Yeon Cho, and Hyoun Woo Kim. Freeze-drying-induced changes in the properties of graphene oxides. *Nanotechnology*, 25:235601, 2014.
34. T.C. Huang, H. Toraya, T.N. Blanton, and Y. Wu. X-ray powder diffraction analysis of silver behenate, a possible low-angle diffraction standard. *Journal of Applied Crystallography*, 26:180–184, 1993.
35. Otto Kratky and Gunther Porod. Diffuse small-angle scattering of x-rays in colloid systems. *Journal of Colloid Science*, 4(1):35–70, 1949.
36. J. D. Bernal. The structure of graphite. *Proceedings of the Royal Society of London A: Mathematical, Physical and Engineering Sciences*, 106(740):749–773, 1924.
37. F. C. Larche, J. Appell, G. Porte, P. Bassereau, and J. Marignan. Extreme swelling of a lyotropic lamellar liquid crystal. *Physical Review Letters*, 56:1700–1703, 1986.
38. C. R. Safinya, D. Roux, G. S. Smith, S. K. Sinha, P. Dimon, N. A. Clark, and A. M. Bellocq. Steric interactions in a model multimembrane system: A synchrotron x-ray study. *Physical Review Letters*, 57:2718–2721, 1986.
39. Reinhard Strey, Reinhard Schomäcker, Didier Roux, Frédéric Nallet, and Ulf Olsson. Dilute lamellar and  $L_3$  phases in the binary water  $C_{12}E_5$  system. *Journal of the Chemical Society Faraday Transactions*, 86:2253–2261, 1990.
40. Éric Freyssingéas, Didier Roux, and Frédéric Nallet. Quasi-elastic light scattering study of a highly swollen lamellar and “sponge” phase. *Journal de Physique II France*, 7:913–929, 1997.
41. Masateru M. Ito, Kohzo Ito, Mitsuhiro Shibayama, Kenji Sugiyama, and Hideaki Yokoyama. Phase behavior of block copolymers in selective supercritical solvent. *Macromolecules*, 48:3590–3597, 2015.
42. Yoshiaki Uchida, Takuma Nishizawa, Takeru Omiya, Yuichiro Hirota, and Norikazu Nishiyama. Nanosheet formation in hyperswollen lyotropic lamellar phases. *Journal of the American Chemical Society*, 138:1103–1105, 2016.
43. Philippe Poulin, Rouhollah Jalili, Wilfrid Neri, Frédéric Nallet, Thibaut Divoux, Annie Colin, Seyed Hamed Aboutalebi, Gordon Wallace, and Cécile Zakri. Superflexibility of graphene oxide. *Proceedings of the National Academy of Sciences*, 113:11088–11093, 2016.
44. K. Bougis, R. Leite Rubim, N. Ziane, J. Peyencet, A. Bentalib, A. Février, C.L.P. Oliveira, E. Andreoli de Oliveira, L. Navailles, and F. Nallet. Stabilising lamellar stacks of

- lipid bilayers with soft confinement and steric effects. *European Physical Journal E: Soft Matter*, 38:78, 2015.
45. R. Leite Rubim, B.B. Gerbelli, K. Bougis, C.L. Pinto de Oliveira, L. Navailles, F. Nallet, and E. Andreoli de Oliveira. Water activity in lamellar stacks of lipid bilayers: “Hydration forces” revisited. *European Physical Journal E: Soft Matter*, 39:3, 2016.
  46. Kévin Bougis. *Fluctuations et interactions en situation de nano-confinement anisotrope*. PhD thesis, université de Bordeaux - Universidade de São Paulo, 28 November 2016.
  47. Massimo G. Noro and William M. Gelbart. Theory of lamellar–lamellar phase transitions in pure and mixed surfactant solutions. *The Journal of Chemical Physics*, 111:3733–3743, 1999.
  48. Barry W. Ninham. On progress in forces since the DLVO theory. *Advances in Colloid and Surface Science*, 83:1–17, 1999.
  49. Frédéric Nallet. Surfactant films in lyotropic lamellar (and related) phases: Fluctuations and interactions. *Advances in Colloid and Interface Science*, 247:363–373, 2017.
  50. Alain Caillé. Remarques sur la diffusion des rayons X dans les smectiques A. *Comptes rendus de l’Académie des sciences Paris, série B*, 274:891–893, 1972.
  51. Leon Gunther, Yosef Imry, and Joseph Lajzerowicz. X-ray scattering in smectic-A liquid crystals. *Physical Review A*, 22:1733–1740, 1980.
  52. P.-G. de Gennes and J. Prost. *The physics of liquid crystals Second edition*. Clarendon Press Oxford, 1993.
  53. Frédéric Nallet, René Laversanne, and Didier Roux. Modelling x-ray or neutron scattering spectra of lyotropic lamellar phases: Interplay between form and structure factors. *Journal de Physique II*, 3(4):487–502, 1993.
  54. Ruitian Zhang, Robert M. Suter, and John F. Nagle. Theory of the structure factor of lipid bilayers. *Physical Review E*, 50:5047–5060, 1994.
  55. Mitsuhiro Shibayama and Takeji Hashimoto. Small-angle x-ray scattering analyses of lamellar microdomains based on a model of one-dimensional paracrystal with uniaxial orientation. *Macromolecules*, 19:740–749, 1986.
  56. J. D. Hunter. Matplotlib: A 2D graphics environment. *Computing In Science & Engineering*, 9(3):90–95, 2007.

# Appendix B

## Résumé détaillé

Cette thèse a été développée au sein de l'équipe Matière Molle : Structure et Dynamique (M2SD) au Centre de recherche Paul-Pascal (UMR5031), un laboratoire situé à Pessac et attaché à l'Université de Bordeaux et au Centre National de la Recherche Scientifique (CNRS), dont le financement a été accordé par le programme Sciences sans Frontières, une initiative du gouvernement brésilien au travers du Conseil National de Développement Scientifique et Technologique (CNPq).

Après l'étude développée par Emerson Rodrigo da Silva (da Silva, 2011), qui a ensuite été continuée par Kévin Bougis (Bougis, 2016), la formulation des complexes composés de bicouches lipidiques a été poursuivie dans le groupe. À l'aide des techniques comme la diffusion de rayons x aux petits angles, les microscopies optique et électronique, les propriétés du système formé par une structure lamellaire hôte et des fragments d'ADN ont été étudiées.

Les fragments d'ADN sont assez petits pour être vus fondamentalement comme des cylindres, des particules unidimensionnelles. L'insertion/organisation de ces macro molécules entre les bicouches, une matrice bidimensionnelle, donne lieu à des différentes structures auto-associées.

Ce travail a été l'inspiration pour étudier, d'un point de vue fondamental, le couplage entre des bicouches amphiphiles auto-associées (lesquelles peuvent être vues comme une matrice anisotrope formée d'objets bidimensionnels) et un objet lui-même bidimensionnel, en l'occurrence le feuillet d'oxyde de graphène, quand ils sont dispersés dans un solvant commun.

Dès sa découverte, le graphène oxydé (GO), dont la structure est présentée en Figure 2.1c et considéré le plus accessible des précurseurs du graphène, a été largement utilisé pour des applications en science et technologie. L'objectif de cette thèse est d'étudier les effets du confinement sur des systèmes complexes auto-associés de matière molle et, en particulier, l'insertion des feuillets de GO dans une matrice fluide anisotrope. La compétition entre les élasticités intrinsèques des bicouches et des feuillets de GO, ainsi que les interactions directes bicouche-bicouche, bicouche-GO et GO-GO, permet d'envisager un riche

polymorphisme en fonction de la composition du système.

Avant l'étude des complexes du système ternaire, le système binaire composé de GO et de l'eau a été exploré. Une caractérisation des feuillets a été réalisée, ce qui a donné une extension latérale de l'ordre du micromètre avec une polydispersité élevée, comme montré en Figure 3.4 et Figure 3.5. Comme décrit en section 3.2, un procédé pour obtenir des dispersions aqueuses de GO à très fortes concentrations a été développé, ce qui a permis l'étude d'une large gamme de concentrations de la dispersion. Les échantillons obtenus sont libres d'agrégats et peuvent être réversiblement gonflés ou deshydratés, ce qui n'est pas faisable avec le GO en poudre.

La Figure 3.14, résultat des expériences de diffusion de rayons X aux petits angles, révèle un comportement typique des cristaux liquides pour les dispersions aqueuses de GO, où des phases organisées peuvent être obtenues avec l'augmentation de la concentration du système. Les phases smectiques obtenues obéissent à la loi de dilution usuelle, caractéristique des cristaux liquides lyotropes, dans la gamme d'hydratation explorée. Une représentation schématique du phénomène est donnée en Figure 3.15.

Le gonflement des dispersions aqueuses de GO peut être interprété en termes des forces qui agissent sur les feuillets. L'équilibre entre les interactions attractives et répulsives stabilise la structure lamellaire et nous avons démontré l'importance de la répulsion électrostatique dans le domaine hydraté, en compétition avec d'autres contributions, pour diluer la structure empilée.

Néanmoins, dans un petit domaine de concentrations, un écart entre la loi de dilution et les données expérimentales est observé, ce qui peut indiquer une transition de phase structurale. Bien que les détails de ce phénomène restent à être identifiés, ce comportement anormal peut être lié au fait que, pour les phases fortement confinées, les groupements oxygénés dans la surface des feuillets de GO s'interpénètrent. Quand la structure est diluée, la périodicité lamellaire augmente et les couches perdent leur contact. Une représentation schématique peut être donnée en Figure 4.7. Ce phénomène affecte les interactions entre les feuillets adjacents, un effet qui est détecté sur la courbe de dilution. Les résultats de cette partie du travail ont été publiés en Rubim et al. (2018) et l'article complet peut être consulté en Appendice A.

Pour des dispersions de GO plus diluées, des modèles de diffusion de rayons x ont été adaptés et employés pour extraire les paramètres structuraux du système analysé. La forme et l'organisation de feuillets ont été étudiées, comme décrit en section 4.2, et les résultats des ajustements sont présentés en Figure 4.6.

L'épaisseur du feuillet de GO, obtenue à partir du contraste de densité électronique, est en accord avec les valeurs décrites dans la littérature. En considérant des densités électroniques différentes pour le plan des atomes de carbone et des groupes oxygénés, une épaisseur autour de 15 Å est obtenue. La partie interne du feuillet, qui mesure autour de 6 Å, a une longueur compatible avec l'épaisseur du graphène. Cependant, si l'on considère une densité électronique moyenne pour les deux parties du feuillet, une épaisseur

approximative de 10 Å est obtenue.

La structure organisée en lamelles a aussi été caractérisée avec les modèles mis en œuvre. Les paramètres sensibles à la flexibilité des feuillets ont été obtenus et leur comportement, en fonction de l'hydratation du système, a été analysé. Ces résultats ont conduit à l'extraction du module de compressibilité de la structure empilée. La Figure 4.8 montre que, comme prévu pour des systèmes comme les phases lamellaires de GO, plus petite est la distance entre les feuillets, plus élevée est la force nécessaire pour les écarter de leur position d'équilibre.

Ensuite, le système binaire composé de tensioactif et d'eau acidifiée a été exploré. Les expériences ont révélé la formation de bicouches amphiphiles organisées en une structure lamellaire pour les systèmes faiblement et moyennement concentrés. La structure obéit aussi à la loi de dilution, ce qui veut dire qu'elle gonfle quand le solvant est rajouté au système. Néanmoins, une transition de phase est observée pour les échantillons fortement concentrés et une structure non définie est observée.

Cette étude a permis l'exploration du système binaire deshydraté composé de feuillets de GO et de tensioactif. La cinétique de ce système a montré que des très longs temps d'homogénéisation sont nécessaires pour stabiliser la structure, un facteur source d'inconvénients pour l'étude.

Pour de plus faibles quantités de tensioactif, les feuillets de GO s'organisent en une structure empilée et les amphiphiles s'adsorbent à leur surface. Avec une augmentation de la quantité de tensioactif, les molécules s'organisent dans la surface et la structure gonfle, jusqu'au moment où la limite de dilution est atteinte. À ce moment, le tensioactif forme une structure similaire à celle d'une bicouche, où la partie hydrophile reste en contact avec le feuillet. Pour des concentrations encore plus élevées en tensioactif, les amphiphiles en excès forment une phase séparée, qui est aussi structurée. La Figure 5.12 représente schématiquement les phases décrites.

Les phases décrites peuvent aussi être diluées à l'eau, auquel cas les molécules d'eau vont s'insérer à la surface des feuillets. Pour les systèmes avec une proportion élevée en tensioactif et qui représentent un domaine restreint du diagramme ternaire, une nouvelle phase est observée. Dans cette nouvelle phase, les amphiphiles se détachent du feuillet de GO et s'organisent en bicouches, qui sont séparées par des couches d'eau avec les feuillets en dispersion. Les représentations schématiques de ces phases se trouvent en Figure 5.18. Les domaines du diagramme ternaire, où chacune des phases sont observées, sont délimités par des zones de transition, dans lesquels les deux phases ou même d'autres phases peuvent coexister.

Deux complexes ternaires distincts ont été obtenus, dont les zones d'existence sont séparées par des régions de transition. Le domaine de transition est directement lié aux systèmes binaires respectifs, cependant quelques structures sont toujours à caractériser en détail.

Tous les résultats obtenus pour les systèmes étudiés ont permis la construction du

digramme ternaire présenté en Figure 5.20, ce qui résume les structures observées.

# Appendix C

## Resumo detalhado

Esta tese foi desenvolvida na equipe Matéria Mole: Estrutura e Dinâmica (M2SD) do Centro de Pesquisas Paul-Pascal (UMR5031), laboratório localizado em Pessac (França) e vinculado à Universidade de Bordeaux e ao Centro Nacional de Pesquisa Científica (CNRS), e financiada pelo programa Ciências sem Fronteiras, uma iniciativa do governo brasileiro através do Conselho Nacional de Desenvolvimento Científico e Tecnológico (CNPq).

Após o estudo desenvolvido por Emerson Rodrigo da Silva (da Silva, 2011), posteriormente seguido por Kévin Bougis (Bougis, 2016), a formulação de complexos de bicamadas lipídicas foi mantida em foco no grupo. Utilizando técnicas como espalhamento de raios-X a baixos ângulos e microscopias ótica e eletrônica, as propriedades do sistema formado por uma estrutura lamelar hospedeira e fragmentos de DNA foram investigados.

Os fragmentos de DNA são pequenos o suficiente para serem vistos fundamentalmente como cilindros, que são partículas unidimensionais. A inserção/organização dessas macromoléculas entre as bicamadas, uma matriz bidimensional, dá origem à diferentes estruturas auto-organizadas.

Este trabalho foi a inspiração para estudar, do ponto de vista fundamental, o acoplamento entre as bicamadas anfífilas auto-organizadas (que podem ser vistas como uma matriz anisotrópica formada por objetos bidimensionais) e um objeto ele mesmo bidimensional, neste caso a folha de óxido de grafeno, quando estão dispersados em um solvente comum.

Desde a sua descoberta, o grafeno oxidado (GO), cuja estrutura é apresentada na Figura 2.1c e considerado o mais acessível dos precursores do grafeno, tem sido amplamente utilizado para aplicações na ciência e tecnologia. O objetivo desta tese é de estudar os efeitos do confinamento em sistemas complexos auto-organizados da matéria mole e, em particular, a inserção de folhas de GO em uma matriz fluida anisotrópica.

A competição entre as elasticidades intrínsecas das bicamadas e das folhas de GO, assim como as interações diretas bicamada-bicamada, bicamada-GO e GO-GO, permitem esperar um rico polimorfismo em função da composição do sistema.

Antes de investigar os complexos do sistema ternário, o sistema binário composto de

GO e água foi explorado. Uma caracterização das folhas foi realizada, cujo resultado obtido foi uma extensão lateral da ordem do micrômetro com uma grande polidispersidade, como pode ser observado na Figura 3.4 e na Figura 3.5. Como descrito na Seção 3.2, um procedimento para obter dispersões aquosas de GO a concentrações elevadas foi desenvolvido, o que permitiu o estudo de uma ampla gama de concentrações da dispersão. As amostras obtidas não apresentam agregados e podem ser reversivelmente diluídas ou desidratadas, o que não é possível com o GO em pó.

A Figura 3.14, resultado dos experimentos de espalhamento de raios-X a baixos ângulos, revela um comportamento típico de cristais líquidos para as dispersões aquosas de GO, onde as fases organizadas podem ser obtidas com um aumento da concentração do sistema. As fases esmélicas obtidas obedecem a lei de diluição usual, característica de cristais líquidos liotrópicos, no intervalo de hidratação explorado. Uma representação esquemática do fenômeno é apresentada na Figura 3.15.

A expansão das dispersões aquosas de GO pode ser interpretada em termos das forças que agem sobre as folhas. O equilíbrio entre as interações atrativas e repulsivas estabiliza a estrutura lamelar e nós demonstramos a importância da repulsão eletrostática no regime hidratado, em competição com outras contribuições, para diluir a estrutura empilhada.

No entanto, em um pequeno domínio de concentrações, um distanciamento em relação à lei de diluição e os dados experimentais é observado, o que pode indicar uma transição de fase estrutural. Apesar dos detalhes deste fenômeno ainda precisarem ser identificados, este comportamento anormal pode estar ligado ao fato de que, para as fases muito concentradas, os grupos oxigenados na superfície das folhas de GO se interpenetram. Quando a estrutura é diluída, a periodicidade lamelar aumenta e as folhas perdem o contato entre elas. Uma representação esquemática pode ser observada na Figura 4.7. Este fenômeno afeta as interações entre as folhas adjacentes, um efeito que é detectado na curva de diluição. Os resultados dessa parte do trabalho foram publicados em Rubim et al. (2018) e o artigo completo pode ser consultado no Apêndice A.

Para dispersões de GO mais diluídas, modelos de espalhamento de raios-X foram adaptados e empregados para extrair os parâmetros estruturais do sistema analisado. A forma e a organização das folhas foram estudadas, como descrito na Seção 4.2, e os resultados dos ajustes são apresentados na Figura 4.6.

A espessura da folha de GO, obtida à partir do contraste de densidade eletrônica, esta de acordo com valores descritos na literatura. Considerando densidades eletrônicas diferentes para o plano de átomos de carbono e para os grupos oxigenados, uma espessura em torno de 15 Å e é obtida. A parte interna da folha, que mede cerca de 6 Å, tem uma dimensão compatível com a espessura do grafeno. No entanto, se consideramos uma densidade eletrônica média para as duas partes da folha, uma espessura aproximativa de 10 Å é obtida.

A estrutura organizada em lamelas também foi caracterizada com os modelos utilizados. Os parâmetros sensíveis à flexibilidade das folhas foram obtidos e seu comportamento,

em função da hidratação do sistema, foram analisados. Estes resultados conduziram à extração do módulo de compressibilidade da estrutura empilhada. A Figura 4.8 mostra que, como previsto para sistemas como as fases lamelares de GO, quanto menor a distância entre as folhas, maior é a força necessária para deslocá-las da posição de equilíbrio.

Em seguida, o sistema binário composto de surfactante e solução aquosa ácida foi explorado. Os experimentos revelaram a formação de bicamadas anfífilas organizadas em estrutura lamelar para sistemas não muito concentrados. A estrutura também obedece a lei de diluição, o que quer dizer que ela expande quando o solvente é adicionado ao sistema. Não obstante, uma transição de fase é observada para as amostras muito concentradas e uma estrutura que não pode ser identificada é obtida.

Este estudo permitiu que o sistema binário desidratado composto por folhas de GO e tensoativo fosse explorado. A cinética desse sistema mostrou que um longo tempo de homogeneização é necessário para estabilizar a estrutura, um fator inconveniente para o estudo.

Para pequenas quantidades de tensoativo, as folhas de GO se organizam em uma estrutura empilhada e as moléculas anfífilas adsorvem à sua superfície. Com um aumento na quantidade de surfactante, as moléculas se organizam na superfície e a estrutura se expande, até o momento em que o limite de diluição é atingido. Neste momento, o tensoativo forma uma estrutura similar à uma bicamada, onde a parte hidrofílica fica em contato com a folha. Para concentrações ainda maiores de surfactante, as moléculas anfífilas em excesso formam uma fase à parte, que também é estruturada. A Figura 5.12 representa esquematicamente as fases descritas.

Essas fases podem também ser diluídas com água, sendo que as moléculas adicionadas vão se inserir na superfície das folhas. Para os sistemas com uma proporção elevada de surfactante e que representa um domínio restrito do diagrama ternário, uma nova fase é observada. Nesta nova fase, as moléculas anfífilas se separam da folha de GO e se organizam em bicamadas, que são separadas por camadas de água com as folhas de GO em dispersão. As representações esquemáticas dessas fases podem ser observadas na Figura 5.18. Os domínios do diagrama ternário onde cada uma das fases são observadas, são delimitados por zonas de transição, sendo que as duas fases descritas, ou até mesmo outras fases, podem coexistir.

Dois complexos ternários distintos foram obtidos, cujas zonas de existência são separadas por regiões de transição. O domínio de transição é diretamente ligado aos respectivos sistemas binários, no entanto, algumas estruturas ainda restam a ser caracterizadas em detalhes.

Todos os resultados obtidos para os sistemas estudados permitiram a construção do diagrama ternário apresentado na Figura 5.20, o que resume as estruturas observadas.





**Title:** Graphene oxide sheets confined within anisotropic fluid matrices

**Abstract:** Since the discovery of graphene oxide (GO), the most accessible of the precursors of graphene, this material has been widely studied for applications in science and technology. The motivation of this work is to study with a fundamental perspective the coupling between amphiphilic bilayers, which can be seen as an anisotropic matrix formed of two-dimensional objects, and another two-dimensional object, namely the graphene oxide sheet when they are dispersed in a common solvent. The competition between the intrinsic elasticities of the bilayers and GO sheets, as well as between direct bilayer-bilayer, bilayer-GO and GO-GO interactions allows us to envisage a rich polymorphism, depending on the composition of the system. Following the development of a dedicated procedure for controlling in an extended range of GO content the binary GO-water system, the confined domain of aqueous GO dispersions was first investigated, and the ternary phase diagram then constructed. The obtained systems have been characterised, using techniques such as optical microscopy, light and x-ray scattering. Elastic and thermodynamic properties have been described by applying, and adapting to the scope of this study, models for two-component lamellar stacks.

**Keywords:** graphene oxide, surfactant, liquid crystal, SAXS, stacked layers

---

**Titre :** Confinement de feuillets de graphène oxydé dans une matrice fluide anisotrope

**Résumé :** Dès sa découverte, le graphène oxydé (GO), le plus accessible des précurseurs du graphène, a été largement utilisé pour des applications en science et technologie. La motivation de ce travail est d'étudier, d'un point de vue fondamental, le couplage entre des bicouches amphiphiles auto-associées (lesquelles peuvent être vues comme une matrice anisotrope formée d'objets bidimensionnels) et un objet lui-même bidimensionnel, en l'occurrence le feuillet d'oxyde de graphène, quand ils sont dispersés dans un solvant commun. La compétition entre les élasticités intrinsèques des bicouches et des feuillets de GO, ainsi que les interactions directes bicouche-bicouche, bicouche-GO et GO-GO, permet d'envisager un riche polymorphisme en fonction de la composition du système. Après avoir développé une procédure destinée à contrôler, dans une gamme étendue de teneur en GO, le système binaire GO-eau, le domaine confiné des dispersions aqueuses de GO a été exploré et, par la suite, le diagramme de phases ternaire a été construit. Les systèmes obtenus ont été caractérisés par des techniques comme la microscopie optique et la diffusion du rayonnement (diffusion dynamique de la lumière et diffusion des rayons-X aux petits angles). Les propriétés élastiques et thermodynamiques ont été décrites par l'application de modèles initialement conçus pour les phases lamellaires à deux constituants et adaptés dans le cadre de cette étude.

**Mots clés :** graphène oxydé, tensioactif, cristaux liquides, SAXS, empilements de bicouches

---

**Título:** Confinamento de folhas de grafeno oxidado em uma matriz fluída anisotrópica

**Resumo:** Desde sua descoberta, o grafeno oxidado (GO), o mais acessível dos precursores do grafeno, tem sido amplamente utilizado para aplicações na ciência e tecnologia. A motivação deste trabalho é de estudar, de um ponto de vista fundamental, o acoplamento entre bicamadas anfífilas auto-organizadas (que podem ser vistas como uma matriz anisotrópica formada por objetos bidimensionais) e um objeto ele mesmo bidimensional, neste caso a folha de óxido de grafeno, quando estão dispersados em um solvente comum. A competição entre as elasticidades intrínsecas das bicamas e das folhas de GO, assim como as interações diretas bicamada-bicamada, bicamada-GO e GO-GO, permitem esperar um rico polimorfismo em função da composição do sistema. Seguindo o desenvolvimento de um procedimento destinado ao controle, em um intervalo estendido da quantidade de GO, o sistema binário GO-água, o domínio confinado de dispersões aquosas de GO foi explorado e, em seguida, o diagrama de fases ternário construído. Os sistemas obtidos foram caracterizados por técnicas como microscopia ótica, espalhamento dinâmico de luz e espalhamento de raios-x à baixos ângulos. As propriedades elásticas e termodinâmicas foram descritas pela aplicação de modelos inicialmente concebidos para fases lamelares à dois constituintes e adaptados ao escopo deste estudo.

**Palavras-chave:** grafeno oxidado, surfactante, cristais líquidos, SAXS, empilhamento de bicamadas

---